

Master Thesis

TVVR 18/5007

Coastal erosion in the region of Thu Bon River mouth, Vietnam



Eric Asplund

Hanna Malmström



Division of Water Resources Engineering
Department of Building and Environmental Technology
Lund University

Coastal erosion in the region of Thu Bon River mouth, Vietnam

By:
Eric Asplund
Hanna Malmström

Master Thesis

Division of Water Resources Engineering
Department of Building & Environmental Technology
Lund University
Box 118
221 00 Lund, Sweden

Water Resources Engineering
TVVR-18/5007
ISSN 1101-9824

Lund 2018
www.tvrl.lth.se

Master Thesis
Division of Water Resources Engineering
Department of Building & Environmental Technology
Lund University

English title: Coastal erosion in the region of Thu Bon River mouth,
Vietnam
Authors: Eric Asplund
Hanna Malmström
Supervisor: Magnus Larson
Nguyen Trung Viet
Examiner: Hans Hanson
Language: English
Year: 2018
Keywords: Coastal erosion; Cua Dai Beach; longshore sediment
transport; EBED; Cascade

Acknowledgements

This master thesis study is done in cooperation between Lund University in Sweden and Thuyloi University in Vietnam. We would like to thank our supervisor Professor Magnus Larson at the Division of Water Resources Engineering at Lund University for introducing us to this exciting project, and for the guidance through the thesis process.

In Vietnam, our supervisor Professor Nguyen Trung Viet at Thuyloi University in Hanoi, supported us with both practical arrangement and through our work. We really appreciate his inputs and that he made sure that we were well taken care of. We would also like to thank Dr. Pham Thanh Nam and Mr. Duong Cong Dien from the Department for Marine Mechanics and Environment at the Institute of Mechanics in Hanoi, Vietnam, for guiding us through the process regarding the EBED model and providing us with needed data. At the Central Region College of Technology in Hoi An, we got a warm welcome from Dr. Pham Quang Dong. We are grateful for the assistance when conducting field measurements, and would like to thank Mr. The Nguyen and Mr. Dien Hoang for the support.

This master thesis project is funded by the Swedish International Development Cooperation Agency, SIDA, and the ÅForsk Foundation. We are very thankful for the opportunity the provided us with and making this journey possible.

Abstract

Coastal erosion has increased worldwide during the last decades, mostly due to human activities. Vietnam is not spared, where many places within the country suffer from beach erosion. This report focuses on the region around Thu Bon river mouth in the central part of Vietnam. The beaches next to the river mouth are experiencing severe erosion, especially Cua Dai Beach. The beach is totally eroded in some areas, and the erosion seems to move further away from the river mouth, which will affect the tourist business.

There is a lack of previous studies regarding nearshore wave climate and sediment transport along the coast. In the present investigation, field studies and simulations have been carried out to address this lack of knowledge. Three different numerical models have been used to (1) calculate wave climate (EBED), (2) longshore sediment transport (LST Cascade), and (3) shoreline evolution (Cascade). The future shoreline evolution was simulated for 30 years, employing two different scenarios. The first scenario implied no change in sediment transport with the river flow, whereas in the second scenario the sediment transport was reduced to half of its initial value after 15 years. The results show a further retreat of the shoreline on the northern side of the river mouth, which already has an erosion problem. The erosion will move even more to the north in the future, if proper action is not taken.

Keywords:

Coastal erosion; Cua Dai Beach; longshore sediment transport; EBED; Cascade

Table of contents

1	Introduction.....	1
1.1	Background.....	1
1.2	Objectives	2
1.3	Procedure	3
1.4	Report disposition.....	4
2	Coastal processes	5
2.1	The coastal zone	5
2.2	Waves	6
2.2.1	Wave classification and categories	6
2.2.2	Wave velocity.....	6
2.2.3	Shoaling, refraction, and diffraction	7
2.2.4	Wave height.....	8
2.2.5	Depth of closure	8
2.3	Wind	8
2.4	Currents	9
2.5	The beach sediment	9
2.6	Sediment transport.....	10
2.7	Coastal erosion	11
2.7.1	Natural causes	12
2.7.2	Man-made causes	12
2.7.3	Coastal protection.....	13
3	Area description	15
3.1	Vu Gia Thu Bon River basin	15
3.1.1	River system.....	16
3.1.2	Climate	16
3.1.3	Land use and economic activities.....	17

3.2	Thu Bon River mouth and its vicinity	17
3.2.1	Hoi An Town.....	19
3.2.2	Coastal processes.....	19
3.2.3	Coastal morphology at Cua Dai Beach	21
3.2.4	Possible reasons for the erosion	22
4	Theory: Numerical modelling.....	23
4.1	EBED: Nearshore wave model.....	23
4.2	LST: Longshore Sediment Transportation	26
4.3	Cascade: Longshore sediment transport and long-term shoreline evolution	27
5	Data collection and analysis.....	31
5.1	Field survey	31
5.2	Beach profiles	36
5.3	Sediment analysis	37
5.4	Bathymetry	39
5.5	Offshore wave climate.....	39
5.6	Shorelines	42
6	Modelling processes.....	45
6.1	EBED.....	46
6.1.1	Model implementation	46
6.1.2	Sensitivity analysis and validation	47
6.1.3	Result and analysis	52
6.2	LST.....	56
6.2.1	Model implementation	56
6.2.2	Result and analysis	56
6.3	Cascade.....	59
6.3.1	Model implementation	59
6.3.2	Calibration and validation	60
6.3.3	Result and analysis	63

7	Discussion	67
7.1	Data collection	67
7.2	Numerical modelling	69
8	Conclusion	73
	References	74
	Appendix A: Data collection.....	81
	A1. Beach profiles	81
	A2. Sediment analysis	87
	A3. Offshore wave climate data	91
	A4. Shorelines	93
	Appendix B: Numerical modelling	95
	B1. EBED	95
	B2. LST	97
	B3. Cascade	97
	B4. Comparison between LST and Cascade	103

1 Introduction

1.1 Background

Almost all coastal countries have problems with coastal erosion (Rijn, 2011), which is a permanent loss of sand from a beach system. There has always been coastal erosion, which has shaped and contributed to the form of present coastlines. However, during the last decades, coastal erosion has been increasing in many places due to human activities. One of the main reasons for coastal erosion is the disturbance of the sediment transport system, which often is in balance in its natural state. Man-made structures that affect the sediment transport will have a negative influence and cause coastal erosion.

When engineers have tried to solve the erosion problem in a specific area, in many cases they created a new problem in a nearby area (Rijn, 2011). The behaviour and movement of coastal erosion depend on the type of coast and factors such as wave exposure, wave climate, surge levels, sediment composition, and beach slope (Rijn, 2011). To solve a coastal erosion problem, it is of importance to understand the coastal process taking place. The complexity of a problem varies extensively (US Army Corps of Engineers, 1984). There are substantial differences in the dynamics of coastal systems and the amount of wave energy affecting them. Before finding a suitable solution, where and how the problem is emerging needs to be thoroughly studied, and the reason for erosion should be identified. (US Army Corps of Engineers, 1984)

Vietnam is a country where coastal erosion is a common problem. Along a total coastline of 3,260 km, many regions suffer from erosion problems (Viet, et al., 2015a; Delegation of the European Union to Vietnam, 2018). To date, several studies have been conducted to increase the understanding of the erosion mechanisms and to find suitable protection along the coastline against erosion. The European Union (EU) together with the French Development Agency (AFD) support the ongoing work regarding coastal protection in Vietnam. They both express the need for assistance to Vietnam for adaptation to climate change, since it is a country particularly affected by the changing climate and its consequences. The European Union states that the existing man-made erosion problems will get worse due to the rising sea level. Sustainable development of coastal protection is therefore of highest priority for Vietnam. (Delegation of the European Union to Vietnam, 2018)

This master thesis project focuses on the coastal erosion problem at a field site situated in the central part of Vietnam, in the vicinity of the Thu Bon River mouth. Thu Bon River is one of the largest rivers in Vietnam (Viet, et al., 2015a). It is located outside Hoi An Ancient Town, which is classified as a UNESCO World Heritage site (UNESCO, 2018). The coastal area on the left side of the river mouth (north) is a sandy beach named Cua Dai Beach, which suffers from severe erosion problems (Viet, et al., 2015a). The shoreline has eroded about 200 m during a ten-year period (Hung, et al., 2017). The coastal erosion affects the entire morphology in the area (Viet, et al., 2015a). It also has negative consequences for the tourism, the safety of the people, and the overall development of the city Hoi An (Hoang, et al., 2015).

1.2 Objectives

The purpose of this study is to clarify the factors controlling the erosion of the area around Thu Bon River mouth. There are a few studies on the coastal erosion problem in this area (Viet, et al., 2015a). Previous studies have identified the need for field data collection to obtain better understanding of the erosion mechanisms, which may serve as a basis for developing and applying models to predict the coastal evolution and the effects of different measures to combat the erosion (Viet, et al., 2015a; Hoang, et al., 2015; Hung, et al., 2017; Viet, et al., 2015c). The report “Analysis of shoreline erosion at the Da Rang River Mouth” by Hoang et al. from 2015 stresses explicitly that the lack of measured field data limits the studies on morphological changes of the beaches in Vietnam. Many of the existing studies of Cua Dai Beach use estimated values based on different assumptions, not measured data from the site (Viet, et al., 2015a; Hoang, et al., 2015; Hung, et al., 2017). Therefore, additional field studies are of great importance. This study aims to give a better understanding of the erosion mechanism around Thu Bon River mouth. The study will be performed on a regional scale around the river mouth, trying to clarify the processes taking place within the coastal system. The result will be useful for future studies on a more local level regarding the protection and development of the area.

The erosion mechanisms will be examined through the following work components:

- Measurements of beach profiles at selected lines alongshore
- Surveying of the shoreline, the vegetation line, and existing structures
- Sediment sampling and analysis
- Nearshore wave modelling
- Longshore sediment transport modelling
- Long-term shoreline evolution modelling

1.3 Procedure

The project was carried between January and June 2018. The study was conducted partly in Lund, Sweden, and partly in Hoi An and Hanoi, Vietnam. During the first three weeks, a literature study was performed in Lund. The area of interest was investigated, and previous reports were examined. Practical preparations concerning the trip and work in Vietnam was also made.

From the 30th of January to the 11th of April, the work took place in Vietnam. Three weeks were spent in Hanoi for data collection and receiving input from our Vietnamese supervisor, Professor Nguyen Trung Viet at Thuyloi University. Preparation for the nearshore wave modeling with EBED was also carried out during the time in Hanoi, with guidance from Dr. Pham Thanh Nam, who has contributed to the development of the model. The remaining time was spent in Hoi An, in the vicinity of the area of interest. There, a field survey of Cua Dai Beach, severely affected by the erosion, took place. Sediment sampling and analysis, and measurements of beach profiles were also done with help from the Central Region College of Technology Economics and Water Resources in Hoi An. All of the field measurements and analysis took place in March 2018.

The time between April and June were spent in Lund. The EBED model was ran during the first week back in Sweden. Based on the EBED results, modelling of the longshore sediment transport with a model called LST in this report, as well as with Cascade was performed. Cascade also simulated the long-term shoreline evolution. The writing of the report took place during the entire project period.

1.4 Report disposition

Chapter 2 in the report describes in short the theory of coastal process relevant for the present study. The impact of waves, wind, and currents are described followed by sediment transport processes and the concept of coastal erosion. Chapter 3 contains a description of the area of interest. It starts on a catchment scale and narrows down to the area around Thu Bon River mouth. In Chapter 4, the theory behind the three used models, EBED, LST, and Cascade, are discussed.

The data collected for the study is presented in Chapter 5. It is followed by Chapter 6, where the models are presented. Each of the models have their own section containing relevant process steps together with results and analysis. The next chapter (Chapter 7) discusses the reliability and quality of the input data and the model results. The conclusions are given in the final Chapter 8.

The report also includes Appendix A and B. Appendix A includes information from the data collection and Appendix B from the numerical modelling.

2 Coastal processes

The interaction between water, wind, and land shapes the many physical processes taking place in the coastal area. It is a complex physical system where the water supply energy and the land absorbs it. This chapter explains some of the many processes taking place of relevance for the present study. The chapter starts by introducing a definition of the coastal area, followed by an explanation of some essential coastal processes regarding wave generation, currents, wind influence, and sediment transport. The last part discusses causes of coastal erosion and common protection methods.

2.1 The coastal zone

Multiple zones define a typical cross-sectional profile of the coastal area. The coast is separated from the beach or shore by a somewhat fixed border, the coastline (US Army Corps of Engineers, 1984). It could be for example cliffs, hard structures, or well-established vegetation. The beach or shore is divided into two zones, the backshore, and the foreshore. The backshore is located closes to the coastline and contains berms. A berm is defined by an elevation change of a sandbank. The foreshore starts at the high-tide shoreline and ends at the low-tide shoreline. The beach or shore is then followed by the nearshore zone which is the area where nearshore currents occur. The nearshore consists of the inshore (also called shoreface) where waves break, followed by the offshore further out. The point where the waves fall is called the plunge point, which is located within the inshore. The surf zone is the area where the waves break and are swashed on to the beach or shore; the different zones are illustrated in Figure 1 below. (US Army Corps of Engineers, 1984)

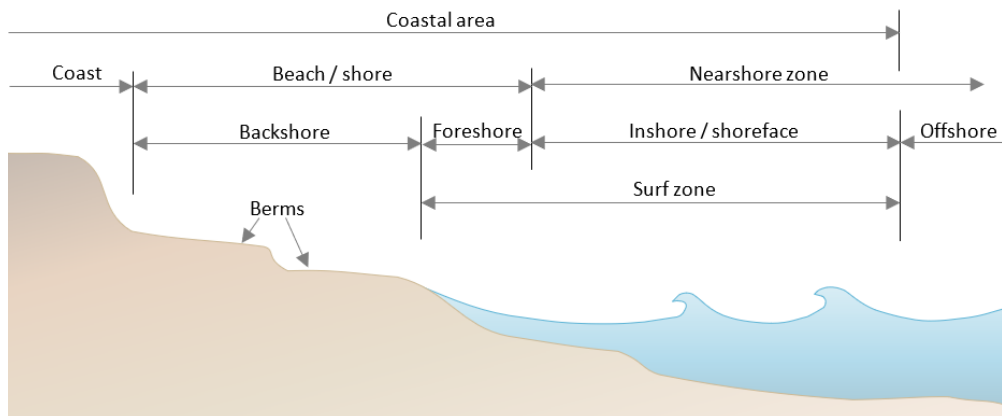


Figure 1. An illustration of the beach profile showing the different coastal zones.

2.2 Waves

Waves are an important factor in how the beaches are forming (US Army Corps of Engineers, 1984). The waves contribute with energy to the beach which leads to the transportation of bottom sediment onshore, offshore, and alongshore, as well as to sorting of bottom sediments on the foreshore. The phenomena of water waves are complex and challenging to explain mathematically due to three-dimensional characteristics, nonlinearities, and random behaviour. The most used theory which describes simple sinusoidal waves was developed by Airy (1845). The theory is proven to work better in deep water, where the bottom does not influence the wave, and the depth relative to the wavelength is not too small. This is a linear wave theory, and it is easy to apply and gives in general satisfactory results over most parts of the whole wave regime. (US Army Corps of Engineers, 1984)

2.2.1 Wave classification and categories

Waves can be classified with regard to the water depth. There are three different types of water waves that are categorised by depth (d) divided by wavelength (L). They are deep water waves, shallow water waves, and transitional water waves; the ranges of these waves are defined in Table 1. (US Army Corps of Engineers, 1984)

Table 1: Classification of waves with regard to relative depth.

Wave category	d/L
Deep-water waves	> 0.5
Transitional water waves	< 0.5 and > 0.04
Shallow water waves	< 0.04

2.2.2 Wave celerity

A simple wave (Airy linear wave theory) is described mathematically with a single cosine or sine function (water surface profile). Where the equation for wave celerity, also called phase speed, can be expressed as in Equation 1:

$$C = \frac{L}{T} = \frac{gT}{2\pi} \tanh\left(\frac{2\pi d}{L}\right) \quad (1)$$

Where,
 L = wavelength (m)
 T = period (s)
 g = gravitational constant (m/s^2)
 d = depth (m)

For deep water and shallow water, the expression can be simplified to Equation 2 (deep) and Equation 3 (shallow).

$$C = \frac{L}{T} = \frac{gT}{2\pi} \quad (2)$$

$$C = \frac{L}{T} = \sqrt{gd} \quad (3)$$

The group velocity, C_g , is the moving speed of the wave train, which differs from wave celerity in deep water, see Equation 4. This speed also represents that transfer of energy in the wave train that is employed in the energy conservation for water waves. In shallow water where the celerity is only dependent on the water depth, the waves will travel at the same speed, see Equation 3. Therefore, the wave train will have the same velocity as the waves, see Equation 5. (US Army Corps of Engineers, 1984)

$$C_g = \frac{C}{2} = \frac{gT}{4\pi} \quad (4)$$

$$C_g = C = \sqrt{gd} \quad (5)$$

2.2.3 Shoaling, refraction, and diffraction

When a deep-water wave approaches shallow water, the depth will influence the wave celerity as can be seen in Equation 2. As the wave celerity decreases, the wavelength must decrease proportionally. If the energy between wave rays is assumed to remain constant and the crest is parallel to the shore the wave height increases as the wave approaches the shore; this is called shoaling. However, if the bottom contours and the wave crest are at an angle, there will be a velocity variation along the wave crest. The wave moves faster in deeper water and will try to align to the bottom contours. Depending on the bending of the wave, the wave height can both increase and decrease. This bending effect of the wave is called refraction, and together with shoaling they determine the wave height. (US Army Corps of Engineers, 1984)

Diffraction is a phenomenon which usually occurs when waves are interrupted by an island or breakwater. The energy is distributed sideways along the wave crest behind the obstacle. The more the wave bends around the obstacle, the less will the wave height be. (US Army Corps of Engineers, 1984)

2.2.4 Wave height

Classification of wave heights in a statistical sense is derived from the Rayleigh wave height distribution curve. A relevant term is the significant wave height, denoted by H_s , which is the average of the highest 1/3 of the waves. (US Army Corps of Engineers, 1984) Another measure is the root-mean-square wave height (H_{rms}), which is given by $H_{rms} = H_s/1.416$ according to the Rayleigh distribution.

2.2.5 Depth of closure

The depth of closure is the depth limit where the beach profile is not seasonally changing due to sediment transport. The depth of closure can be calculated with an equation developed by Hallermeier (1980) (Equation 6).

$$h_d = 2.28H_e - 68.5 \left(\frac{H_e^2}{gT^2} \right) \quad (6)$$

Where, H_e = The significant wave height that is exceeded twelve hours per year (m)
 T = The corresponding wave period to the H_e (s)
 g = gravitational constant (m/s²)

2.3 Wind

Wind plays an important role in the generation of waves and the characteristics of the waves (US Army Corps of Engineers, 1984). Wind wave properties are characterised by the wind speed, the wind duration, the water depth, the fetch, and the decay distance. The fetch is the length the wind blows over the sea when generating waves, and the decay distance is the length the wave travels after the wind forcing ceases.

To predict wave generation by wind, an estimation of the wind speed over the water surface and the fetch are needed. The wind speed can be obtained from observations over the fetch, projections made from land data, or weather forecasts. After the wind speed is obtained, an adjusted wind speed must typically be determined before use in the governing equations for wave growth. The factors elevation, duration-average wind speed, stability correction, location effects, and coefficient of drag needs to be considered. A deep-water wave is either duration-limited or fetch-limited. In the beginning, the wave growth will be duration-limited, but after a certain amount of time, it

will be fetch-limited instead. With the help of the wind data, a hindcast approach can be employed to predict historical wave heights. (US Army Corps of Engineers, 1984)

2.4 Currents

The influences of currents in the nearshore zone vary and are for some systems certain currents are more significant than others. Factors that cause the formation of currents in the nearshore zone are water level differences created by, for example, wind and breaking of waves. Another situation when currents occur is at a river outlet where the water being discharged generates currents in the nearshore zone. Current formation could also happen due to tidal motion, so-called tidal currents. These currents can be significant at, for example, lagoon inlets or harbours. (US Army Corps of Engineers, 1984)

One important type of current that often occurs at shallow water are longshore currents. These types of currents are created due to breaking waves approaching the shoreline at an angle, and they are in general the most important currents for coastal sediment transport. Local currents directed away from the shore back seaward, it is called rip currents. (US Army Corps of Engineers, 1984)

2.5 The beach sediment

The origin of beach material could vary a lot. It can come far away from the coast with streams and rivers (US Army Corps of Engineers, 1984). Other origins could be from erosion of formations in the coastal zone, or travel from deeper regions in the sea on to the shore. The main parameters to define the characteristics of the sediment is the grain size distribution and the median grain size (D_{50}). To determine these material characteristics a widely used method is to collect sediment samples at the location of interest and then filter the sample through sieves with varying mesh sizes (Gyr & Hoyer, 2006). The definition of the different grain sizes is presented in Table 2.

Table 2. Grain size definitions.

Type	Grain size
Boulder	0.25 – 4 m
Cobble	50 – 250 mm
Gravel	2 – 50 mm
Sand	0.06 – 2 mm
Silt	$4 - 60 \times 10^{-3}$ mm
Clay	$0.25 - 4 \times 10^{-3}$ mm

The sediment properties will have an impact on the beach slope. Finer grains typically provide less inclination than larger grains. In the cross-shore direction, the sediment size will in general vary. The beach and grain characteristics will together with the accessible coastal material decide how the beach manages the forces from the sea. (US Army Corps of Engineers, 1984)

2.6 Sediment transport

Littoral transport is the name for the processes causing movement of sediment in the nearshore area due to waves and currents (US Army Corps of Engineers, 1984). Wave breaking is typically the main generating factor for sediment movement. When the waves break in the nearshore zone, they create turbulence in the water that will mobilize and suspend the bottom sediment. A lack of carrying capacity results in deposition of sediment, starting with the coarser grains. The energy generated due to turbulence, transports finer grains to less turbulent areas to settle there (Jianga, et al., 2015). Smaller grains need less energy to be set in motion and are more easily transported with waves and currents. (Hanson, 2017a)

Sediment can be transported in three different modes; bed load, sheet flow, and suspended flow. Bed load motion occurs along the bottom, and the grains are in contact with each other when moving. The movement starts when the bed shear stress reach the threshold of motion. Sheet flow also occurs along the bottom but at high shear stresses resulting in a layer of sediment in motion. Suspended load is when grains are lifted by the water motion upwards from the bed and are maintained in the water column by the turbulence (Soulsby, 1997).

There are two main types of littoral transport at the coast, longshore and cross-shore. How prominent each type is depending on the grain size, the beach slope, and the wave energy. Cross-shore transport occurs perpendicular to the coastline, in the seaward or shoreward direction (US Army Corps of Engineers, 1984). The cross-shore transport creates short-term variations in the beach profile shape on the event (storm) or seasonal scale (Hanson, 2017a), but often have limited long-term effects on the beach. If a wave traveling up on the beach can reach higher elevations, for example, during a storm, it may erode the upper part of the beach and transport sediment in the offshore direction, creating bars in the sea. The bars will influence the waves to break earlier, hence, lower the wave energy reaching the foreshore. When the wave conditions get calmer, the sediment creating the bars will be transported back to the beach (US Army Corps of Engineers, 1984).

Longshore transport occurs when the waves break and hit the beach at a non-perpendicular angle, creating longshore currents. The angle of approach together with the duration and the energy of the incoming waves determine the longshore transport rate. Depending on season and local climate the rate could vary a lot. The net transport rate means the net amount of sediment transport passed a specific point in a predefined direction. The gross transport rate adds all the sediment transport, regardless of direction. (US Army Corps of Engineers, 1984)

2.7 Coastal erosion

The main causes for coastal erosion are disturbances in the natural sediment transport system (Rijn, 2011). Changes in the sediment budget can result in the transformation of areas functioning as sediment sources to sinks, and vice versa (Bird & Lewis, 2015). The reasons for such alterations are many and could be due to both natural or man-made causes and be long-term or short-term. To comprehend the reasons for coastal erosion, it is essential to examine and understand the different coastal processes taking place in the studied system. Field surveys can promote such understanding as well as numerical modelling. A clear perception of the system will help to find sustainable solutions for the erosion problem (US Army Corps of Engineers, 1984). Lack of knowledge of the studied system can have a negative effect and create significant erosion problems in adjacent areas (Rijn, 2011).

2.7.1 Natural causes

A natural reason for beach erosion is a lack in sediment supply. It can be from stabilization of eroding nearby cliffs that provides sand and gravel material to the beach (Bird & Lewis, 2015). A decreased sediment availability could also be due to reduced flows in rivers and streams experiencing sediment transport. The river discharge will have a natural seasonal variation and can significantly decrease during drier periods when less runoff occurs. (Bird & Lewis, 2015; US Army Corps of Engineers, 1984)

As previously discussed, beach sediment can be transported offshore with the waves. If the water level increases due to, for example, surge during a storm, it will allow larger waves to reach the upper part of the profile, promoting erosion (Bird & Lewis, 2015). Another cause of offshore transport is sea level rise, which contributes to a gradual retreat of the shoreline (US Army Corps of Engineers, 1984).

Variations in the longshore sediment transport will determine where erosion occurs. If there is an increase in the sediment transport along the coast, it will induce erosion, whereas a decrease means accretion (Bird & Lewis, 2015). How much sediment that will be drifting along the shore depends on the factors that generate the longshore transport rate (US Army Corps of Engineers, 1984).

2.7.2 Man-made causes

Substantial causes where humans influence the shore erosion are due to different types of structures. Coastal structures preventing erosion locally may have side effects influencing nearby shores and their vulnerability towards erosion. Hard structures can reflect the incoming wave energy and the surrounding beaches need to cope with a higher energy dissipation increasing the erosion rate (US Army Corps of Engineers, 1984). Reflected waves will create currents transporting the sediment offshore, lowering the bottom close to the hard structure, which is called local scour (Bird & Lewis, 2015).

Man-made structures could also obstruct the sediment transport to beaches, which are common reasons for reduced sediment availability (US Army Corps of Engineers, 1984; Bird & Lewis, 2015). Protecting concrete structures can prevent erosion from the landmass behind, but stops the sediment supply to downdrift areas. Other structures such as dams in a river system, created for example in conjunction with hydropower generation, control the flow that is discharged. The dams will also function as sediment sinks due to reduced

velocities and turbulence, which allows particles to settle. Therefore, the fluvial sediment that is discharged from the dam will be less than in the inflowing water. (Bird & Lewis, 2015)

A reduction in fluvial sediment can have severe consequences for beaches adjacent river mouths (Bird & Lewis, 2015). A further reason for a decrease is dredging of channels for navigational purposes. Problems due to dredging may occur if the material is removed from the active sediment transport zone. Dredging the nearshore zone can affect the amount of wave energy impacting the beach, and therefore disturb the natural protection (US Army Corps of Engineers, 1984).

The extraction of underground resources, for example, groundwater close to the coastal zone, may cause subsidence of the land mass. Changes in elevation in the land mass mean that the shore needs to adapt to new water levels (US Army Corps of Engineers, 1984). A lowering of the groundwater level will also increase the seawater infiltration rate, which enhances long-term erosion processes (Bird & Lewis, 2015).

The use of sand as a resource, from the coastal area or the connected river system, could also cause erosion problems (Bird & Lewis, 2015). Sand mining disturbs the natural sand balance, reducing the sediment supply. If sand is taken from the beach, it lowers the shore elevation forcing the system to adapt to higher water levels. (Bird & Lewis, 2015)

2.7.3 Coastal protection

The type of needed coastal defence against erosion will depend on the causes of the erosion problem, the desired result, and adaptations to the surrounding environment. There are three categories of coastal protection: soft, intermediate, and hard structures. (Hanson, 2017b)

An example of soft protection is the beach, which constitutes the most seaward defence. Behind the beach, the existence of dunes creates another soft natural protection against waves (US Army Corps of Engineers, 1984). They are originally formed by sediment blown with the wind over the berm on to the land behind the beach. The dunes work as storage of sand. If vegetation stabilizes the dunes the natural protection will increase. The dunes function as protection has in many cases been ruined due to near-coastal urban development. Beaches and dunes can be nourished or reconstructed to increase its defence capacity (Bird & Lewis, 2015). A strategy to reinforce the dunes is

the use of sand fences. The fences will work as a sand trap for the aeolian sediment transport and are usually constructed with wooden planks but can also consist of fine nets (Grafals-Soto & Nordstrom, 2009).

A revetment of sandbags is a type of intermediate structure. The solution with sandbags is a short-term solution. The sandbags are easily destroyed, sensitive to UV radiation, and causes toe erosion. However, they are easy to install, repair, and replace. It could be a good temporary solution in low-energy systems, but will not be sustainable in a longer perspective (Hanson, 2017b). Geotube is the name for an intermediate solution that is getting more common. It is a geotextile filled with dredge material, for example, sand, that can extend for long distances (Imran, et al., 2017).

Common hard structures are seawalls and revetments made of concrete or rubbles. The structures aim to give solid protection of the shoreline from waves, stopping erosion at a specific location. Another function of hard structures is to trap sediment drifting along the shore. Example of such structures is groins and jetties. Detached breakwaters are hard protections constructed offshore, often parallel to the shoreline, reducing the wave energy that affects the coast behind them. (US Army Corps of Engineers, 1984)

3 Area description

Vietnam has an area of 331,100 km² with a population of 93.7 million situated in southeast Asia. It borders to China, Laos, Cambodia, and the South China Sea in the east (Nationalencyklopedin, u.d.). From the northern part of the country to the southern part, the climate is varying between tropical and subtropical. The subtropical climate occurs in the mountainous regions (Landguiden, 2016). The location of the study area is in the central part of Vietnam east of the town Hoi An. The focus site is on the regional scale around the Thu Bon River mouth, where the river discharges its water into the South China Sea. The Thu Bon River drains part of the Vu Gia Thu Bon River basin and the river mouth is located adjacent to Cua Dai Beach, which is the area most affected by the erosion problems. This chapter contains a general description and provides the physical setting of the catchment, including the Thu Bon River mouth and its surroundings.

3.1 Vu Gia Thu Bon River basin

Vu Gia Thu Bon River basin is one of the largest river basins in Vietnam, located in the central part of the country (Nauditt & Ribbe, 2017). It extends in the east-west direction from the border of Laos to the South China Sea. Figure 2 shows a map over the river basin and its location in Vietnam together with the area of interest, the Thu Bon River mouth and its surroundings, marked in red.



Figure 2. A map showing the Vu Gia Thu Bon River basin containing topography, towns, river system, and the location of the field site (LUCCi, 2010).

3.1.1 River system

The name of the river basin comes from the two main rivers within the catchment, Vu Gia River and Thu Bon River (Nauditt & Ribbe, 2017). The river system contains 19 first-order streams that are connected to the two major rivers. Both major rivers in the basin flow from the Truong Son mountain range. The Vu Gia River is 145 km long and its water is discharged close to the city of Da Nang. The Thu Bon River is 205 km and with the mouth located east of the city Hoi An (Nauditt & Ribbe, 2017). Two streams connect the Vu Gia River with the Thu Bon River; about 30 km upstream from the Thu Bon River mouth the water flows from the Vu Gia River to the Thu Bon River, and 10 km downstream it flows the opposite way. (Viet, et al., 2015b)

3.1.2 Climate

The climate zone in the central part of Vietnam where the catchment is located belongs to the tropical monsoon climate. A rainy season occurs between September and January when flooding is a common problem for some areas (Viet, 2016; Nauditt & Ribbe, 2017). During this period, 65% to 80% of the total annual precipitation occurs (Nauditt & Ribbe, 2017). The wet season is followed by a dry season from February to August, which frequently causes droughts. The relative humidity is at its highest during the rainy season and

reaches up to 90%, and at its lowest at 75% in the dry season. In Hoi An, the average mean annual temperature is measured to be 25.6 °C. (Viet, 2016)

3.1.3 Land use and economic activities

The river basin is mainly occupied by forest (Nauditt & Ribbe, 2017). Agricultural and urban areas make up about 5% of the catchment each, with the crops located primarily around rivers and the largest cities along the coast. For tourists, two popular cities to visit are Da Nang and Hoi An, both located on the coast of the South China Sea. Also affecting the coast is the fast-growing industrial sector, which is the most significant economic source together with tourism. Example of products that are being produced in the region is rubber, clothes, and automobile products. (Nauditt & Ribbe, 2017)

Another activity that is taking place in the Thu Bon River system is sand mining (Hung, et al., 2017). During a field investigation in the lower part of the river system made by Fila et al. (2016), 35 active sand mining sites were observed during 24 hours.

In the middle and northern part of the catchment, hydropower production and forestry are the main contributing sectors to the economic development. (Nauditt & Ribbe, 2017; Hoang, et al., 2015). The Vu Gia Thu Bon River system plays a virtual role for the hydropower generation in Vietnam and is ranked number four in potential hydropower generation capacity. Since 2008, the hydropower sector has rapidly grown, and in 2014 it contributed to around 40% of the total energy production in Vietnam (Nauditt & Ribbe, 2017; Asian Development Bank, 2016). The river system has nine large hydropower plants and 36 medium- and small-size plants. Due to the extreme seasonal variations, the efficiency of the power plants changes significantly. The storage capacity of the hydropower plants is limited, which causes problems for storing water to reduce flooding or to cope with droughts. (Nauditt & Ribbe, 2017)

3.2 Thu Bon River mouth and its vicinity

The area of interest is the coastline around Thu Bon River mouth, with the focus on Cua Dai Beach adjacent to the river mouth. Cua Dai Beach is the area with most severe erosion problems. The region around the river mouth consists of two bays, one on the north side of the river and one on the south side. The bay on the north side of the river mouth starts outside the city of Da Nang close to the mountain Son Tra to the east of the town Hoi An and is around 30 km. The bay on the south side is about 50 km and stretches from south of the river

mouth to the island Tam Hai southeast of the town Tam Ky. Northeast of Thu Bon River mouth there is an island group called the Cham Islands. The Cham Islands are today a nature reserve situated around 18 km from the Thu Bon River mouth (Viet, 2016). A map of the field site is shown in Figure 3 with the whole coastline of interest marked in red. Figure 4 shows the location of Cua Dai Beach.

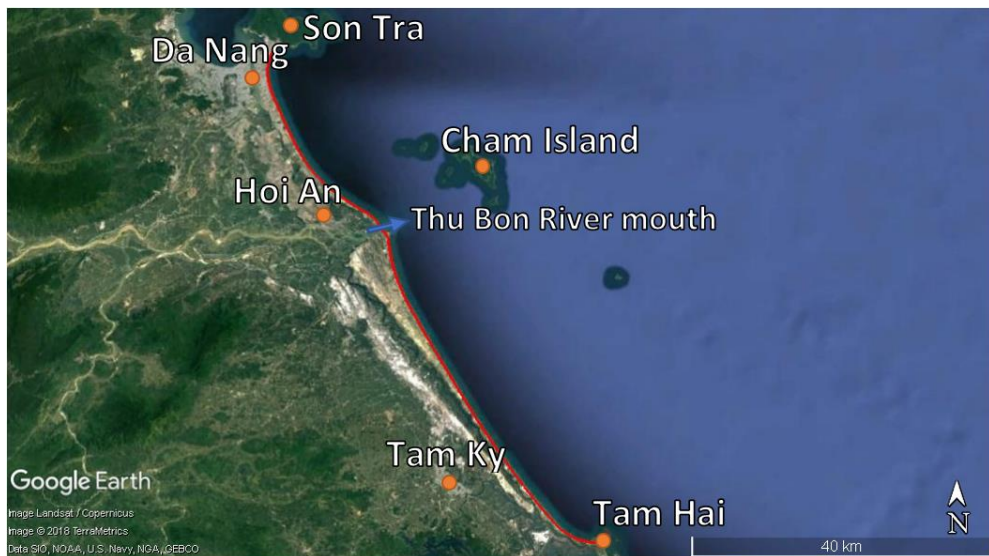


Figure 3. Overview of the field area with the coastline of interest marked in red (Google Inc, 2018).



Figure 4. A zoomed-in view of the field area around the Thu Bon River mouth. The yellow line shows Cua Dai Beach, which is most affected by erosion (Google Inc, 2018).

3.2.1 Hoi An Town

Hoi An is located near the mouth of the Thu Bon River, 30 km South of Da Nang. There was a small-scale trading port located here between the 15th and 19th century and the port traded with countries all over the world. The ancient town of Hoi An is well preserved, where the wooden structures and city plan originates from the 17th and 18th century, which is unique for the region. Also, influences of cultures from China, Japan, and Europe can be found. Therefore, the ancient city of Hoi An has a place on the UNESCO's World Heritage list. (UNESCO, 2018)

Many tourists visit the region and during the year of 2015, 3.9 million people visit Quang Nam district (Nauditt & Ribbe, 2017), where most of the people visited the famous town Hoi An. Cua Dai Beach is one of the nearest beaches from Hoi An, which makes this beach important for recreation and tourism. Cua Dai Beach suffers badly from erosion, where some parts of the beach are totally eroded and hotels have been forced to close (Hung, et al., 2017).

3.2.2 Coastal processes

3.2.2.1 Thu Bon River mouth

Along the stretch where the Thu Bon River flows past Hoi An, more tributaries are joined together in a complex river mouth system. The river mouth may be classified as being a mix between a lagoon river mouth and an L-shaped river

mouth, according to classifications in Vietnam (Viet, 2016). A more general classification is an estuary, where fresh water and salt water are mixed resulting in brackish water. The salinity of the water and the distance upstream the saline water can move depend on the relative importance of the river and tidal flow (NOAA, 2017a).

The mean yearly discharge of Thu Bon River is 327 m³/s; however, there is a large difference in discharge depending on the season (Viet, et al., 2015a). In a previous study made by Fila et al. (2016), the sediment transport in Thu Bon river was investigated based on three different methods. In the first method, the transport was estimated based on comparisons with similar catchments with known sediment concentrations. The second method calculated the sediment transport from the general characteristics of the river (e.g., bed slope). The last method used measured sediment concentration values that were multiplied with the average yearly discharge. Fila et al. (2016) also studied possible reasons for sediment transport reduction and estimated an approximate reduction of 28 % due to observed sand mining and dam construction. The estimated values for each of the methods are shown in Table 3, with a range of 390,000 to 600,000 m³/year and 280,000 to 430,000 m³/year after the reduction of 28 %.

Table 3: Estimated sediment transport in Thu Bon river for the three methods employed (based on catchment area, bed slope and sediment concentration measurements). The sediment transports are shown with and without a 28% reduction.

Method	Without reduction (m³/year)	With reduction (m³/year)
Catchment	600,000	430,000
Bed slope	440,000	320,000
Sediment measurements	390,000	280,000

3.2.2.2 Tide

The coast of Quang Nam has a mixed semidiurnal tide cycle, which means two low and two high tides of different sizes every lunar day (NOAA, 2017b). The maximum measured tidal range in Hoi An is 1.31 m (Tide-forecast, 2018). Two previous studies have performed calculations on the mean tidal range at Da Nang. The study by Lam (2009) gave an average tidal range of 0.72 m, and Tung (2011) got a value of 0.70 m.

3.2.2.3 *Wind*

In Hoi An, the monsoon is the essential factor determining the wind direction, duration, and speed. The most dominant winds are from the northeast, which arise from mid-October and last until the end of March. The weather is typically unstable, and storms may occur which create rough seas with large swells. From May until August the wind changes to a southeast direction; however, the wind is moderate and more irregular. Most coastal erosion occurs during the northeast winds. (Viet, 2016)

3.2.2.4 *Waves*

As mentioned in the previous section, the largest waves occur during mid-October until the end of March, approaching from northeast (Viet, 2016). The calmer summer months generates waves with heights of 1 to 2 m having a southeast approach (Fila, et al., 2016). The Cham Islands is located in the northeast direction from the Thu Bon River mouth, which significantly influences the wave heights at the river mouth.

3.2.3 **Coastal morphology at Cua Dai Beach**

Coastal erosion around Thu Bon River mouth is severe, and approximately 200-m width of the beach has eroded during the last ten years. The erosion has spread, and beaches within 5 km of the river mouth have erosion problems. The Cua Dai Beach, north of the river mouth suffers the most from erosion, where man-made structures have been constructed to protect hotels and stop further erosion (Hung, et al., 2017). Mostly hard structures and intermediate structures are used, such as concrete and rubble revetments, concrete walls, rubble mound, small sandbags, and geotubes. Some soft structures are implemented such as sand fences to enhance dune build-up (Fila, et al., 2016).

The coastal evolution based on satellite images from Google Earth from the year 2004 to 2017 is shown in Figure 5 below (Google Inc, 2018). The shoreline change may be compared between consecutive years (2004, 2011, 2014 and 2017). A significant retreat can be seen on both sides of the Thu Bon River mouth. When comparing the years 2004 and 2017, a beach width loss of 200 m is confirmed. In the most southern part of Cua Dai Beach, a spit reaching out into the river mouth can be observed for the years 2004, 2011, and 2014. In the year 2017, the end of the spit has been separated from the rest, creating a small island and resulting in two discharge paths to the ocean.



Figure 5. Satellite images showing the coastal evolution of the area close to Thu Bon River mouth (Google Inc, 2018).

3.2.4 Possible reasons for the erosion

Construction of dams upstream Thu Bon River for hydropower and irrigation purposes interrupts the sediment flow in the river and the sediment supply to the downstream coast will decrease. The highest amount of sediment transport is during flood season, where rivers usually have high flows and sediment concentrations (Kondolf, et al., 2014). Dams will decrease the flow in the river and the sediment carrying capacity, which will reduce the sediment transport and in addition trap sediment in the dam. (Hung, et al., 2017).

Another discussed cause of erosion is sand mining in the river channels and how it contributes to reduce sediment transport in the river. Also, dredging in the river mouth is frequently conducted to increase the navigability for fishing boats that further reduces the sediment supply to the coast. Because of the dredging, the natural conditions may be disturbed and the prevailing forces will try to restore the equilibrium bathymetry leading to increased sedimentation in the parts that are deepened through dredging (Hung, et al., 2017). Thus, the reduction of sediment supply in the river and river mouth could be the main reason for the erosion at Cua Dai Beach (Viet, et al., 2015a) (Duy, et al., 2016) (Tanaka, et al., u.d.).

4 Theory: Numerical modelling

This chapter explains in short, the theory behind the three numerical models used in the study to increase the understanding of the factors controlling the coastal evolution at Cua Dai Beach. The first model is the EBED model, which simulates nearshore wave transformation. The result from the EBED model simulations is a part of the input data for the next two models. The LST model calculates the longshore sediment transport rate based on the incident wave climate. The model Cascade also calculates the longshore sediment transport rate, but at a finer scale; also, this model calculates the shoreline evolution and allows for predictions of future shoreline positions. With the wave climate data, together with information from field surveys of, for example, shoreline positions, beach profile shape, and sediment grain size, Cascade simulates long-term shoreline evolution at the regional scale.

4.1 EBED:

Nearshore wave model

The EBED model is a multidirectional random wave transformation model (Mase, 2001) and it is based on the wave energy balance equation. The energy balance includes an energy dissipation term that describes for energy losses due to wave breaking. It also includes diffraction of waves using a parabolic approximation. The original EBED model created by Mase (2001) has been modified by Nam et al. (2017) to improve the description of dissipation due to wave breaking in the surf zone (Nam, et al., 2009). A new energy dissipation term was derived since the original formulation tended to over-predict wave heights in the surf zone. This term includes two dimensionless coefficients that depend on the offshore wave height, wavelength, and bottom slope. At steady state, the modified energy balance equation by Nam et al. (2017) is written as follows:

$$\begin{aligned} & \frac{\partial(v_x S)}{\partial x} + \frac{\partial(v_y S)}{\partial y} + \frac{\partial(v_\theta S)}{\partial \theta} \\ & = \frac{\kappa}{2\omega} \left\{ (C C_g \cos^2 \theta S_y)_y - \frac{1}{2} C C_g \cos^2 \theta S_{yy} \right\} - \frac{K}{h} C_g S \left\{ 1 - \left(\frac{\Gamma h}{H_s} \right)^2 \right\} \end{aligned} \quad (7)$$

Where, S = angular frequency spectrum density,
 $v_{x/y/\theta}$ = velocities in coordinate direction x , y and θ ,
 κ = calibration parameter to control effect of diffraction,

w = frequency,
 C = phase velocity,
 C_g = group velocity,
 h = still water depth,
 K = dimensionless decay coefficient,
 Γ = dimensionless stable wave height coefficient

The left-hand side term in Equation 7 describes the change in wave energy depending on the wave velocity in the horizontal directions x and y , and in the wave direction to the shore at the angle θ counting anticlockwise from the x -axis. The angular frequency spectrum density correlates with the wave energy (Mase, 2001). The first term on the right side includes an expression for the parabolic wave energy multiplied by how large the impact of diffraction is. It is followed by the part representing the energy dissipation due to wave breaking. The two coefficients K and Γ are described in Equation 8 and 9, respectively (Nam, et al., 2017);

$$\Gamma = 0.45 + \beta \quad (8)$$

$$K = \frac{0.9}{8} \left(1 + \frac{\beta}{\sqrt{H_o/L_o}} \right) \quad (9)$$

Where, β = bottom slope,
 H_o = offshore wave height,
 L_o = offshore wavelength

The coefficients Γ and K are important when estimating the energy loss and may be useful in the calibration process for a specific location. The bottom slope, wave height, and wavelength influence the wave breaking and are therefore important when describing Γ and K . Recommended value for Γ and K based on field measurements and laboratory studies are (Nam, et al., 2017);

$$0.37 \leq \Gamma \leq 0.59, \quad 0.06 \leq K \leq 0.32$$

A large Γ value means a higher stable wave height, which results in an overall lower energy loss. When K is high, the decay of the wave will be faster, that is, the wave height will decrease faster, and therefore at a higher energy dissipation rate.

For the model, needed input data are the offshore wave climate and the bathymetry. The numerical calculations are performed for a grid over the study area with a certain number of cells with a specific size. Each cell is assigned a

value for the water depth. The calculations start at the offshore boundary and proceed step by step as the wave approaches the shore. The output data provide information about significant wave height, significant wave period, and wave direction describing the wave climate for each cell. Figure 6 contains a summary of the input and output data.

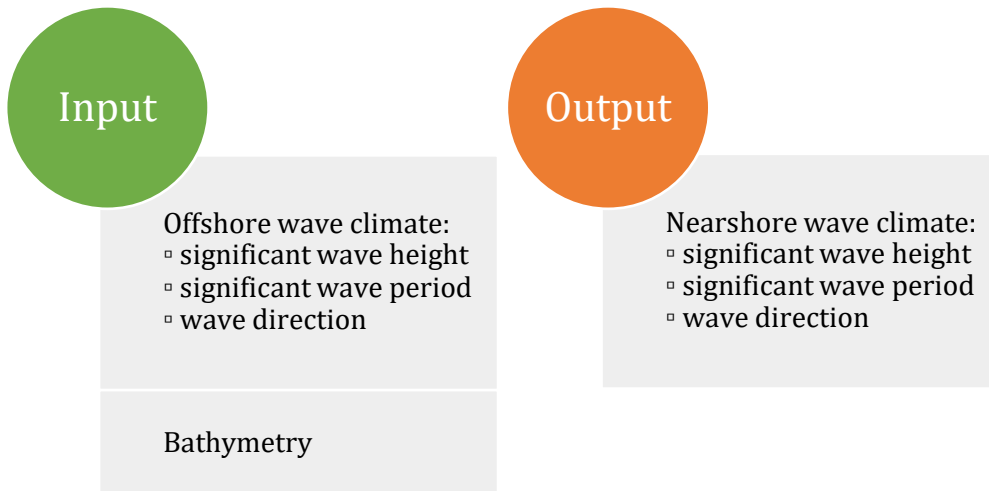


Figure 6. The needed input data and the obtained output data for the EBED model.

The EBED model has been validated, calibrated, and verified using detailed, high-quality data (Nam, et al., 2017). It has been employed using both field and laboratory data to demonstrate a good fit between calculated and measured waves. Three different field areas with sandy or sandy barred beaches were previously used to examine model performance. In these areas, multiple measurement stations existed. Validation with a lot of measuring points and long data sets increases the reliability. The model was also evaluated using laboratory measurements. Laboratory data can be measured and examined thoroughly giving a high accuracy. For the validation of the model, different indexes were used: coefficient of determination (r^2), relative root-mean-square error (*rel.rmse*), scatter index (*s.i*), and relative bias (*rel.bias*). Each of the validation indexes is further explained in Appendix B1. Previous model validation concluded that EBED provides reliable estimations of the nearshore wave climate based on these indexes. (Nam, et al., 2017)

4.2 LST:

Longshore sediment transportation

The total longshore sediment transport rate is estimated by the commonly used CERC equation through a FORTRAN program (US Army Corps of Engineers, 1984). The program is in this report called the LST model. The longshore sediment transport is obtained as a total rate across the surf zone given in terms of volume sediment transported per unit time, Q_{ls} . The CERC formula is based on the assumption that Q_{ls} is proportional to the rate of wave energy flux per unit time directed alongshore. Sediment transport is assumed to only take place due to currents generated by wave breaking, and currents from for example wind and tides are neglected. Regarding the mode of transport, it is assumed to be mainly suspended sediment in the surf zone. The sediment characteristics are represented in the formula by the relative sediment density. The CERC equation is expressed as Equation 10:

$$Q_{ls} = \frac{0.23g^{1/2}H_{sb}^{5/2} \sin 2\theta_b}{(s - 1)} \quad (10)$$

Where, g = acceleration due to gravity,
 H_{sb} = significant wave height at breaker line,
 θ_b = angle between wave crest and shoreline at breaker line,
 s = relative sediment density

The significant wave height, H_{sb} , and the angle, θ_b , where the wave breaks, are obtained from the wave energy flux conservation equation (Equation 10) and Snell's law (Equation 11) inserting the nearshore wave climate offshore the breakpoint (US Army Corps of Engineers, 1984). The two equations are presented below.

$$H_{s0}^2 C_{g0} \cos \theta_0 = H_{sb}^2 C_{gb} \cos \theta_b \quad (11)$$

$$\frac{\sin \theta_0}{C_0} = \frac{\sin \theta_b}{C_b} \quad (12)$$

Where, H_{s0} = significant wave height at the offshore point,
 H_{sb} = significant wave height at breaker line,
 C_{g0} = group velocity at the offshore point
 C_{gb} = group velocity at the breakpoint,
 C_0 = phase velocity at the offshore point,
 C_b = phase velocity at breakpoint,

θ_o = incident wave angle at the offshore point,
 θ_b = wave angle at the breakpoint

The needed input data for the nearshore wave climate is obtained from the EBED simulation results. To get the wave angle at the breakpoint for a particular stretch of shoreline, the input wave angle should be given with reference to the normal determined based on the representative shoreline orientation. Also, the ratio between the wave height and water depth at breaking should be given (taken to be 0.78 here). The program calculates the wave height and angle at the breakpoint from which the longshore sediment transport is determined. Figure 7 summarizes the needed input and the obtained output from the longshore sediment transport model.

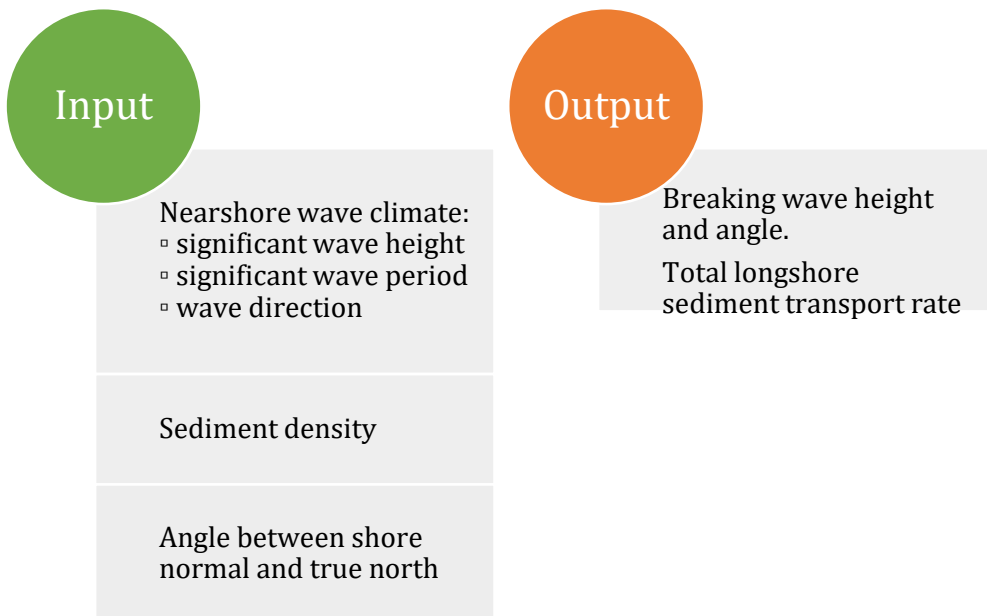


Figure 7. Input and output data for the LST model.

4.3 Cascade: Longshore sediment transport and long-term shoreline evolution

Cascade is a numerical model that simulates the longshore sediment transport and coastal evolution. The model simulates the evolution at the regional scale and the governing equations are solved numerically using a FORTRAN program. The longshore transport and coastal change can be simulated over hundreds of kilometres for with time periods from decades to centuries, which makes the model unique as a tool to study coastal evolution at the regional

scale. The calculations are done in an x - y -coordinate system describing the shoreline position along the coast. A boundary condition on each side of the defined model domain must be set. The shoreline is divided into cells, and the model calculates the shoreline position in each cell along the x -axis for each time step. (Larson, et al., 2002)

The longshore sediment transport rate Q is described by Equation 13,

$$Q = Q_o \sin 2 \left(\alpha_{br} + \alpha_b - \arctan \frac{\partial y}{\partial x} \right) \quad (13)$$

where the sediment transport amplitude is denoted Q_o (depends on the wave properties at breaking and the sediment characteristics similar to the CERC formula), the wave angle at breaking α_b , the regional shoreline orientation α_{br} (assumed to be zero), the shoreline position y , and the alongshore coordinate x . The shoreline position y can be obtained by solving Equation 13 in a combination of sand volume conservation equation (Equation 14):

$$\frac{\partial Q}{\partial x} + D \frac{\partial y}{\partial t} = q(x, t) \quad (14)$$

Where, D = active profile height for longshore transport,
 t = time,
 q = a source (sink) term varying in time and space

The model can handle the influence of several sediment sources and sinks within the system, such as river discharge. Sources and sinks need to be identified and assigned strength values before running the model. Other input data that need to be compiled are the nearshore wave climate, the position of the shoreline for a minimum of two different times, and the median grain size. Preferably, the input nearshore wave climate should correspond to the studied period of shoreline evolution, although often a generic climate is employed. In the present study the actual hindcasted nearshore wave climate was used.

The calculations are made successively along the shoreline and results in an output of average net longshore sediment transport for each year and cell, and the shoreline position at the final time step. The shoreline position will be given as an y -value for each corresponding cell in the x -direction. The output shoreline can then be compared with measured shoreline positions for calibration and validation of the model.

Two main model parameters were changed in the calibration process: the transport coefficient and the sediment transport rates (strength) for the river (source). The transport coefficient appears in the above equation (in Q_o) and has a recommended value of 0.2 with a maximum estimated value at 0.39 (based on the significant wave height) (Schoonees & Theron, 1996; Schoonees & Theron, 1993; Komar & Inman, 1970). When the model is calibrated and validated, the time series for the nearshore wave climate can be extended to predict the future evolution. Figure 8 shows the input and output regarding the Cascade model.

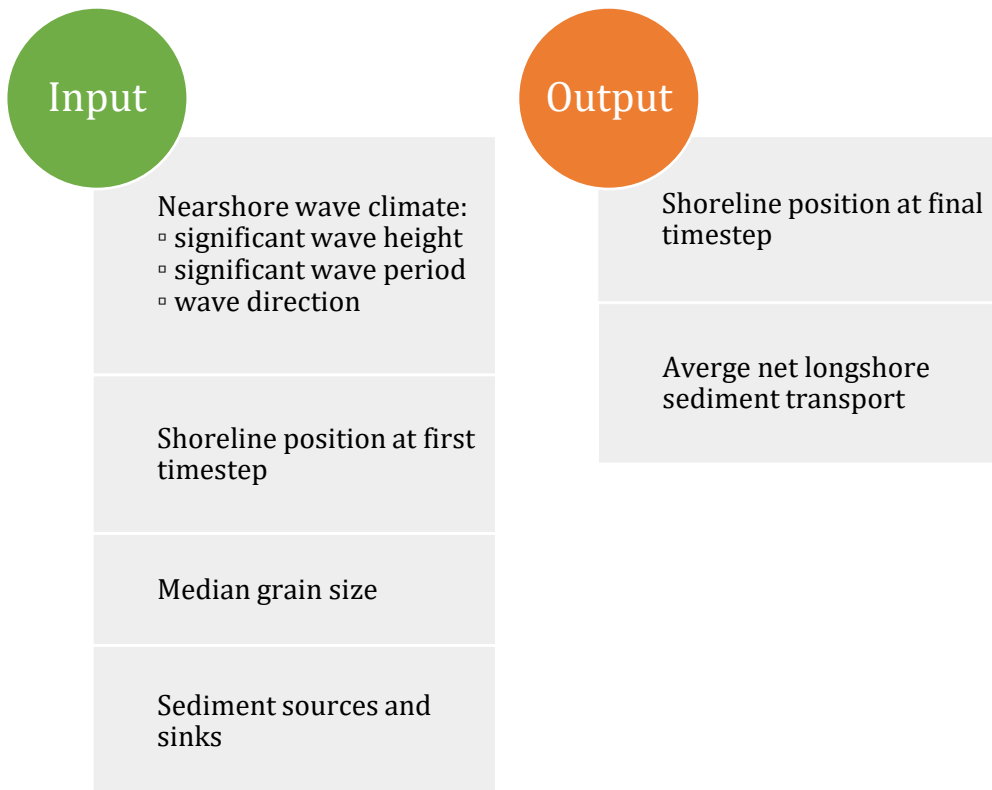


Figure 8. Input and output regarding the Cascade modelling process.

5 Data collection and analysis

Below, the data compilation and collection are presented. The obtained data have been analysed and evaluated before being presented in a suitable manner. The chapter starts with a detailed field survey that describes Cua Dai Beach. It is followed by beach profiles measurements, sediment analysis, bathymetry data, the offshore wave climate data, and at last shoreline position data are presented.

5.1 Field survey

As mentioned, the erosion problems are worst around Cua Dai Beach. A field survey was therefore conducted around this area to get a good perception of the scale of the current situation and future challenges. Along Cua Dai coastline, multiple different solutions for protection against erosion exist. In 2016, signs of erosion existed up to a distance of 7.6 km on the coast north of the river mouth (Tuan & Viet, 2016). The erosion problems was in 2018 observed to continue to propagate northwest along the coastline. Figure 9 shows a map over the Cua Dai coastline, where it is divided into different sections based on the type of currently used coastal protection. Table 4 contains a description of the type of coastal protection for each section. The existing coastal protections are a mix of soft, intermediate, and hard solutions. There are five resorts along Cua Dai coast, all protected with hard structures.

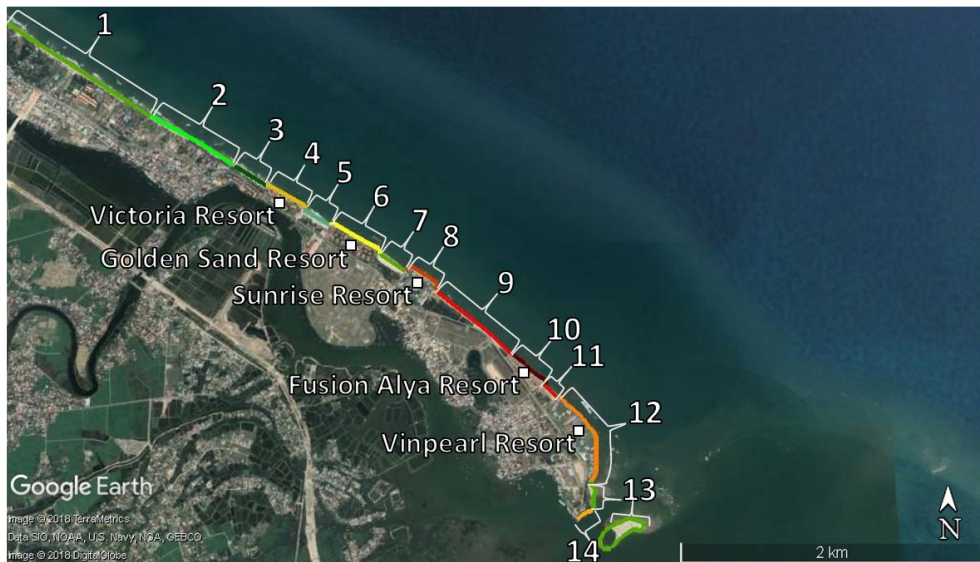


Figure 9. Coastline characteristics along Cua Dai and division into sections with regard to different coastal protection (Google Inc, 2018).

Table 4. Type of erosion protection for each coastal section marked in Figure 9.

Coastal section	Protection
1	Sandy beach
2	Sandy beach, geotubes
3	Sandy beach, sand bags, sand fence, geotube groins
4	Rubble revetment, T-shaped geotubes
5	Sandy beach, sand fence
6	Rubble revetment, L-shaped groin
7	Sandy beach
8	Seawall, rubble revetment
9	Concrete revetment
10	Seawall
11	Concrete revetment
12	Rubble revetment, T-shaped geotubes
13	Sandy beach
14	Rubble revetment

At the tip of the river mouth, revetments of rubbles are protecting the spit and preventing the erosion to approach the harbour located inside the river mouth (Figure 10). It is followed by a small sandy beach that is heavily affected by the currents created due to the river discharge (Figure 11).



Figure 11. A hard structure at the north part of the river mouth.



Figure 10. Sandy beach adjacent to Thu Bon River mouth in the north.

Each of the resorts has constructed their own erosion protection. The resort closest to the river mouth is Vinpearl resort, which is protected by a revetment of rubbles (Figure 12) together with geotubes. The geotubes lay in a T-shaped pattern below the water surface in the nearshore zone outside the hotel. Fusion Alya is the next resort when travelling north from the river mouth along the coast. The hotel was forced to close down due to a lack of finances to construct erosion protection. Figure 13 shows the current state of Fusion Alya. It reveals that the seawall which formerly protected the resort is heavily damaged, allowing waves to pass and causing buildings to collapse. Sunrise resort has also constructed a seawall but reinforced it with rubble revetment. Golden Sand and Victoria resort are both protected with revetments made of rubbles. Golden Sand has increased its protection by constructing an L-shaped groin at the most southeast end of the resort. Victoria resort has just as Vinpearl resort placed geotubes in a T-shape seaward of the hotel.



Figure 12. Rubble revetment protecting Vinpearl resort. Figure 13. Fusion Alya resort.

The government has funded the concrete revetment at the Cua Dai coast. It stretches along two parts: between Vinpearl and Fusion Alya resort, and between Fusion Alya and Sunrise resort. During the field survey in 2018 severe damages were observed. In multiple places, the revetment has started to collapse due to damaged caused by local scour. Figures 14 and 15 show the concrete revetment and an example of the damage, respectively.



Figure 14. Concrete structure.



Figure 15. Damaged concrete structure.

Between Sunrise and Golden Sand resort, and Golden Sand and Victoria resort there are two smaller sandy beaches. The beaches have retreated further inland along the resorts. Sand fences exist at the beach between Golden Sand and Victoria resort. The sand fence then continues northwest of Victoria resort, where sandbags and geotubes also are used as protection. The first part of the sandy beach northwest of Victoria resort is seen in Figures 16, 18, and 19. Figure 16 shows intermediate erosion protection sandbags. Figure 19 shows an example of a sand fence, and Figure 18 a geotube used as a groin. In the next part of the beach, two layers of geotubes work as erosion protection (Figure 17). The final part of the sandy beach has currently no other erosion protection than the beach itself, but is today also affected by erosion (Figure 20). Signs of erosion of the beach could be observed up to around 7 km from the river mouth on the northern side.



Figure 16. Protection with small sandbags.



Figure 17. Protection with geotubes.



Figure 18. Groin made of geotubes.



Figure 19. Sand fence.

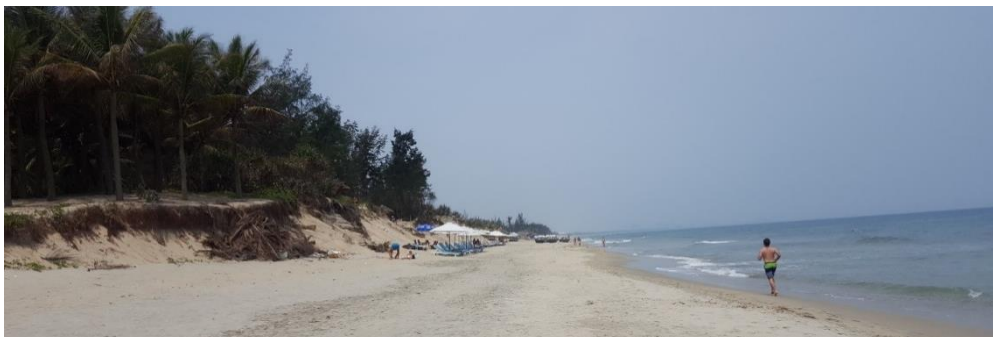


Figure 20. Erosion situation at Cua Dai coast looking north.

South of the river mouth, there is a sandy beach. In the area close to the river mouth, a part of the beach has eroded away. Further south the erosion effects subside. The south beach area is currently undeveloped, and there are no structures. Just a few kilometres upstream the mouth of Thu Bon River, many sand mines were observed (Figure 21).



Figure 21. Sand mine around 2 km upstream the river mouth.

5.2 Beach profiles

The beach profile data consist of earlier measured profiles (Duong, et al., 2017) together with recent profiles measured in conjunction with this study. Figure 22 shows the location of each of the profile surveys. A total of 27 profiles belong to the earlier measured profiles. These were measured the year 2014 and 2016, and some also in 2017. Profiles P1 to P23 are measured in the nearshore zone and on the foreshore (orange lines). Profile P24 is for the river mouth (blue line). The profiles P25 to P27 (white points) were all obtained in October 2016, where the measurements were taken across the beach and over a part of the nearshore zone before and after a storm event.

The most recent profiles, P28 to P31, are from March 2018 (white points in Figure 22). The profiles from 2018 show the beach and a part of the nearshore zone. The profiles were measured with a Leica TS02, which is an electronic optical distance measurement instrument with a built-in GNSS. The seaward measurement distance was limited by the height of the person conducting the study, also depending on the wave and tide conditions. In Appendix A1 all the profiles are presented.

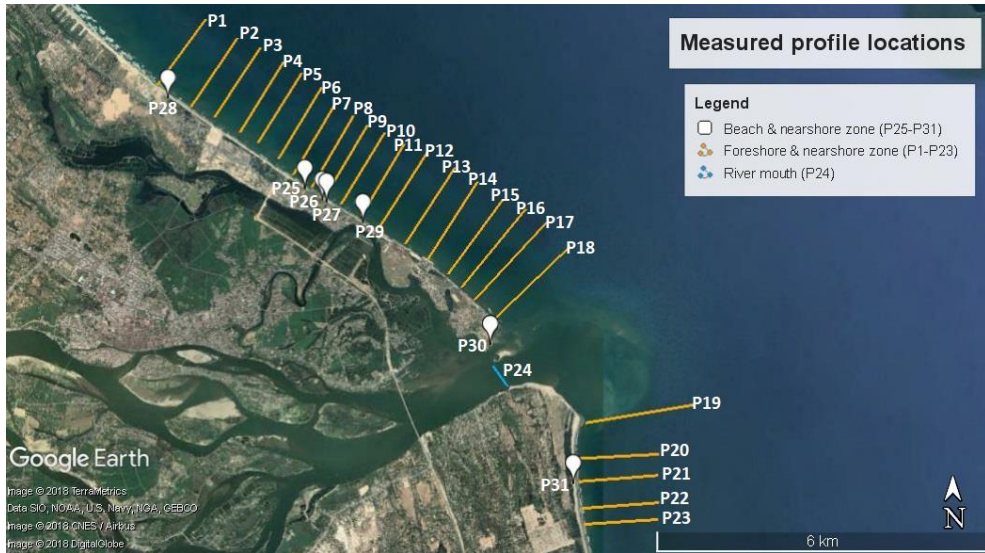


Figure 22. The location of the measured beach profiles P1 to P31 (Google Inc, 2018).

5.3 Sediment analysis

Sediment samples were collected in March 2018 at four different locations (A, B, C, and D) illustrated in Figure 23. Location A is situated south of the river mouth and site B just north of the river mouth. The site location C is close to the end of Cua Dai Beach and site D north of Cua Dai. At each location, three different samples were collected along the sandy beach profile, see Figure 24. One sample was taken at the coast bordering to the beach (A1, B1, and C1), another at the shoreline (A2, B2, and C2), and the final one in the surf zone (A3, B3, and C3). The depth and location of the samples in the surf zone were collected by wading into the sea and diving to the bottom. Therefore, it was limited by the height and diving capability of the person collecting the sample, as well as influenced by wave and tide conditions.

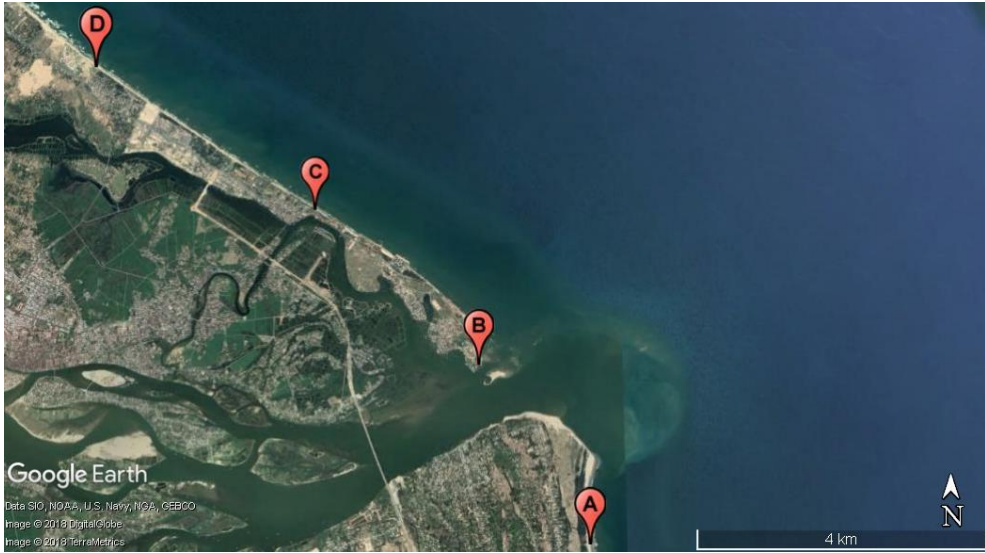


Figure 23. Sediment sample locations A, B, C and D (Google Inc, 2018).



Figure 24. Locations of sampling points along beach profile.

The sediment samples were analysed in the lab. First, the samples were dried in an oven at 105°C for four to nine hours depending on the water content. The samples were then filtered using seven different sieves with the filter sizes 1.4, 1.0, 0.63, 0.32, 0.20, 0.10 and 0.06 mm. When filtering, the shaking of the sieves was done manually. The trapped sediment in each sieve were subsequently weighted. The analyses resulted in grain size distribution curves for each of the samples, which can be found in Appendix A2.

5.4 Bathymetry

The bathymetry over the area was obtained from the study made by Duong (2018), see Figure 25. The area has been rotated 60 degrees anticlockwise from true north, in order to be aligned with the general trend of the coastline. In the grid over the area, a specific depth value was assigned to each cell. The derived bathymetry is based on a combination of different types of input data. Measured bathymetry from 2016 and 2017 at locations nearshore and measurements further offshore was interpolated and was then combined with digitized nautical maps.

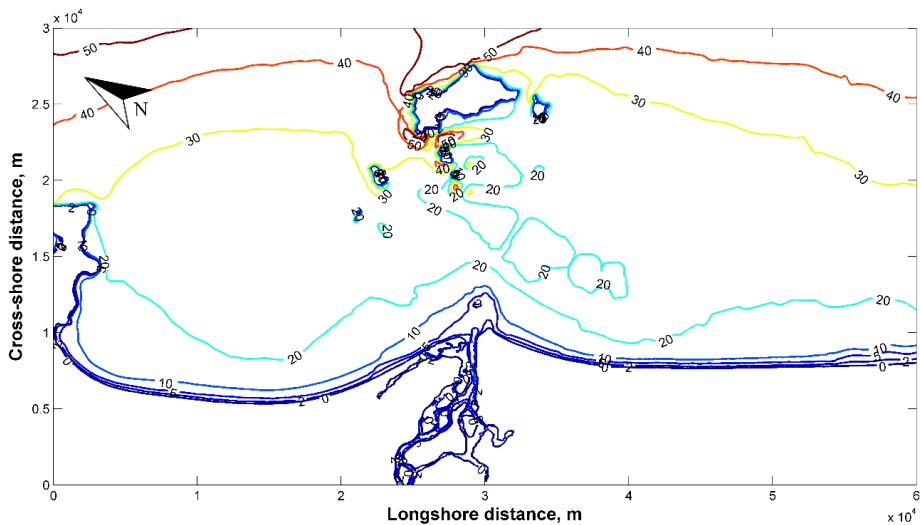


Figure 25. Bathymetry of the study area.

5.5 Offshore wave climate

The offshore wave data are based on wind data using a hindcast approach with a numerical wave generation and propagation model, extracting the wave climate at a location northeast of the Cham Islands at 56-m water depth. The wind data were obtained from the Japanese Meteorological Agency. Data on wave height, period, and direction were simulated with the model SWAN for every third hour from the year 1988 to 2004, and every hour for the period 2005 to 2017 (Duong, 2018). A wave rose illustrating the distribution of the direction and significant wave height is shown in Figure 26. The dominant wave direction is from the northeast to east-northeast, which usually occurs in October to February. During May to August, the wave direction is usually from the east-southeast. The remaining months the dominant wave directions are

from the east. The average direction of the incoming waves for each month is seen in Figure 27.

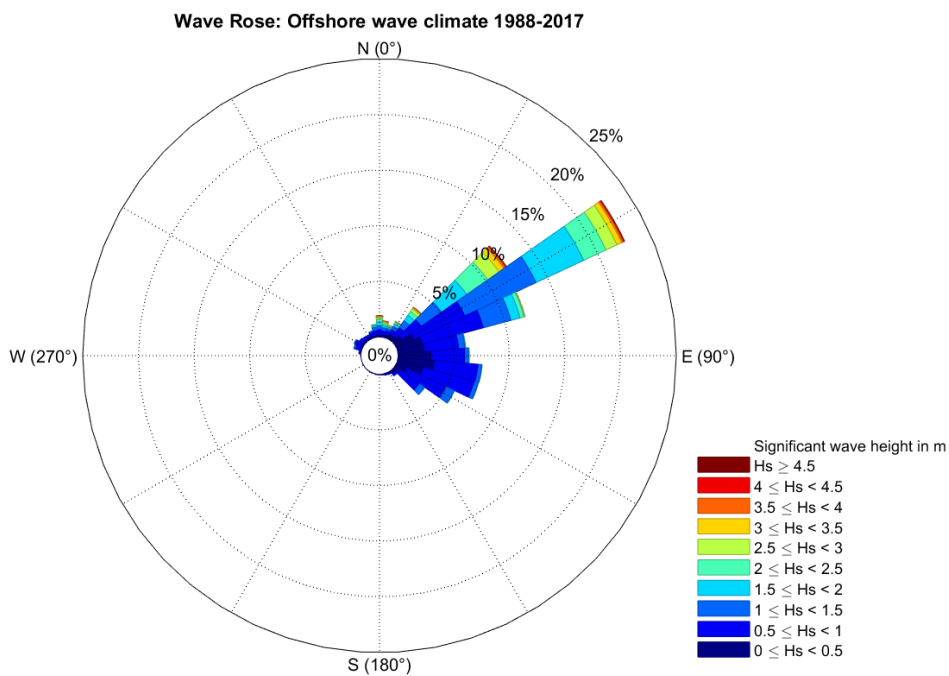


Figure 26. Wave rose for the offshore wave climate 1988 to 2017.

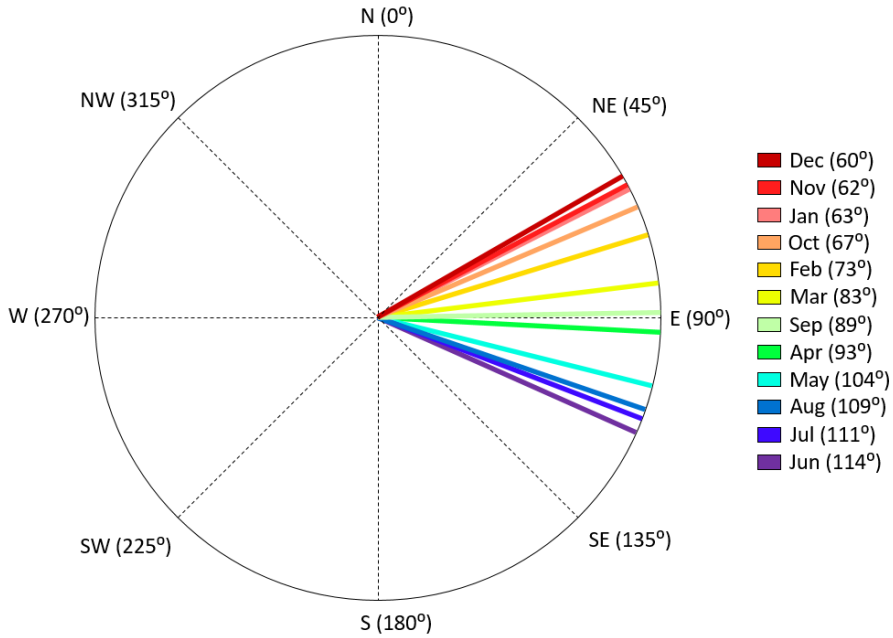


Figure 27. The average direction for the incoming waves per month for the years 1988 to 2017.

The yearly variations in the significant wave height and wave period are displayed in Figures 28 and 29, respectively. In Figure 28 it is shown that the wave height is highest during the winter months and it peaks in December. The height is lowest through the summer. Figure 29 shows that the wave period approximately follows the same pattern as the wave height and it peaks in December. The lowest period occurs in the beginning of the summer. Based on the hindcast data for the years 1988 to 2017, the depth of closure for the area was calculated to 8.6 m using Hallermeier's equation. In Appendix A3, Table A2 contains the monthly mean of the average significant wave height, maximum significant wave height, and average wave period. Table A3 shows the yearly significant wave height that is exceeded twelve hours per year with the corresponding period.

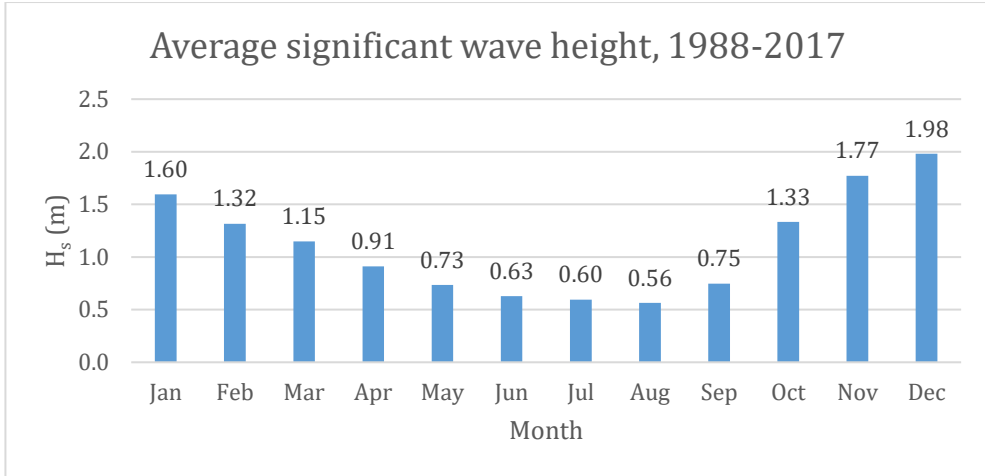


Figure 28. The average significant wave height for each month during the years 1988 to 2017.

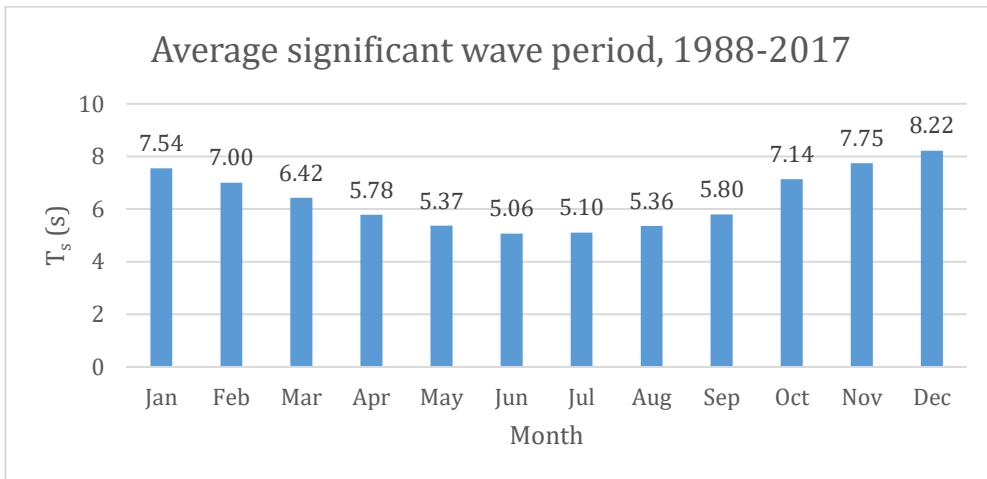


Figure 29. The average significant wave period for each month during the years 1988 to 2017.

5.6 Shorelines

The shoreline positions in an x - y -coordinate system for four different dates were obtained using Google Earth satellite images digitized with the software Grapher (Google Inc, 2018). Figure 30 shows the shoreline positions for these dates. The shorelines are divided into three different zones, and a detailed figure for each of the zones is shown in Appendix A4 (Figure A36 to A38). The figure shows the shorelines in non-scaled condition. Each shoreline has been rotated 60 degrees anticlockwise from true north.

Due to lack of satellite images over the whole area of interest, the shorelines were obtained using images from different dates. These combinations were made with time steps as small as possible. The lack of older satellite images explains the larger time step for the shoreline "2002-2004". The dates of the image representing the line "2002-2004" are 21st of April 2002 and 10th of November 2004, and for "2011-2012" 8th of February 2011 and 10th of April, 11th of June and 21st of September 2012. The two other shorelines are from the years 2014 and 2017 respectively. The line "2014" is represented by the satellite images dated 19th of March and 6th of July 2014, and "2017" by 10th of April, 14th of June and 23rd of June 2017.

In Figure 30, a retreating shoreline can be observed closest to the river mouth (see Figure A37 in Appendix A4). A slight accretion of the beach is shown at around 7 to 20 km along the *x*-axis (Figure A36, Appendix A4). After the years "2011-2012" the shoreline is rather stable in the north of the river mouth due to the construction of hard structures. Figure 30 indicates a retreating shoreline even south of the river mouth at 31 to 33 km (Figure A38, Appendix A4). Between "2002-2004" and "2011-2012", accretion of the beach starts around 35 km south and continues all along the studied shoreline. After "2011-2012" the shorelines "2014" and "2017" indicate a more stable behaviour.

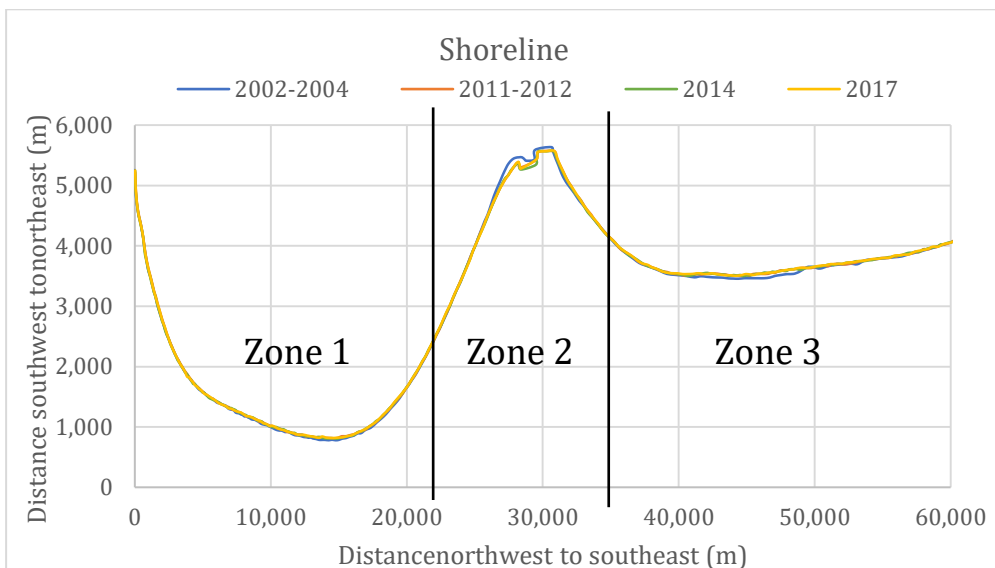


Figure 30. The shoreline position for the years 2002-2004, 2011-2012, 2014 and 2017. The river mouth is located around 28,000 m on the *x*-axis. The shoreline is divided into Zones 1, 2, and 3. A detailed illustration of each of the zones can be found in Appendix A4.

6 Modelling processes

As previously discussed, three different models were set up for the study area: EBED, the alongshore sediment transport model (LST), and Cascade. Cascade also calculates the longshore sediment transport together with the shoreline evolution. The LST model and Cascade are limited by the number of output locations for the nearshore wave climate resulting from the EBED simulations. The two natural boundaries, Son Tra in the northwest and Tam Hai Island in the southeast, are the limits in the longshore direction, which extends for a coastline length of over 80 km. EBED is a time-demanding program to run for large grids and long time periods. Due to limited computational resources, the studied coastline length was set to around 60 km. It is essential to include the influence of Cham Islands; therefore, the grid needs to include the deep-water area seaward of Cham Islands, which implies a cross-shore extent of the grid of 30 km. The longshore sediment transport rate model (LST model) and Cascade are also implemented along the 60 km long coastline. Figure 31 shows the area that was modelled.

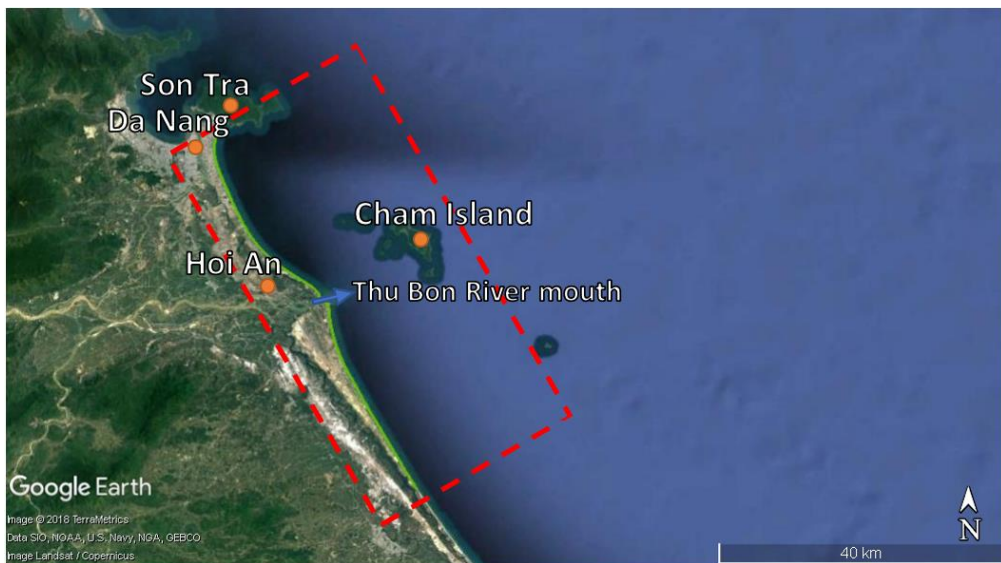


Figure 31. Study area for the modelling. The red rectangle shows the model area for EBED, and the green line the extent of the coastline for the LST and Cascade models.

6.1 EBED

6.1.1 Model implementation

The grid area created for EBED was 60 km x 30 km. It is of importance to try to reduce the total amount of cells in the grid due to long simulation times; however, the quality and resolution of the output must also be satisfactory. The change in bathymetry in the longshore direction is not changing as much as in cross-shore direction, which is seen in Figure 25. Hence, the grid cell size in longshore direction can be longer than in cross-shore direction. Different cell sizes were tested; 100 m x 15 m, 100 m x 30 m, 100 m x 50 m, 100 m x 100 m. The cell size 100 m x 50 m resulted in a satisfying quality of the output with regard to the duration of the simulations, which gives 601 cells in both x - and y -direction. The bathymetry needed to be interpolated to the chosen grid size, yielding depth values in all cells.

The EBED model has the zero-degree axis located to the east. Waves incoming from the north has a negative angle and waves from south a positive angle. EBED can only consider waves with an incoming angle in the range of -90 to 90 degrees. Therefore, to include as many waves as possible rotation of the grid is necessary, where the zero-degree axis should be perpendicular to the coastline. A rotation of 60 degrees anticlockwise was made to align the grid with the main trend of the coastline, resulting in an x -axis in the northwest to southeast direction and an y -axis in the southwest to northeast direction.

The bathymetry coordinates and incoming wave angle were corrected with the help of MATLAB and Excel to fit the required setup of EBED. Due to the limitations of EBED to calculate for incoming waves near 90 degrees and above, angles which are not within the range of -85 to 85 degrees are corrected to -85 and 85 respectively. 857 values were corrected, out of a total of 162,889 values for the entire period.

In order to reduce the simulation duration further, as well as making the input data consistent and have the same hourly input values, 2/3 of the wave data between 2005 and 2017 was removed; hence, every third hour is simulated. Eleven points were chosen for the output of the nearshore wave climate to get a satisfactory description of the waves alongshore in the region. The locations of the points can be seen in Figure 32. The 11 points were chosen at a depth of 9 m, which corresponds to the depth of closure; also, wave breaking is assumed to be negligible at this depth. Point six were first located opposite the river

mouth; then, five points on each side of the river mouth were set, where the distance between each point is 5000 m on the x -axis.

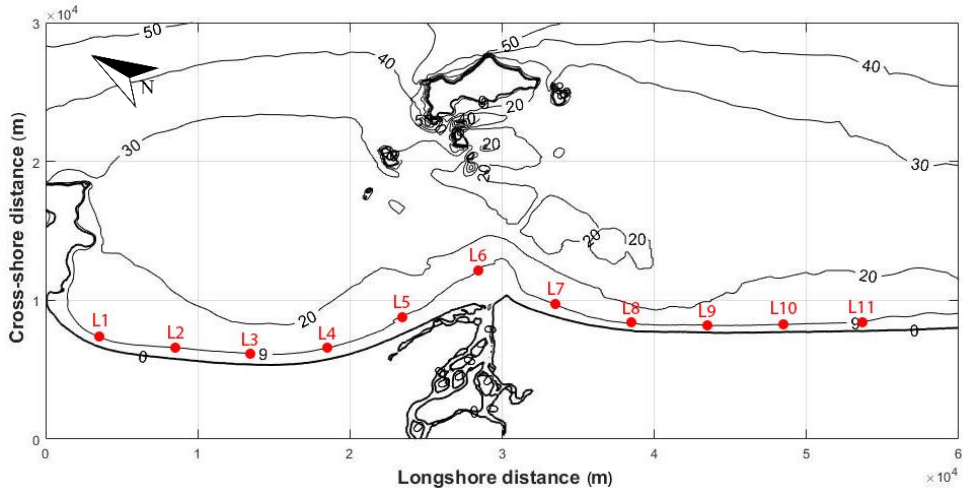


Figure 32. The spatial distribution of the points where the nearshore wave climate was simulated.

6.1.2 Sensitivity analysis and validation

There was a lack of measured wave data in the area, and only three different periods of measurements exist. Moreover, the periods are only for a few days and the measurements are taken every hour. A sensitivity analysis for the calculated waves to changing K (decay coefficient) and Γ (stable wave height coefficient), which influence the wave breaking in the nearshore zone, was performed. Changing K and Γ in the defined range by Nam et al. (2017) did not make much difference for the calculated waves. The values for K and Γ were therefore set to the values 0.15 and 0.45, which is in the middle of the suggested range.

Nine different measurement sets from three different periods in the years 2016 and 2017 were used for the model validation. The year 2016 has measurements from two time periods, and 2017 from one. The measurement stations A1, A2, and A3 are from the first period, which is between 11th to the 14th of October 2016, have measurements every hour. Stations B1, B2, and B3 are from the second period in the year 2016 and measurements were taken every hour, except from the 19th to the 26th of October. The period between the A- and B-measurements was interrupted by a storm making it impossible to conduct measurements. Stations C1 and C2 are from the 20th to the 25th of March 2017,

and C3 from the 15th to the 25th of March 2017, with measurements every hour. The locations of the measurement stations are shown in Figure 33.

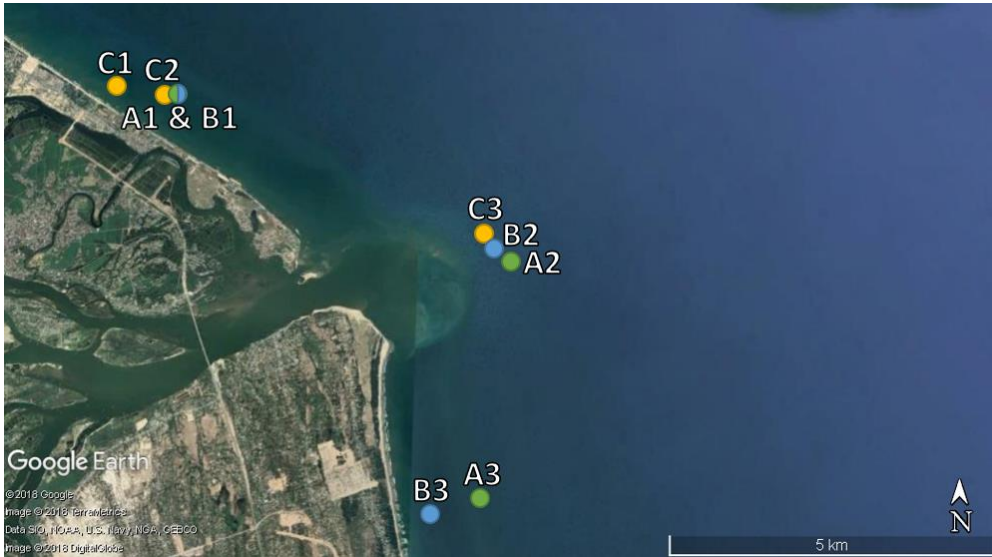


Figure 33. Location of the measurement stations.

The validation for each of the measurement stations can be seen in Figures 34, 35, and 36, where the measured significant wave height is compared to the calculated significant wave height. The figures also include the significant wave height of the deep-water waves. To analyse the validation results several different indexes are used: coefficient of determination (r^2), relative root-mean-square error (*rel.rmse*), scatter index (*s.i*), and relative bias (*rel.bias*). The obtained values for the different indexes can be seen in Table 5.

The first validation period yielded rather good results when comparing measured and computed wave heights. There is one peak in A1 and A2 that EBED does not predict, see Figure 34. However, viewing the deep-water wave height there is no peak in this record either, which means the input wave data may not be entirely correct.

Measured and calculated wave height - 2016 period 1

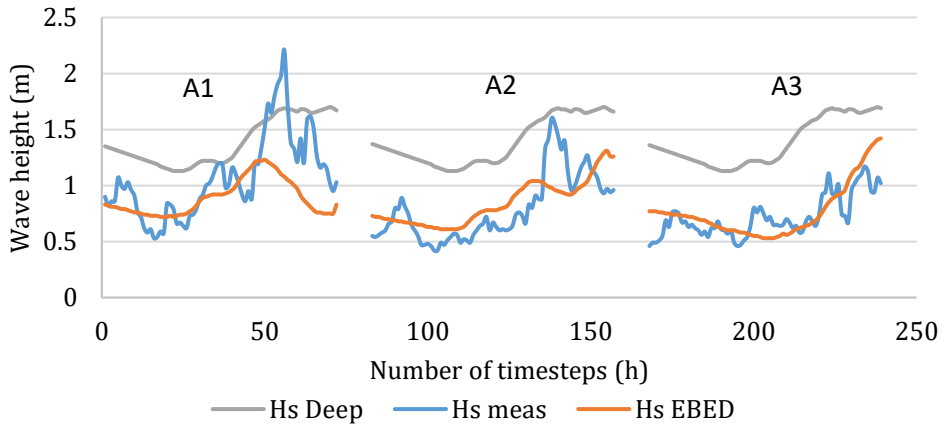


Figure 34. The first validation period. A comparison between measured, calculated, and input deep-water waves at three different locations.

In the second validation period, there is a peak that the computed wave height exaggerates compared to the measured value, see Figure 35. The calculated peak is slightly higher in B1 and B3, and the peak is almost 15 time steps to early. In B2 the difference between measured and computed value of the peak is substantial. It could be because B2 is located just outside the river mouth; the river probably has an increased flow due to the recent storm. Therefore, the river flow may affect the wave height at this location. More likely is that the bathymetry just outside the river mouth experiences considerable change, especially during a storm, which makes the actual and modelled bathymetry different. It should be noted that the measurements were essentially made at a point, whereas the grid size in EBED yields an average depth over a substantial area (see discussion below). This requires rather smooth bathymetric changes to make model comparisons with measurements reasonable; this is probably not the case near the river mouth. A smaller grid size in EBED would probably improve the agreement, if the correct bathymetry is available.

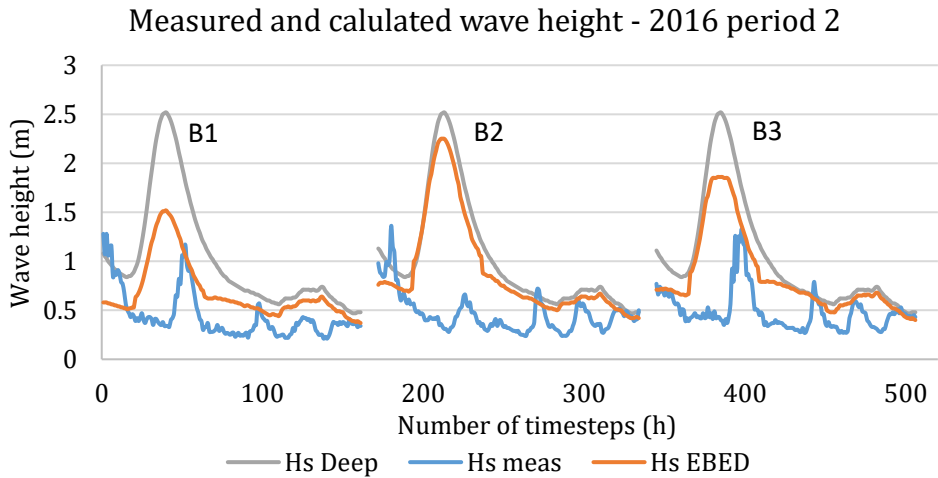


Figure 35. The second validation period. A comparison between measured, calculated and input deep-water waves at three different locations.

The third validation period is during a calm period which can be seen in Figure 36. The wave height is relatively small, but the calculated height is overestimated almost over the whole period. However, this period has the best r^2 value as can be seen in Table 5.

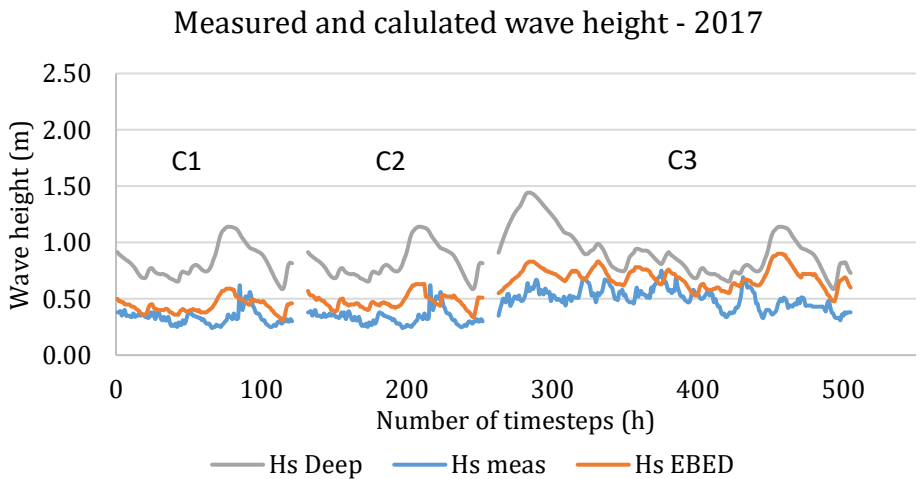


Figure 36. The third validation period. A comparison between measured, calculated and input deep-water waves at three different locations.

Table 5. Quantification of the model performance according to different statistical measures.

	A1, A2, A3	B1, B2, B3	C1, C2, C3	Total
r²	0.39	0.02	0.46	0.11
rel.rmse	27.76	112.77	42.74	68.65
s.i	0.27	0.84	0.29	0.51
rel.bias	-0.03	0.77	0.36	0.3

To assess the uncertainty of the wave height calculated in EBED, the water depths for the output points in the model were compared with the average water depths for each of the measurement stations. Table 6 shows the result of this comparison. For five of the stations, the values of the depth employed in EBED and measured depths are relatively similar. The error varies between 0 and 7.5 m, with a mean error of 2.4 m. Station A2 has a 7.5 m larger measured depth compare to one used in EBED. A larger measured depth also applies to station C1 (1 m), C2 (0.5 m), and C3 (1 m). When looking at Figure 34 and 36, it is shown that the calculated significant wave heights are slightly higher than the measured values, which is reasonable since larger depths for the measured values will result in lower wave heights (assuming correct input wave conditions).

Lower measured depths than the depths used in EBED occur for station A3 (2.9 m) and B3 (3.7 m). Figure 34 and 35 shows no specific trends related to this fact. The stations A2, A3, B2, and B3 are contributing to more substantial errors. These are all from 2016 in October around a stormy period, which complicated the measurements. Measured values are missing at station B2. Tidal variation also influences the depth at the measurement stations.

Table 6. Depth employed in EBED compared to the measured depth at the measurement stations.

	A1 & B1	A2	A3	B2	B3	C1	C2	C3
Depth employed in EBED (m)	7.9	6.3	16.0	2.9	11.9	5.0	7.5	5.0
Average measured depth (m)	7.9	13.8	13.1	-	8.2	6.0	8.0	6.0

In the validation, it is shown that at some locations, EBED computes waves similar to the measured. The location which had the most substantial error was the location outside the river mouth. It could be due to the effect of river flow or changes in bathymetry. Sediment deposits outside the river mouth create spits, sandbanks, and shoals, which will affect the wave transformation. In the EBED model, the same bathymetry is used over the whole 30 years, which could be inaccurate in areas close to the river mouth. The lack of measured waves is an issue for the validation where not many days of measured data exist. The maximum length for a measurement period was 11 days. The few peaks in the validation that do not agree with the measured data could be due to error in the hindcasted offshore waves. However, with the data available this cannot be established.

6.1.3 Result and analysis

The calculated wave fields (significant wave height) for the whole area are shown in Figures 37 and 38, where the average input wave conditions for December and June were used, respectively. December and June have the most marked differences in incoming wave height and angle as discussed in the previous chapter, see Figure 27. In the winter months, the waves approach from an east-northeast direction, which is illustrated in the December wave climate (Figure 37). The influence of Cham Islands on the wave height at the river mouth for these months can clearly be seen in the figure. The highest waves occur during the winter months; hence, the Cham Islands reduces the incoming wave height with about 50 % in the nearshore area around the river mouth for the studied wave conditions. However, there will be shoaling effects in the nearshore as the waves approach the surf zone. In Figure 37, the input

deep-water wave is 1.98 m with a wave period of 8.22 m, approaching at an angle of 60 degrees from the north.

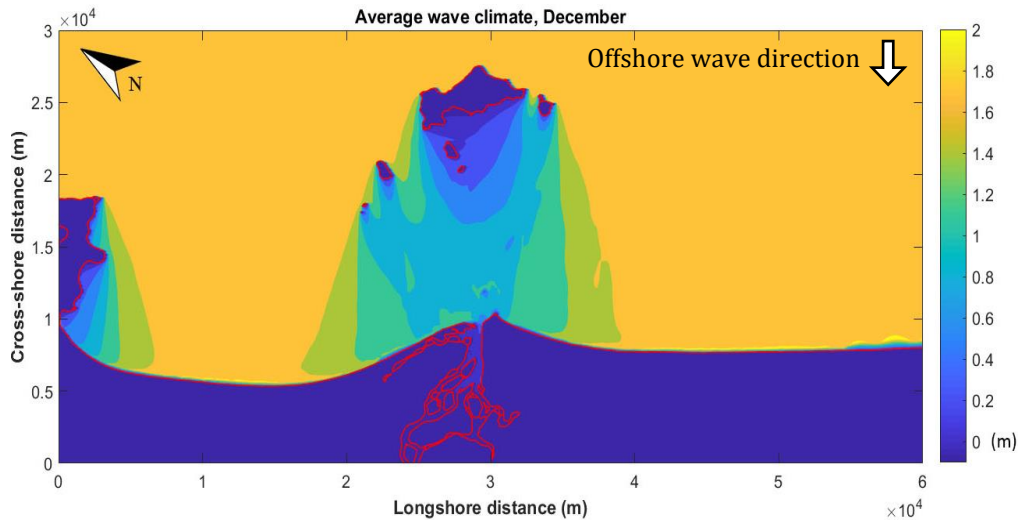


Figure 37. Simulated wave field for average input wave conditions in December, where the significant wave height is shown.

In June the incoming deep-water waves have an average height of 0.63 m, with a period of 5.06, and an incoming angle of 114 degrees true north, which corresponds to an east-southeast direction. The wave field in the area can be seen in Figure 38, where the Cham Islands do not influence the wave height at the river mouth anymore; also, the average wave height in the summer months are much smaller. Thus, these waves will not generate as much sediment transport as during the winter months.

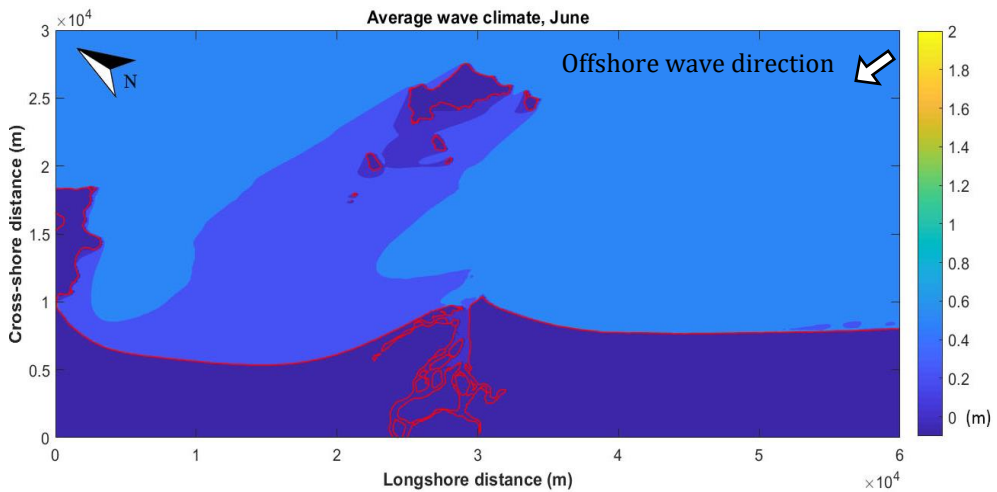


Figure 38. Simulated wave field for average input wave conditions in June, where the significant wave height is shown.

The wave field for the average input wave conditions based on the whole period is shown in Figure 39, where it can be seen that the south side of the river mouth are exposed to the deep-water waves with no protection from the Cham Islands. The average deep-water wave height is 1.1 m with an incident angle of 86 degrees true north.

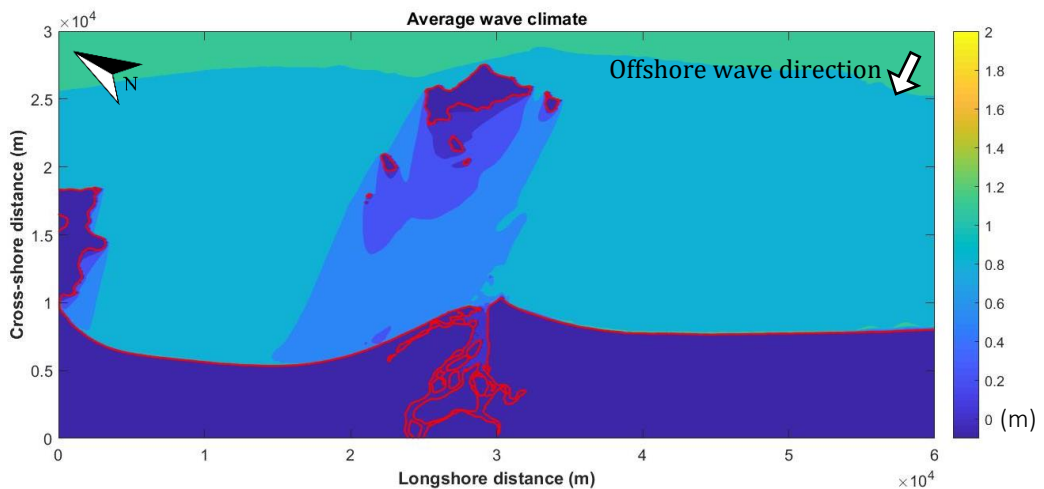


Figure 39. Simulated wave field for average input wave conditions based on the whole period, where significant wave height is shown.

The result of the simulation for the average significant wave height at the 11 locations of interest is shown in Figure 40. It is possible to see the influence of Cham Islands at locations 5, 6, and 7, and even slightly at location 4 and 8.

The locations are at a depth of 9 m, which means that the shoaling effects will increase the wave height somewhat before breaking occurs.

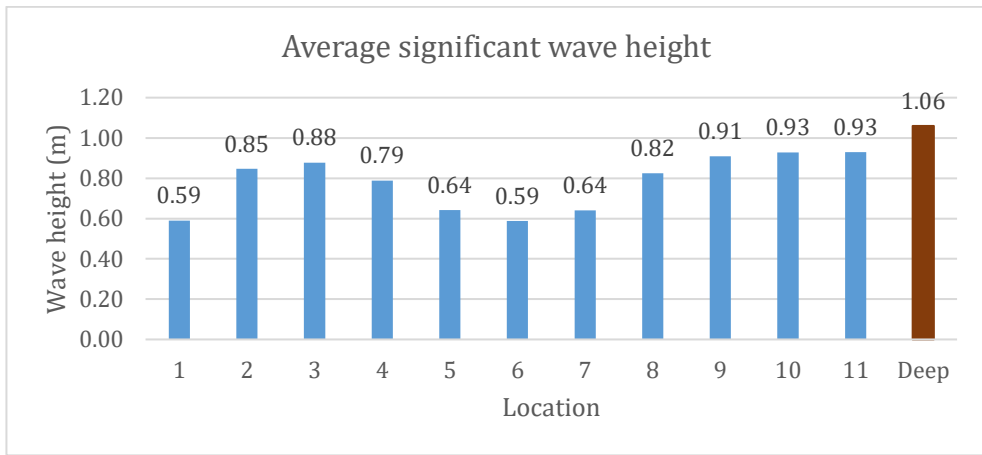


Figure 40. Average significant wave height at each studied location and input deep-water wave height.

The average monthly significant wave height at each location is shown in Figure 41. It can be seen how Cham Islands influence the wave climate in the winter months, see the curved lines in Figure 41. In the summer months, the lines are quite straight, which indicates the wave heights are more evenly distributed along the coast.

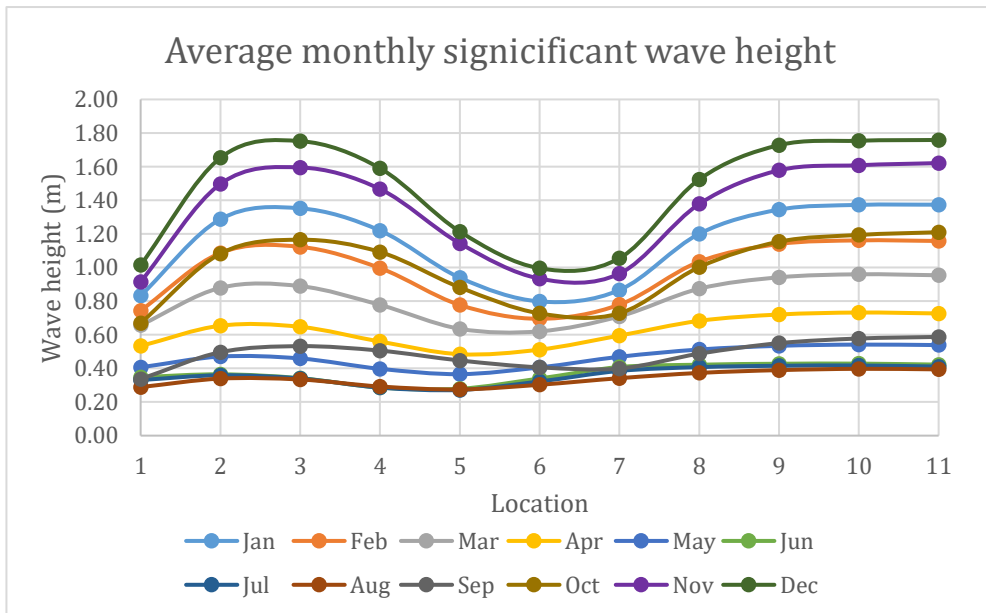


Figure 41. Average monthly significant wave height at each studied location.

6.2 LST

6.2.1 Model implementation

To calculate the longshore sediment transport in each location point with a given nearshore wave climate from the EBED simulation results (L1 to L11), a FORTRAN program was used. It employs the CERC equation, Snell's law, and the wave energy flux conservation equation with the output result from EBED described in section 5.1.3 to calculate the sediment transport rate. The angle between true north and the normal to the shoreline is also measured for each point and used as input in the program. The normal is drawn perpendicular to the local shoreline orientation. Appendix B2 contains the input angle for each of the studied locations together with an illustration of how the angle was determined. The model does not consider the river as a source of sediment.

6.2.2 Result and analysis

The annual average net sediment transport direction can be seen in Figure 42. The arrows indicate the direction, where a larger arrow size denotes a larger magnitude of net sediment transport. The amount of net sediment transport is given in Table 7, where a positive value corresponds to movement in the positive longshore direction, and a negative value in the opposite direction.

According to the calculated net longshore sediment transport direction (Figure 42), Cua Dai beach is affected by erosion, since the transport direction is northwest in L5 and southeast in L6. Between L3 and L4 there should be accretion as a result of two opposite transport directions at those locations, as can be seen in Figure 30 in section 5.6. It correlates with the observed shoreline evolution and previous study made by Do et.al (2018), where accretion can be seen between L3 and L4, and erosion between L5 and L6. The locations L8 to L10 are very sensitive to the input shoreline angle, indicating a system in dynamic equilibrium. If the angle is changed only one degree, the transport direction switches and/or the amount of sediment transport increases or decreases markedly. This indicates that at these locations the net sediment transport is close to zero.

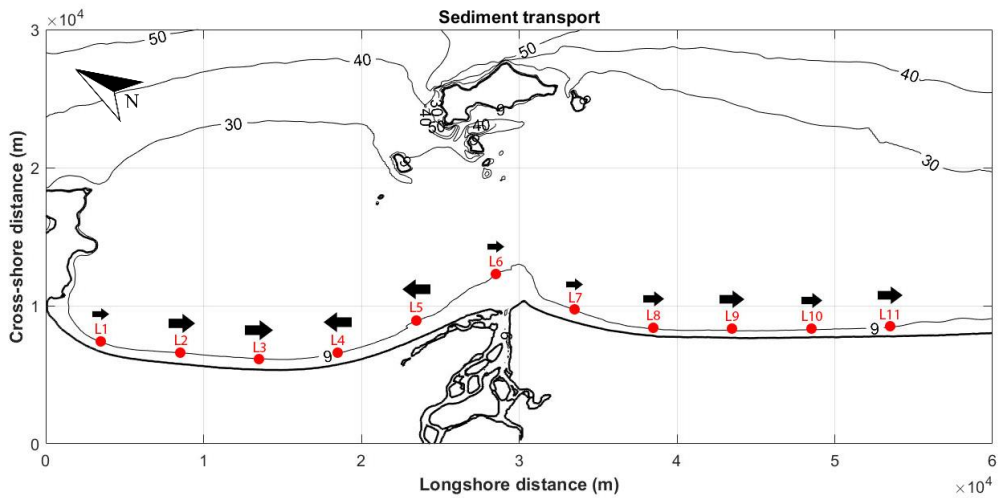


Figure 42. Annual average net sediment transport magnitude and direction.

Table 7. Annual average net sediment transport at each location, where a positive value indicates movement in the direction of the x-axis.

	L1	L2	L3	L4	L5	L6	L7	L8	L9	L10	L11
Annual Average ($m^3 \times 10^3$)	21	178	220	-210	-190	20	28	31	18	43	63

The net sediment transport direction changes during the year, which is shown in Figure 43 where a comparison between net sediment transport directions in June and December can be seen. The change in transport direction is due to the difference in mean angle of the incoming waves during the summer and winter months associated with northeast and southwest monsoon, respectively. Moreover, net sediment transport is much greater in the winter months, because of higher waves during northeast monsoon. For the average net sediment transport per location and month, see Table 8.

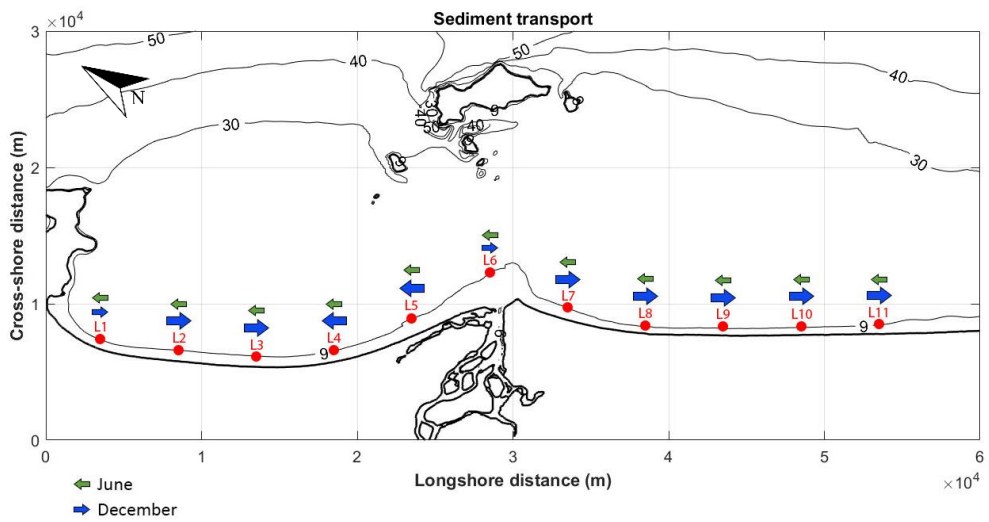


Figure 43. Average net sediment transport magnitude and direction for June and December.

Table 8. Average net sediment transport for June and December, where a positive value indicates movement in the direction of the x-axis.

	L1	L2	L3	L4	L5	L6	L7	L8	L9	L10	L11
June (m³ x 10³)	-4	-5	-3	-2	-2	-5	-8	-9	-9	-8	-7
Dec. (m³ x 10³)	14	62	62	-66	-56	7	19	27	22	18	20

6.3 Cascade

6.3.1 Model implementation

Measured shorelines are needed to compute the long-term regional sediment transport rate with Cascade; thus, past shorelines were digitized using images from Google Earth and the software Grapher. The coastlines obtained was denoted as “2002-2004”, “2011-2012”, “2014”, and “2017”, which are shown and described in the previous section 4.6. The shoreline “2002-2004” was used as the start shoreline for the simulations.

The wave climate in each location was described in section 6.1.3 with data starting from the year 2002 used as input. The same grid setup and rotation were used as in the EBED simulations, yielding an x -axis along the coast in the northwest to southeast direction and y -axis in the southwest to northeast, see Figure 44. The cell size in the x -direction was 250 m, resulting in 201 cells alongshore.

Two boundary conditions were set in the model, called “1” and “2” in Figure 44. Number “1” is at the border to Son Tra in the northwest. The boundary condition at this point is set to a constant y -value (i.e., shoreline position), since it was observed from measurements that the shoreline is approximately fixed at this location. It was more difficult to set the boundary condition in “2”, since there was no natural boundary or observed behaviour here. After some trials, the boundary condition was set to zero sediment transport, which seemed to reasonably well reproduce the shoreline response. Other tested boundary conditions yielded similar behaviour, although less good compared to the zero-transport condition.

The river discharge was added in the model as a distributed sediment source, and the width of the river discharge was set to 500 m (a width of two cells). The model does not describe the river mouth in detail and a constant source strength was specified without trying to relate the river transport to the flow. Other detailed information, such as structures for erosion protection along the coastline, were neglected in the model, since the main purpose was to describe the shoreline evolution at the regional scale. The entire modelled shoreline is assumed to consist of sandy beaches with a median grain size 0.215 mm, which is the average value obtained from the sediment analysis.

The future scenarios are modelled by prolonging the wave climate with the data from the previous 28 years (1988 to 2017). The wave climate is therefore

assumed to follow the same behaviour in the future as in the past. Two output years for the future shorelines were chosen. The first output year is 15 years after 2017 (2033), and the second is 30 years from 2017 (2048).



Figure 44. Illustration of the coordinate system and location of boundary conditions for the Cascade model (Google Inc, 2018).

6.3.2 Calibration and validation

The calibration of the model was performed by comparison with the shoreline denoted as “2011-2012” obtained from the satellite images. The transport coefficient and the sediment transport through the river discharge was the two parameters that were changed in the calibration process. A suitable value of 0.25 for the transport coefficient was established, which is a reasonable value according to previous studies. Regarding the river sediment transport, a value of $0.009 \text{ m}^3/\text{s}$ ($281,000 \text{ m}^3/\text{year}$) was found to give a reasonable fit. It is a value in the low range of $280,000$ to $430,000 \text{ m}^3/\text{year}$, which are estimated values after a reduced sediment transport due to sand mining and dam construction (Fila, et al., 2016). Note that input river sediment transport to Cascade should only include the material of beach-building size; finer material will not be deposited in the nearshore but end up further offshore.

Two output examples for the area around the river mouth illustrating the sensitivity of the model to changes in the calibration parameters are shown in Figures 45 and 46. Figure 45 illustrates the output shoreline for different K -values, with a constant sediment supply of $0.009 \text{ m}^3/\text{s}$. A lower value (0.15) results in too little erosion compared to a higher value (0.39), when comparing with the satellite image from 2017. Figure 46 shows how a change in sediment

supply affects the output shoreline, and the K -value is kept constant at 0.25. Note that in Figures 45 and 46, the details inside the river mouth is not described; here only the distributed source is discharging its sediment.

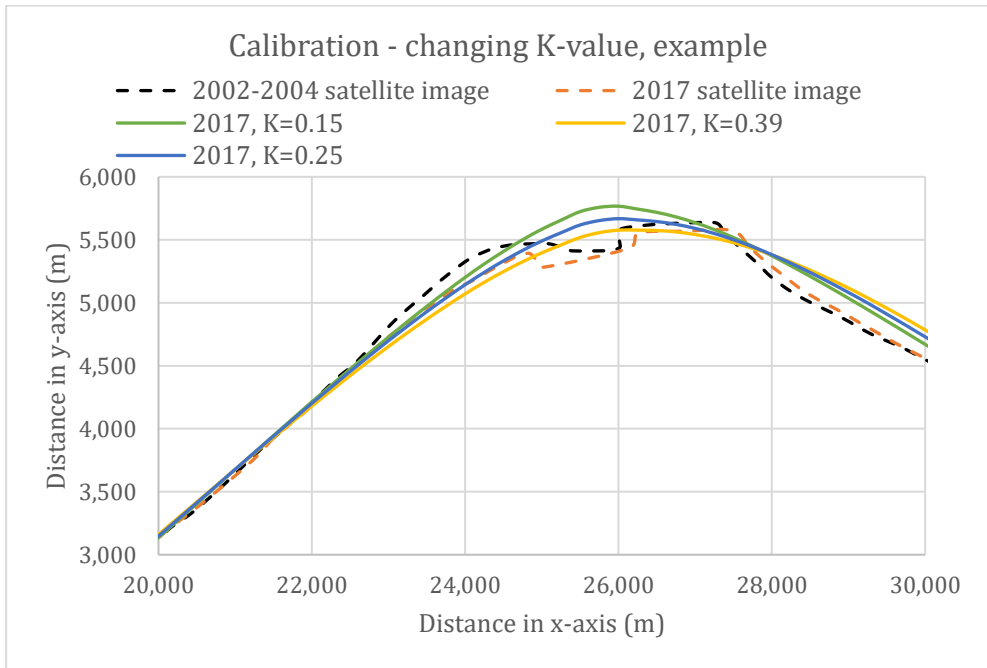


Figure 45. An example of model sensitivity to changes in the K -value and how they affect the output shoreline for the area around the river mouth.

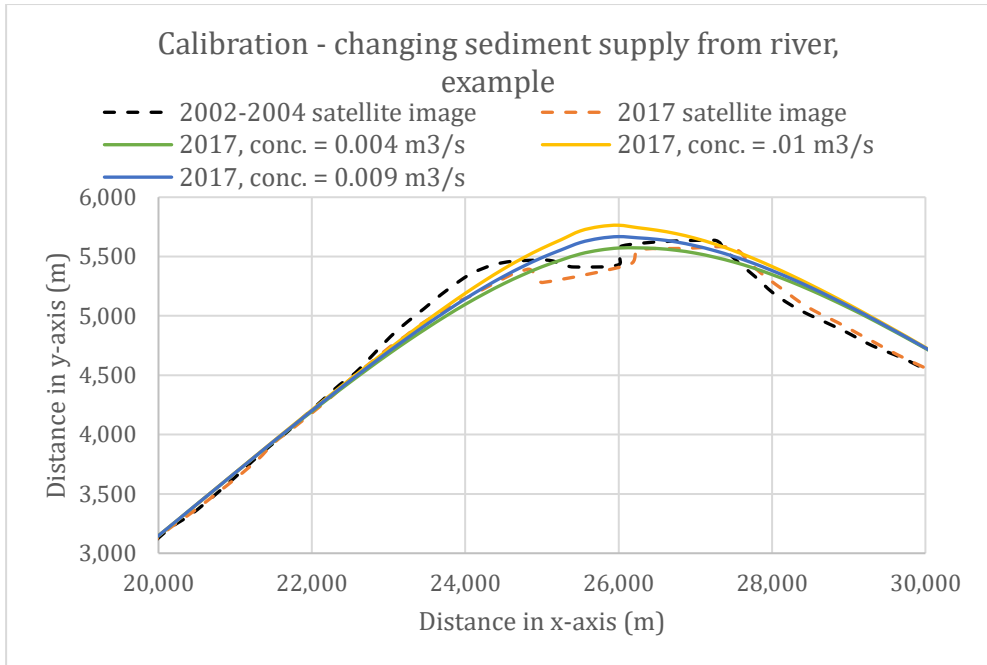


Figure 46. An example of model sensitivity to changes in the sediment supply from the river and how they affect the output shoreline for the area around the river mouth

After the calibration, a validation was performed using the shorelines “2014” and “2017”. The calculated shorelines compared to the measured shorelines are shown for each of the years in Figures 47 and 48. The focus area for the calibration and validation has been around Cua Dai Beach since it is known to be the most problematic area.

Both shorelines used in the validation show good fits between measurements and calculations, exhibiting the same general behaviour (Figure 47 and 48). At Cua Dai Beach the calculated and measured shorelines match well. When studying the behaviour on the northern side of the river mouth, it is seen in Figures 47 and 48 that the beach appears to be slightly wider in the model from 0 to 3 km and 11 to 22 km compared to the information obtained from the satellite images. Between 3 to 11 km the beach in the model is a bit narrower in a similar comparison. On the southern side of the river mouth, similar behaviour is observed in both Figures 47 and 48. From 27 to 36 km the beach is wider in the model, and between 36 to 50 km it is narrower.

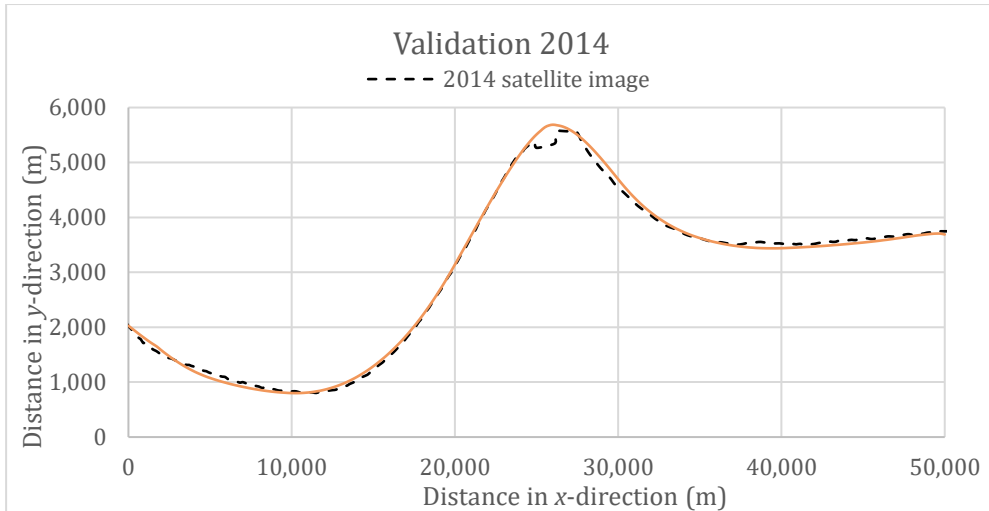


Figure 47. Shoreline from 2014 based on satellite images compared to calculated shoreline with Cascade.

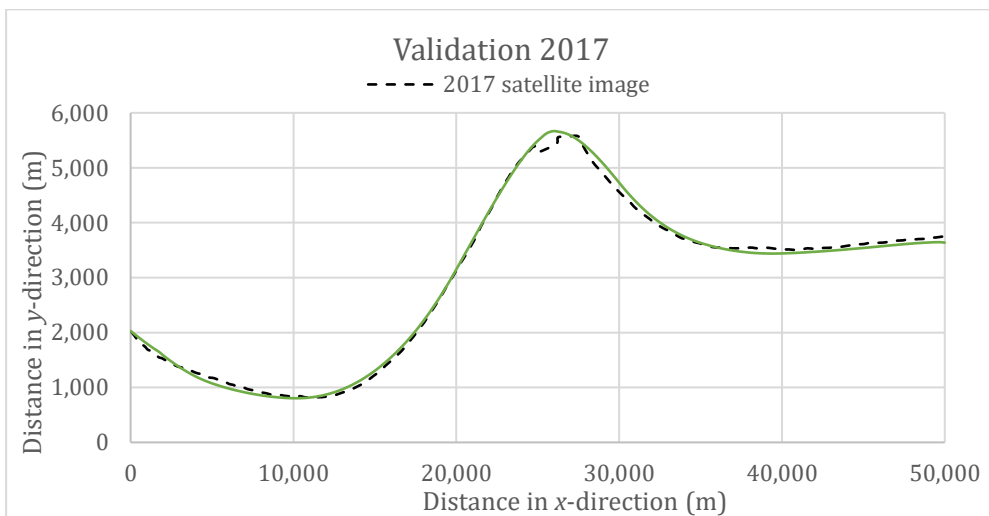


Figure 48. Shoreline from 2017 based on satellite images compared to calculated shoreline with Cascade.

6.3.3 Result and analysis

The result of the annual average net sediment transport direction between the years 2002 to 2017 can be seen in Figure 49. The red lines represent the two boundary conditions, and the yellow lines represent locations for the change in the sediment transport direction. The arrows indicate the direction of the sediment transport. Where two arrows meet there will be accretion, whereas erosion will occur if two arrows are in the opposite directions. The result of

the sediment transport pattern is displayed in Figure 50 showing the shoreline evolution from 2002 to 2017. In Figure 50, the shoreline is divided into three zones that will be discussed in more detail; see also Figures B3 to B5 in Appendix B3.

The first two accretion and erosion areas (around 5000 and 8000 m on the x -axis) do not agree with the observed shoreline data in section 5.6. This could be due to the boundary condition used in the simulation, where a fixed shoreline position is set. Also, the effects of the adjacent headland on the local wave conditions might not have been reproduced accurately enough. The other three erosion and accretion areas (yellow lines in Figure 49) correspond to the evolution of the shorelines observed in section 5.6. A table showing the amount of annual average net sediment movement along the shoreline can be found in Appendix B3. In Appendix B4, a comparison between the Cascade and LST results regarding the annual average net sediment transport is presented.

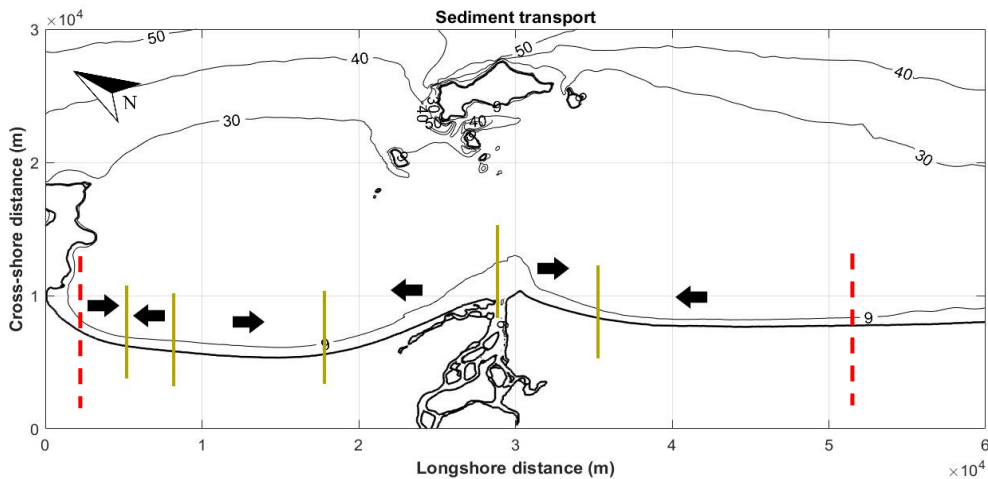


Figure 49. Annual average net sediment transport direction for the years 2002 to 2017.

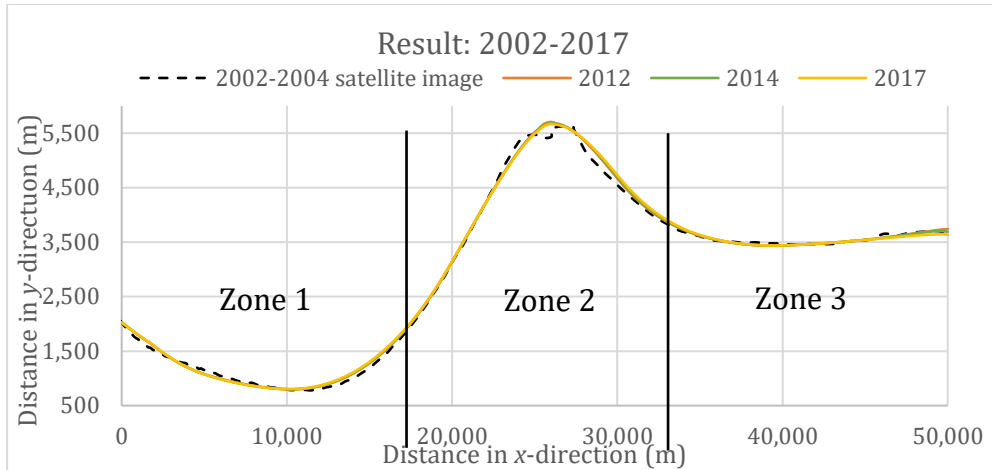


Figure 50. Overview of model simulation result from the initial shoreline “2002-2004”, to the years 2012, 2014 and 2017. The shoreline is divided into Zones 1, 2, and 3, which are shown in more detail in Figures B3, B4, and B5, respectively, in Appendix B3.

The result of the predicted, future shoreline evolution is shown in Figure 51. Figure 51 contains a dotted line illustrating the shoreline from 2017 based on satellite images, a blue line showing the calculated shoreline 2017, and an orange line describing the shoreline after 15 years from 2017 (2033). The two final lines show the shoreline in 2048 (30 years from 2017) based on two different scenarios. Scenario 1 implies that the sediment supply from the river continues at the same magnitude as the calibrated value ($0.009 \text{ m}^3/\text{s}$) until 2048. In scenario 2, the sediment transport in the river discharge is reduced by half after 15 years.

As before, the shoreline has been divided into three different zones, as illustrated in Figure 51. Figures B6 to B8 in Appendix B3 shows more detailed figures of each of the zones. Zone 1 is on the northern side of Thu Bon River mouth and shows the distance 0 to 17 km in Figure 51. Scenarios 1 and 2 show very similar shorelines for year 2048. From 0 to 8 km the beach will retreat around 30 m the first 15 years (2 m per year), and then have a maximum erosion of 6.0 m for the final 15 years (0.40 m per year). After 9 km the model indicates accretion of the beach that continues up to 21 km north, as shown in Zone 2. Between 2017 and 2033 the accretion is around 5.3 m per year, and 2033 to 2048 it is 2.5 m per year.

After 21 km along the x -axis to the north, the beach will be affected by erosion in the coming 30 years (Figure B7 in Appendix B3). The impact of the different scenarios in 2048 will start to show in Zone 2; around the river mouth,

Cua Dai Beach will continue to erode with approximately 4.4 m per year until 2033. If Scenario 1 takes place, the retreat will decrease to around 0.50 m per year compared to Scenario 2, for which the same retreat will occur closest to the river mouth as during the first 15 years.

On the south side of the river mouth, the impact of the different scenarios is almost unchanged. South of the river mouth up to 39 km there is an accretion of 4.7 m per year until 2033, and 3.8 m per the year 2033 to 2048 (Figure B8 in Appendix B3 of Zone 3). The most downdrift part of the modelled shoreline is somewhat similar between the years due to the specified boundary condition. However, the conditions here vary between erosion and accretion depending on the year.

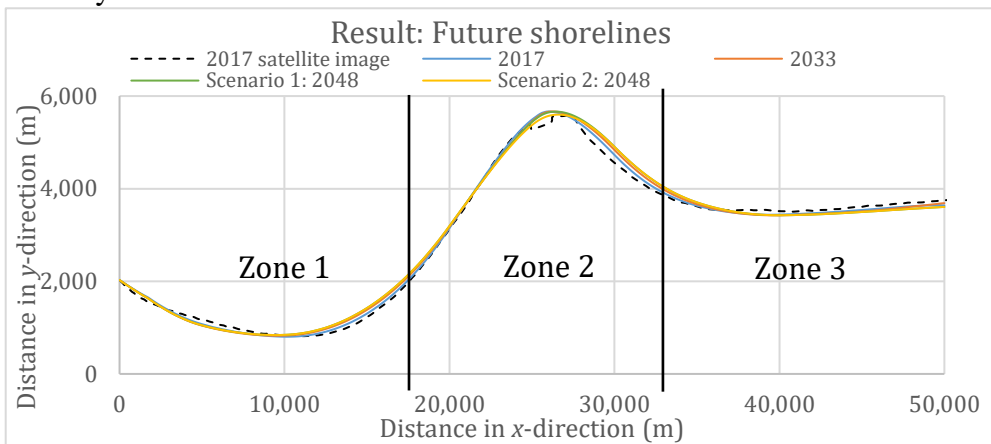


Figure 51. Overview of Cascade results showing shorelines in year 2033 and for two different scenarios 2048, together with the shoreline location in 2017. The shoreline is divided into three different zones, which are presented in more detail in Figures B6 to B8 in Appendix B3

7 Discussion

7.1 Data collection

Regarding the collected data many uncertainties need to be considered. The specific time when the field survey in the area around Cua Dai beach was conducted is of importance when analysing the state of the beach. Due to seasonal variations, the conditions could change drastically. The survey was carried out during the dry season in March 2018. The rainy season (northeast monsoon) occurs in September to January which could result in even more severe erosion due to stormy weather. A comparison with future field surveys could give an indication about seasonal variations and changes in the state of the coastline.

Earlier measured beach profiles of the foreshore and nearshore zone from the years 2014, 2016 and 2017 shows signs of a retreating coastline up to approximately 6.5 km north of the river mouth. This is confirmed by the observations made during the field survey, which indicated erosion up to approximately 7 km. The earlier profiles also imply scouring in front of existing hard protection structures along Cua Dai coastline (P13 to P16 in Appendix A1). There is a risk that the scour may reach the foundation of the structures, undermining them, and causing collapse. The sand supporting the structure from beneath will be dug out and transported away. This is what happened in Figure 15 of a hard-concrete structure taken during the field survey. It can also be one of the reasons for the collapse of Fusion Alya resort (Figure 13), in combination with strong wave forces.

The beach profiles measured in conjunction this study are difficult to compare with earlier profile data or results to yield any specific conclusions. The measurements from the year 2016 are all centred on one area, compared to the ones made during this study. The new profiles give a broader knowledge about the spatial variations along different parts of the coastline. The present profile measurements should be combined with future beach profile measurements at the same locations, in order to provide information about the beach evolution. Future measurements could also be improved by prolonging the survey from the beach further out into the nearshore zone.

All the taken sediment samples taken contain grain sizes only within the range of the definition of sand (0.06 to 2 mm), with a mean median grain size of 0.215 mm. Sample locations B, C, and D all show expected results regarding

the grain size composition along the beach profile according to Jiang et al. (2015) and Hanson (2017). The wave energy distribution and cross-shore transport pattern should result in coarser grains at the shoreline and finer grain upwards the beach profile and seawards. The samples taken at location A deviates from the expected grain size distribution pattern. The sample taken at the coastline (A1) are as projected finer than the sample at the shoreline (A2), but when comparing sample A2 with A3 taken in the nearshore zone, it does not match the predicted theory. Sample A3 has higher median grain size than A2. This deviation could be explained by the fact that the sample was taken in an area of more intensive breaking, where sand bars may have been present. Since the sampling location was limited by the ability of the person taking the sample to reach the bottom sand, this is a possible explanation. Location A is a wide sandy beach with shallow water and sand bars far out in the sea.

Both the bathymetry and the offshore wave climate was obtained from Duong (2018). The bathymetry was compiled from different sources, and the origin of these sources, as well as their data quality, is not known in detail. It is therefore difficult to estimate errors and uncertainties in the bathymetric data. Regarding the bathymetry, the number of measurement points in space and their corresponding times together with the type of data source are important; for example, whether the data came from bathymetric surveys or nautical map should be considered. The interpolation between specific points could neglect detailed bottom variation depending on the accuracy of the measurements. For the calculations of the offshore wave climate, a hindcast approach was used. The transformation from wind to wave parameters are based on various limitations and assumptions defining the model used (SWAN). Also, the input wind conditions over the wave-generating area are not known in detail, but derived from different types of data.

The shorelines were digitized using satellite images obtained from Google Earth. This results in errors since it is difficult to tell the exact location of the shoreline due to wave and tidal motion. Tidal variations were ignored since the exact time of the day when the satellite images were taken were unknown. Some of the shorelines are combinations of images from different months and years, which will also increase the uncertainty. The shoreline position could vary significantly over the seasons due to a dynamic and complex coastal system.

7.2 Numerical modelling

The EBED modelling highlights the importance of reliability in the input data. All the EBED calculations are based on the hindcasted offshore wave climate. Thus, all the errors in the offshore wave data will follow throughout the whole modelling process. It means not only for the EBED result, but also for the LST model and Cascade result, since the output data from the EBED model are used as input in both LST and Cascade.

Thus, the resulting wave climate computed by EBED depends on the input deep-water waves and the bathymetry. Both factors include uncertainties, which will affect the results computed by EBED, as mentioned above. In order to fit the bathymetry to the EBED grid, depth values had to be interpolated. Therefore, some bottom contours or local shallow parts may have been neglected by the interpolation, which will affect the shoaling and the refraction. Since the cell size was 100 x 50 m, there will be more such effects in the interpolation close to shore where bathymetric changes at a higher rate is expected; these effects can be reduced if a smaller cell size is employed. However, a smaller cell size would imply an increase in the simulation time, which is already considerable.

Another limiting factor with regard to execution time is the choice of the modelling area. A more reasonable area would be to include the natural boundary at Tam Hai island at the southeast end of the bay on the southern side of the river mouth. A larger model area was not possible because of too long simulation times, primarily with EBED.

Regarding the EBED calculation procedure, it includes a description of the the most important nearshore wave effects, that is, shoaling, refraction, diffraction, and breaking. All the effects are essential when predicting the wave behaviour around and in the shadow zone of Cham Islands. However, reflection is not considered which could affect the waves, although that would mainly be close to shore where structures are present.

The EBED simulations give the highest waves during winter months, which is a result of the offshore wave climate. The highest offshore waves occur from an east-northeast direction, which is generally from October to January. During the winter months, the Cham Islands are found to reduce the wave height with approximately 50 % in the nearshore area around the river mouth. The influence of the Cham Islands will, therefore, have an impact on the sediment transport during the winter months. It is confirmed when studying

the longshore sediment transport rates obtained with LST. The winter months result in a more dynamic and complex system, which is seen from both the EBED and LST result. When looking at the average wave climate and the average longshore sediment transport similar behaviour is found. It can be concluded that the Cham Islands will markedly influence the wave climate in the nearshore zone for the dominant wave conditions in the area; this must be taken into account when studying the nearshore sediment transport and coastal evolution, as well as measures to alleviate erosion problems.

When the waves approach from an east-southeast direction, the significant wave height is found to be the lowest. Based on the EBED results, this occurs during May to August, also affecting the direction of the transport during the summer as seen in the LST result. The Cham Islands will also reduce the wave height during the summer months, but only in the area just behind the island. The wave energy during the summer months is lower. Hence, there will be less sediment transport during these months. It is confirmed by the LST result indicating a lower net sediment transport during the summer months compared to the rest of the year.

The LST model and Cascade are based on similar theory for the longshore sediment transport, but Cascade allows for more detailed calculations of the transport rate. Both models regard longshore sediment transport and neglect the cross-shore sediment transport, although Cascade can include the latter type of transport through sources and sinks. The cross-shore sediment transport has an influence on the appearance of the coastlines when comparing stormy and calmer weather conditions. Thus, it is important when studying seasonal variations of the beach or the impact of individual events.

Both models only consider sediment transport due to wave-generated currents, and neglect transport from wind- and tide-induced currents. The wave-generated currents are typically dominant in the nearshore, and the impact of the wind and tide will in general be small. The average tidal range at the field site is around 0.7 m, which is defined as micro-tidal conditions. Significant tidal currents may be created around, for example, lagoon shaped river outlets and harbours. The Bon River mouth is as discussed earlier classified as a mix between a lagoon river mouth and L-shape river mouth. When the tidal range is at its highest, tidal currents might be a factor contributing to sediment transport in the vicinity of the river mouth.

Another factor causing the formation of currents are the discharge flow from the river. It is not included in the LST model, so the calculated results only

refer to the transport by wave-generated longshore currents. The reduced sediment supply by the river discharge is believed to be the main reason of the erosion of the adjacent beach. The sediment transport from the river is added in the Cascade model, increasing the usefulness of the modelling. However, the transport rate from Thu Bon River is only an estimated value and it was partly a result of calibration. More investigations are needed to confirm the reliability of the input value.

The Cascade results show that the sediment supply from the river plays an important role regarding the erosion at Cua Dai Beach. If the sediment transport is reduced from the estimated input at present, the erosion will further increase. Possible reasons for a reduced sediment supply from the river are increased sand mining activity and the construction of hydropower plants.

In the LST model, the relative density of sand is the only sediment characteristics included depending on the CERC formula. Thus, no detailed and accurate description of the grain-size composition of sand can be modelled. However, in many cases the sand composition is a significant factor when studying sediment movement and the accuracy of the LST model could be improved by including the median grain size in the model. The description of the sediment characteristics through the median grain size is an improvement added in the Cascade model, although for the present application a CERC-type variation of the transport formula was used.

LST model only calculates sediment transport at a specific point, whereas Cascade provides a higher resolution that more closely follows the sediment movement along the entire studied coastline. The LST model gives a good indication of the sediment net transport and its direction, but the spatial resolution is coarse and there is no coupling to the shoreline evolution. It shows which locations that are probably close to net sediment transport equilibrium, which are found around 7 km south of the river mouth, continuing in the southeast direction. This is not the case for Cascade result, which indicates a northwest transport direction along the major part of the southern coastline, only the first 5 km after the river mouth is there a southeast transport direction.

A comparison between the amount of annual average net sediment transport for the two different models (LST and Cascade) is presented in Appendix B4. The results show quite similar transport direction until location L8, after which Cascade implies a significant northwest transport direction in L8, L9, L10, and L11. Moreover, the amount of annual average sediment transport is significantly higher at these four points in the Cascade result. The average

wave climate indicates an incoming wave angle which should result in a northwest transport direction on the southern side, which agree with the Cascade result.

A factor that is neglected in the Cascade model is the influence of the structures for erosion protection. On the northern side of the river mouth, hard structures exist along a stretch of about 3 km. In the model, this is an area that will continue to be affected by erosion during all the modelled years until 2048. Cascade regards the whole coastlines as a sandy beach. It means that the sand that is predicted to erode in the area with the hard structures needs to be taken elsewhere. The longshore sediment transport in the affected area is found to be in the northeast direction. Hence, the erosion would probably occur at the beaches further north, starting at the downdrift end of the protection.

As mentioned previously, hard erosion protection is common on the northern side of river mouth. Sandbags and geotubes are a commonly used intermediate protection on what is left of Cua Dai Beach. Neither of the solutions are sustainable alternatives, if the goal is to preserve and prevent the nearby beaches further north to erode. The beaches play an important role for the tourism and therefore livelihood of the local people.

The behaviour of hard structures and other erosion protection, and how they affect the system, needs to be studied in more detail on a local level. The different types of protection interact with each other, which is often an important factor to study in order to find an optimal solution. Before further constructions are made, it is necessary to identify the reason for erosion and quantify it. The field area is a complex and dynamic coastal system with significant seasonal variations, which needs to be considered when finding a solution to the erosion problems.

8 Conclusion

The studied area is a dynamic and complex coastal system. The influence of the Cham Islands is a significant factor regarding the wave behaviour and longshore sediment transport. It is essential to have knowledge about sediment transport magnitudes and directions to predict the impact of erosion. The modelling of the future long-term shoreline evolution demonstrates that the most problematic areas will continue to be influenced by erosion until 2048 and probably beyond. The erosion is found to propagate along the shoreline in the northeast direction north of the river mouth, which will affect the remaining beaches nearby Hoi An Town. The sediment supply from Thu Bon River also plays an important role regarding the magnitude of erosion in the vicinity of the river mouth. At the present level of sediment supply erosion will continue, although most likely at a lower rate; however, further reduction in the supply will increase the erosion.

Future recommended studies are local modelling of the sediment transport behaviour around Thu Bon River mouth. It will give a better understanding of the complexity of the system in the areas with the most severe erosion, allowing for a higher spatial and temporal resolution than what the present modelling with Cascade yielded. The choice of the local model should be such that it allows for more details of, for example, structures and river flow conditions, to be considered. As in any coastal area affected by erosion, the causes need to be identified before effective and sustainable solutions can be found.

Since preserving and restoring the beaches are important for the tourism industry in the area, a socio-economic study should be useful. A cost-benefit analysis put the investments for protecting the beaches in relation to losing the income from the tourism.

References

- Asian Development Bank, 2016. *Viet Nam - Energy sector assesment, strategy, and road map*, Mandaluyong City, Philippines: Asian Development Bank.
- Atilla, B., Magnus, L. & Hans, H., 2007. A new formula for the total longshore sediment transport rate. *Coastal Engineering*, Volume 54, p. 700–710.
- Bird, E. & Lewis, N., 2015. *Beach Renourishment*. s.l.:Springer International Publishing.
- Delegation of the European Union to Vietnam, 2018. *Coastal erosion in Viet Nam: the European Union facilitates research and discussion on causes and protection measures in the perspective of climate change*. [Online] Available at: https://eeas.europa.eu/delegations/vietnam/38788/coastal-erosion-viet-nam-european-union-facilitates-research-and-discussion-causes-and_en [Accessed 14 02 2018].
- Do, A. T., de Vries, S. & Stive, M. J., 2018. Beach Evolution Adjacent to a Seasonally Varying Tidal Inlet in Central Vietnam. *Journal of Coastal Research*, 1(34), pp. 6-25.
- Duong, C. D., Nguyen, N. T., Nguyen, T. V. & Tran, T. T., 2017. *Research On the Seasonal Trend of Shorline and Coastal Changes for Cua Dai, Hoi An Using Sbeach Model*, Hoi An, Vietnam: s.n.
- Duong, D., 2018. *Calculations of offshore wave climate and bathymetry*. Hanoi, Vietnam: s.n.
- Duy, D. et al., 2016. Study on river mouth delta formation and recent beach erosion on Cua Dai Beach, Vietnam. *Journal of Japan Society of Civil Engineers*, Volume Vol. 72(2), pp. I_1657-I_1662.
- Fila, J. et al., 2016. *Costal erostion Hoi An*, Delft: Delft Univerity of Technology.
- Google Inc, 2018. *Google Earth*. [Online].
- Grafals-Soto, R. & Nordstrom, K., 2009. *Sand Fences in the Coastal Zone: Intended and Unintended*, s.l.: Springer Science + Business Media.

Gyr, A. & Hoyer, K., 2006. *Sediment transport: A geophysical phenomenon*, Dordrecht, The Netherlands: Springer.

Hallermeier, R., 1980. A profile zonation for seasonal sand beaches from wave climate. *Coastal Engineering*, Volume 4, pp. 253-277.

Hanson, H., 2017a. *Introduction to coastal sediment transport processes*. Lund, Lunds Universitet.

Hanson, H., 2017b. *Basic concepts in coastal protection*. Lund, Lund University.

Hoang, V. C., Viet, N. T. & Tanaka, H., 2015. Morphological change on Cua Dai Beach, Vietnam: Part II theoretical analysis. *Tohoku Journal of Natural Disaster Science*, pp. Vol.51, p. 87-92.

Hung, N. T., Vinh, B. T., Nam, S. Y. & Lee, J. L., 2017. Cause Analysis of Erosion-Induced Resort Washout on Cua Dai Beach, Vietnam.. *Journal of Coastal Research*, Volume 79, pp. 214-218.

Imran, A., Nakashima, K. & Kawasaki, S., 2017. Combination Technology of Geotextile Tube and Artificial Beachrock for Coastal Protection. *International Journal of GEOMATE*, 13(39), pp. 67-72.

Jianga, C. et al., 2015. Sorting and sedimentology character of sandy beach under wave action. *Procedia Engineering*, Volume 116, pp. 771-777.

Komar, P. & Inman, D., 1970. Longshore sand transport on beaches. *Journal of Geophysical Research*, Volume 75, pp. 5914-5927.

Kondolf, G. et al., 2014. Sustainable sediment management in reservoirs and regulated rivers: Experiences from five continents.. *Earth's Future*, 2(5), pp. 256-280.

Lam, N., 2009. *Hydrodynamics and Morphodynamics of a Seasonally Forced Tidal Inlet System*, s.l.: Ph.D. Thesis, Delft University of Technology.

Landguiden, 2016. *Klimat*. [Online]

Available at: <https://www.ui.se/landguiden/lander-och-omraden/asien/vietnam/klimat/>

[Accessed 07 03 2018].

- Larson, M., Kraus, N. C. & Hanson, H., 2002. Simulation of regional longshore sediment transport and coastal evolution - the "Cascade" model. *Coastal Engineering Conference, World Scientific Press, Issue 28.*
- Larson, M., Kraus, N. C. & Hanson, H., 2002. SIMULATION OF REGIONAL LONGSHORE SEDIMENT TRANSPORT AND COASTAL EVOLUTION – THE “CASCADE” MODEL. *Coastal Engineering Conference, World Scientific Press, Issue 28.*
- LUCCI, 2010. *Lưu vực sông Vu Gia – Thu Bồn*. [Online]
Available at: <http://www.lucci-vietnam.info/vn/khu-v-c-nghien-c-u/di-u-ki-n-t-nhien>
[Accessed 10 02 2018].
- Mase, H., 2001. Multi-directional random wave transformation model based on energy balance equation. *Coastal Engineering Journal*, 43(4), pp. 317-227.
- Nam, P. T., Larson, M., Hanson, H. & Hoan, L. X., 2009. A numerical model of nearshore waves, currents, and sediment transport. *Coastal Engineering*, Volume 56, pp. 1084-1096.
- Nam, P. T., Larson, M., Hanson, H. & Oumeracic, H., 2017. Model of nearshore random wave transformation: validation against. *Ocean Engineering*, Volume 135, pp. 183-193.
- Nationalencyklopedin, n.d. *Vietnam*. [Online]
Available at: <http://www.ne.se/uppslagsverk/encyklopedi/lång/vietnam>
[Accessed 24 04 2018].
- Nauditt, A. & Ribbe, L., 2017. *Land Use and Climate Change Interaction in Central Vietnam - LUCCI*. Singapore: Springer Nature.
- NOAA, N. O. a. A. A., 2017a. *National Ocean Service, What is an estuary?*. [Online]
Available at: <https://oceanservice.noaa.gov/facts/estuary.html>
[Accessed 19 01 2018].
- NOAA, N. O. a. A. A., 2017b. *NOAA Ocean Service Education*. [Online]
Available at:
https://oceanservice.noaa.gov/education/kits/tides/media/supp_tide07a.html
[Accessed 19 01 2018].

- Rijn, L. v., 2011. Coastal erosion and control. *Ocean & Coastal Management*, pp. vol.54. iss.12. p. 867-887.
- Schoonees, J. & Theron, A., 1996. Improvement of the Most Accurate Longshore Transport Formula. *25th International Conference on Coastal Engineering*, Volume 3, pp. 3652-3665.
- Schoones, J. & Theron, A., 1993. Review of the field-data base for longshore sediment transport. *Coastal Engineering*, Volume 19, pp. 1-25.
- Soulsby, R., 1997. *Dynamics of marine sand*. s.l.:Thomas Telford.
- Tanaka, H., Hoang, V. & Viet, N., n.d. *Investigation of morphological change at the cua dai river mouth*. s.l., International Coastal Engineering Conference, American Society of Civil Engineers.
- Tide-forecast, 2018. *Tide-forecast, Tide Times for Hoi An*. [Online] Available at: <https://www.tide-forecast.com/locations/Hoi-An/tides/latest> [Accessed 19 01 2018].
- Tuan, B. D. T. & Viet, N. T., 2016. *Erosional situation at Cua Dai Beach, Hoi An (The North Part)*. s.l., CKT.
- Tung, T., 2011. *Morphodynamics of Seasonal Closed Coastal Inlets at the Central Coast of Vietnam*, s.l.: Ph.D. Thesis, Delft University of Technology.
- UNESCO, W. H. C., 2018. *UNESCO World Heritage Centre*. [Online] Available at: <http://whc.unesco.org/en/list/948> [Accessed 01 02 2018].
- US Army Corps of Engineers, 1984. *Shore Protection Manual*,. Washington D.C.: US Army Corps of Engineers, Coastal Engineering Research Center.
- Viet, N. T., 2016. *Report No2 - Report on field investigation in October 2016*, Hoi An: CKT & Ministry of agriculture and rural development.
- Viet, N. T., Hoang, V. C., Hai, H. D. & Duy, D. V., 2015c. Analysis on Erosion of Beach Adjacent to Cua Dai River Mouth. *5th International Conference on Estuaries and Coasts*, pp. 153-158.
- Viet, N. T., Hoang, V. C. & Tanaka, H., 2015a. Morphological change on Cua Dai Beach, Vietnam: Part I image analysis. *Tohoku Journal of Natural Disaster Science*, Volume 51, pp. 81-86.

Viet, N. T., Hoang, V. C. & Tanaka, H., 2015b. Morphological change on Cua Dai Beach, Vietnam: Part II theoretical analysis. *Tohoku Journal of Natural Disaster Science*, Volume 51, pp. 87-92.

Appendix A: Data collection

A1. Beach profiles

A total of 31 profiles exist for the area around Thu Bon River mouth. Profile P1 to P23 were measured on the foreshore and in the nearshore zone, where P1 to P18 is on the northern side of the river mouth (Figure A1 to A18) and P19 to P23 on the southern side (figure A19 to A23). Figure A24 illustrates P24 which is taken across the river mouth. P25 to P31 are measured across the beach and a part of the nearshore zone (figure A25 to A31). (Duong, et al., 2017)

Profile P1 to P18 (Figure A1 to A18) are from north of river mouth. P1 to P6, P16, and P18 are measured during an unknown month in 2014, and in March and October 2016. P7 to P15 and P17 have additional measurements from March 2017. P1 and P2 are profiles located most to the north, around 7.5 km from the river mouth. Between 2014 and 2016 no change in the beach slope is observed (Figure A1 and A2) and the slope is estimated to be around 1:110. P3 to P9 (Figure A3 to A9), 4 to 6.5 km from the river mouth, indicate a retreat of the coastline between 2014 and 2016, but keeping a similar slope. The slope for profile P3 to P6 is approximately 1:130. The retreat is then stabilized between 2016 and 2017 for the profiles P7 and P9 (Figure A7 and A9).

The profiles P10 to P12 show a stable coastline from 2014 to 2017 (Figure A10 to A12). The slope for P7 to P12 is steeper over the first 500 m and then becomes smoother further offshore. P12 to P14, P17, and P18 are measured adjacent to five different resorts that are protected by rubble revetments. P15 and P16 are in front of concrete revetments. This is shown in figure A15 to A16, indicated by a steep slope around 1:50 closer to the shoreline. P13 to P16 shows a greater slope from 2014 to 2017 indicating a scour effect due to the hard erosion protection (Figure A13 to A16).

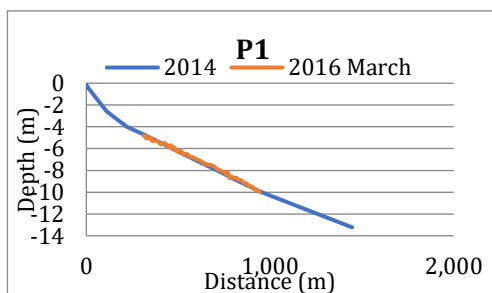


Figure A1. Profile P1.

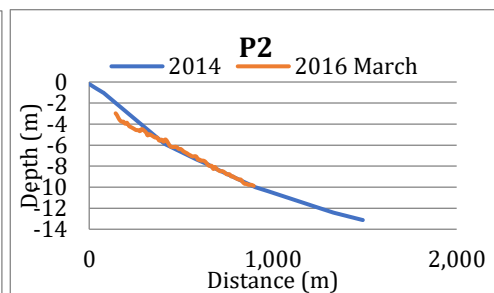


Figure A2. Profile P2.

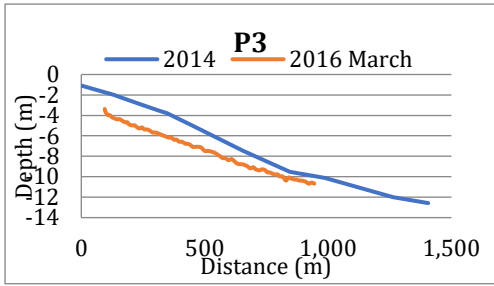


Figure A3. Profile P3.

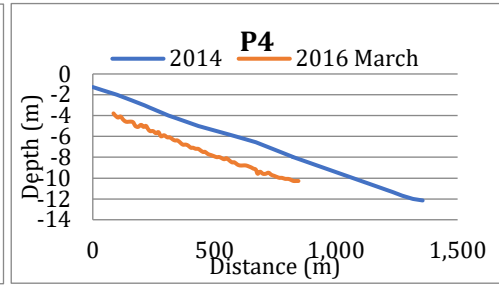


Figure A4. Profile P4.

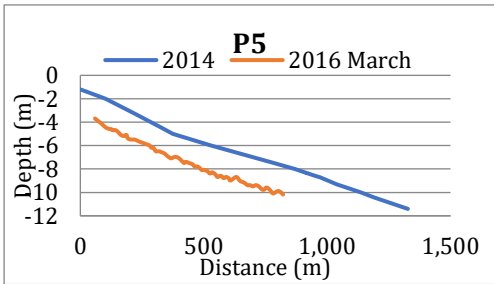


Figure A5. Profile P5.

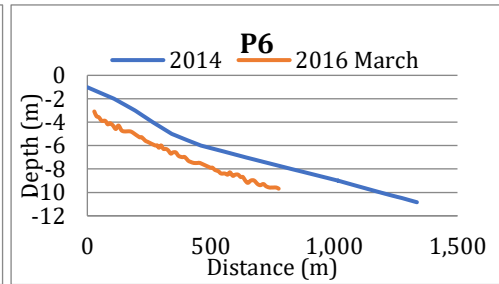


Figure A6. Profile P6.

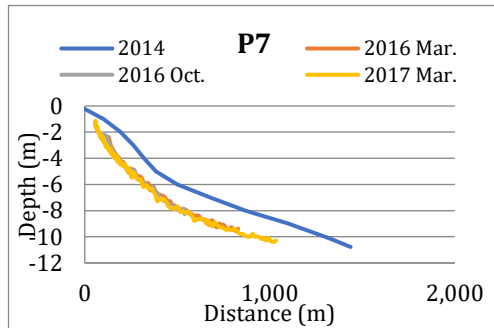


Figure A7. Profile P7.

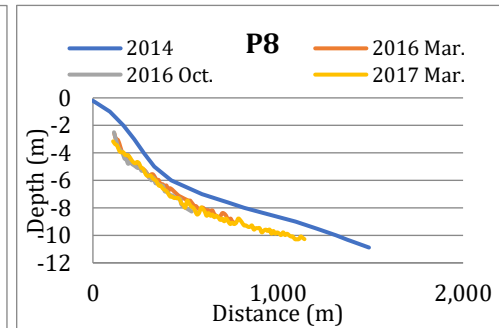


Figure A8. Profile P8.

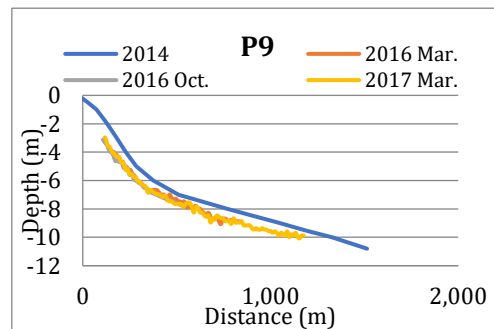


Figure A9. Profile P9.

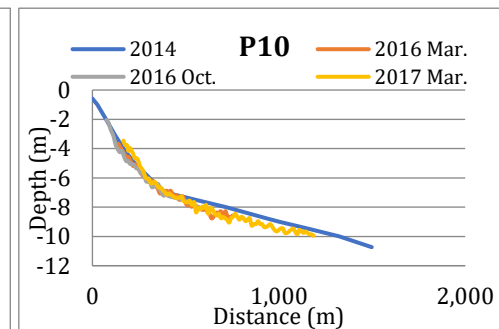


Figure A10. Profile P10.

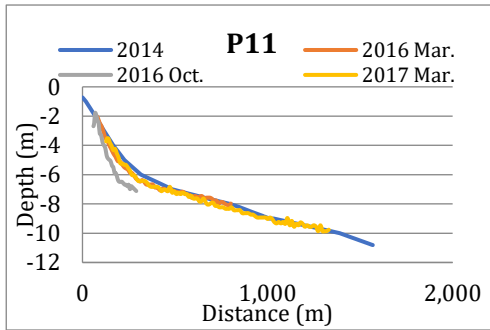


Figure A11. Profile P11.

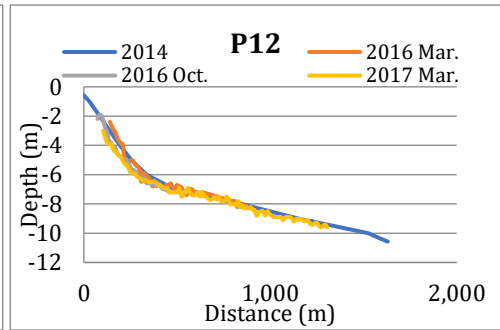


Figure A12. Profile P12.

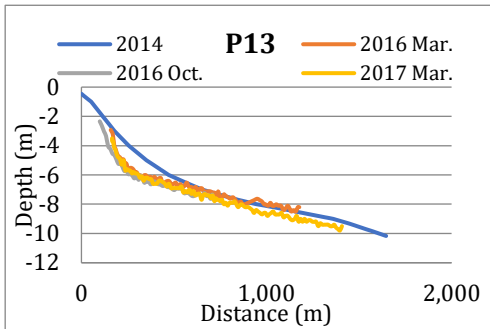


Figure A13. Profile P13.

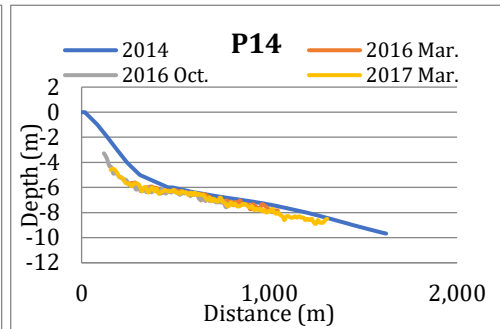


Figure A14. Profile P14.

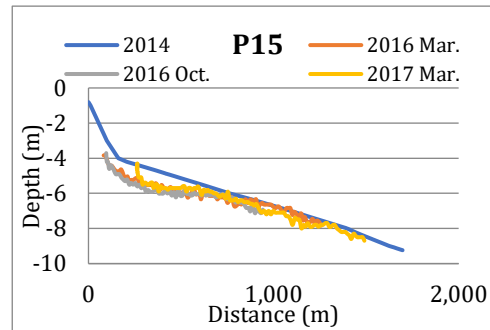


Figure A15. Profile P15.

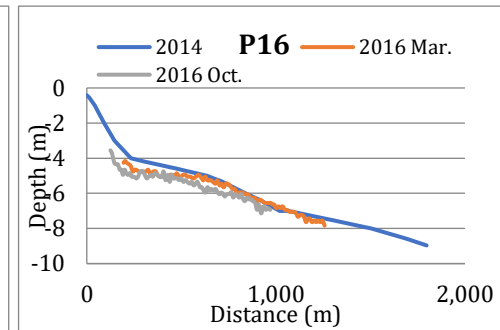


Figure A16. Profile P16.

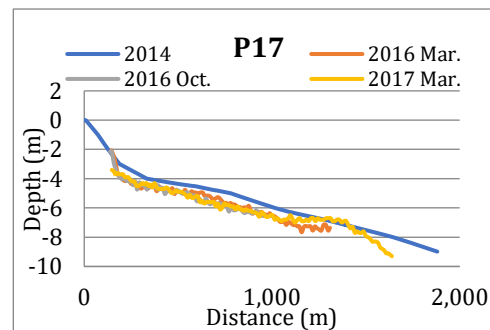


Figure A17. Profile P17.

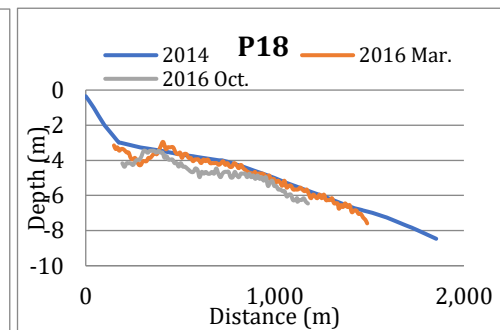


Figure A18. Profile P18.

Profiles P19 to P23 are measured south of the river mouth. P19 (figure A19) is situated closest to the river mouth and indicates a changing shape of the profile in the nearshore zone from the year 2014 to 2016. Figures A20 to A23 shows P20 to P23, respectively; all profiles have similar average slopes of about 1:115 from 2014 to 2016. The surveyed length of the profiles in March 2016 are only 400 to 300 m compared to approximately 1200 m for 2014. P21 to P23, Figures A21 to A23, respectively, indicate a retreating shoreline. In Figure A24 the profile of the river mouth, P24, is shown, illustrating a changing shape of the bottom between 2014 and 2016.

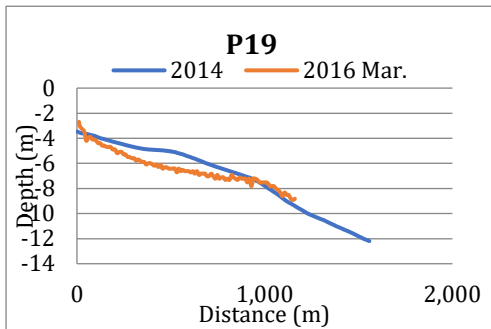


Figure A19. Profile P19.

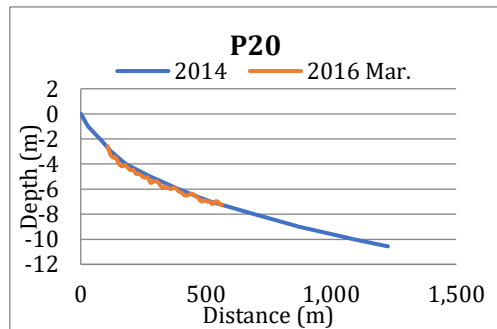


Figure A20. Profile P20.

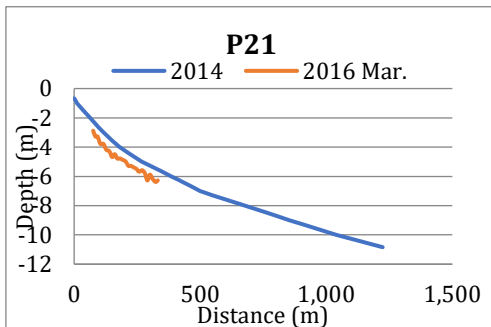


Figure A21. Profile P21.

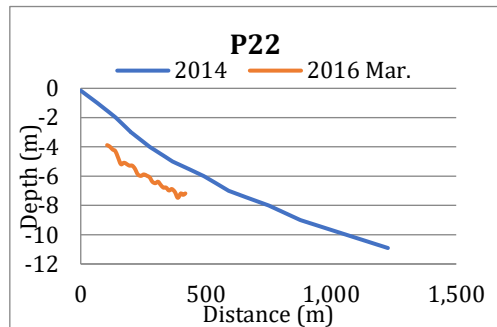


Figure A22. Profile P22.

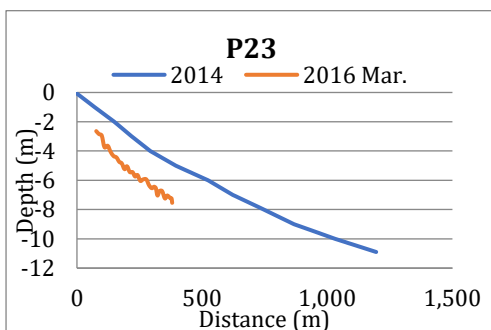


Figure A23. Profile P23.

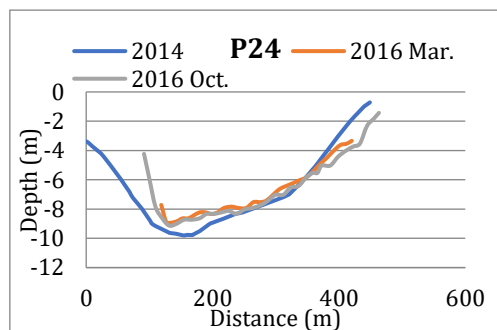


Figure A24. Profile P24.

P25 to P31 show the profile over the beach and a part of the nearshore zone (Figure A25 to A31). The beach profiles P25 to P27 are measured around 4.2 km on the north side of the river mouth during a storm event in October 2016 with two or three days in between each survey. The last measurements were taken nine days after the first for P26 and P27 and shows the development of a steeper and more massive berm on the beach (Figures A26 and A27). Profile P25 (Figure A25), close to P8, was measured on the foreshore and over the nearshore zone. P26 and P27 are both in the vicinity of P9. The profiles over the foreshore and nearshore zone can be seen as an extension of the profiles across the beach and a part of the nearshore zone.

The most recent profiles are P28 to P31 from March 2018 done in conjunction with this study (Figures A28 and A31). P28 is in between P1 and P2, P29 close to P11, and P31 near P21. P28 is located 7.5 km north of the river mouth, P29 around 3.2 km from the mouth, P30 next to it, and P31 approximately 2 km south of the river mouth. P30 reaches out into the recently created opening of the river mouth. P24 illustrates a cross section of the bottom in the river outflow.

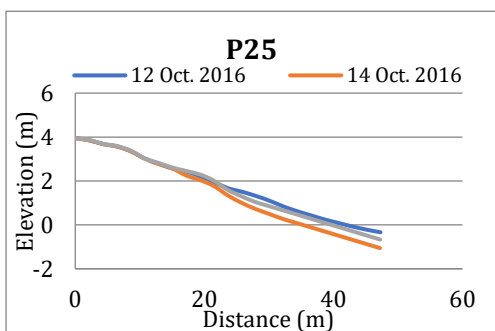


Figure A25. Profile P25.

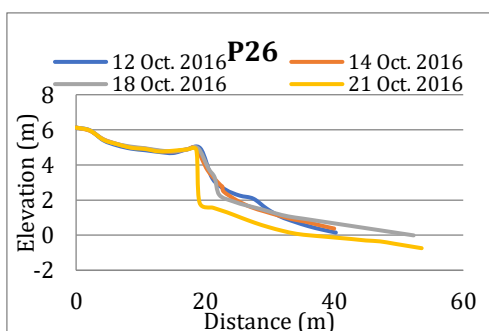


Figure A26. Profile P26.

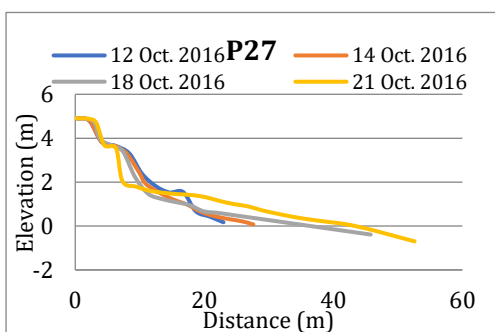


Figure A27. Profile P27.

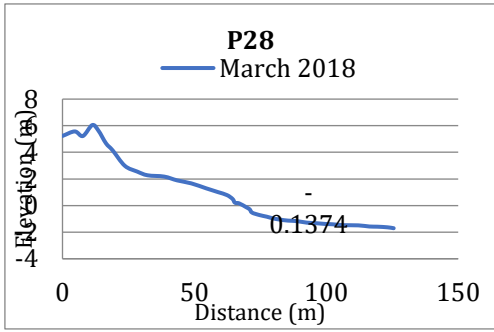


Figure A28. Profile P28.

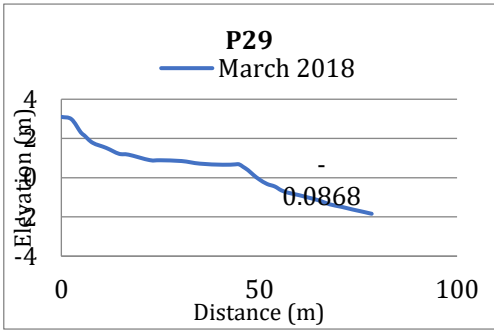


Figure A29. Profile P29.

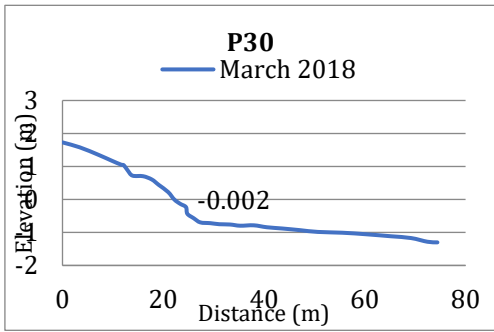


Figure A30. Profile P30.

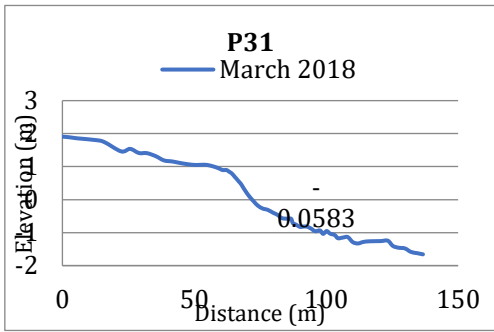


Figure A31. Profile P31.

A2. Sediment analysis

At each site, A, B, C and D, three samples were collected. The sampling points were distributed along the beach profile according to Figure 24 in section 5.3. Below, the grain-size distribution curves (Figures A32 to A35) are presented, followed by Table A1 containing the median grain size, $D50$, for each of the samples. The average $D50$ is 0.215 mm for all samples.

Table A1. Median grain size for each of the sample and an average median grain

Sample	D50 (mm)
A1	0.157
A2	0.178
A3	0.208
B1	0.239
B2	0.254
B3	0.209
C1	0.232
C2	0.240
C3	0.168
D1	0.254
D2	0.255
D3	0.183
Mean	0.215

Site A was at the time of the sample collection an approximately 70 m wide beach enclosed by the vegetation line and shallow water. The samples in the surf zone were collected at an estimated depth of around 1.5 m, about 50 m from the shoreline at moderate wave conditions. Figure A32 shows the grain-size distribution curves for the three different samples taken at location A. When looking at Figure A32, sample A1 located at the border to the beach is the finest one with a $D50$ value of 0.157 mm. This is followed by A2 with a $D50$ of 0.178 mm. The sample with the largest grain size is the one taken in the surf zone were $D50$ is 0.208 mm.

Site B is in the part of Cua Dai that is located closest to the river mouth. The beach width was around 15 m, and the sample location in the surf zone approximately 20 m seawards at a depth of 1 m. The wave conditions were moderate, but strong currents limited the depth of the sampling. The sample taken in the surf zone (B3) is found to be the finest, followed by the coastline

sample (B1), and finally the shoreline sample (B2). This is illustrated in Figure A33. For B3 D_{50} is 0.209 mm, B1 0.239 mm, and for B2 0.254 mm.

Site C is close to the most northern part of Cua Dai Beach. At this site, the beach is limited by sand bags protecting the coastline against the ongoing erosion. Behind the sandbags, there is about 20 m of vegetation followed by a road. The area behind the sandbags is a non-natural environment where much digging due to the erosion and construction of the road had been taken place. Therefore, the C1 sample was taken just below the sandbags on the beach. The width of the beach in front of the erosion protection was only about 5 m. Thus, samples C1 and C2 were taken relatively close to each other. Figure A34 illustrates the grain-size distribution curve for location C, where it is shown that the samples C1 and C2 are the coarser samples with similar D_{50} values, 0.232 mm and 0.240 mm, respectively. Sample C3 was collected at an estimated water depth of 1.5 m around 20 m from the shoreline, and is the finest of the samples with a D_{50} of 0.168 mm. The wave conditions were rough, which complicated the collection.

Site D is an approximately 30-m wide sandy beach backed by a vegetation line. The rough wave conditions limited the sediment sampling at D3, which was collected in the surf zone. It was taken at an estimated depth of 1 m, about 10 m out in the sea. When looking at the grain-size distribution curve for site D (Figure A35), it is shown that the finest sample is D3, located in the surf zone (D_{50} is 0.183 mm). D1 and D2 have similar D_{50} values of 0.254 mm and 0.255 mm, respectively, but the D2 sample has a poorly graded distribution compare to sample D1, which was more uniform. A steeper curve illustrates a well graded sample in the grain-size distribution diagram.

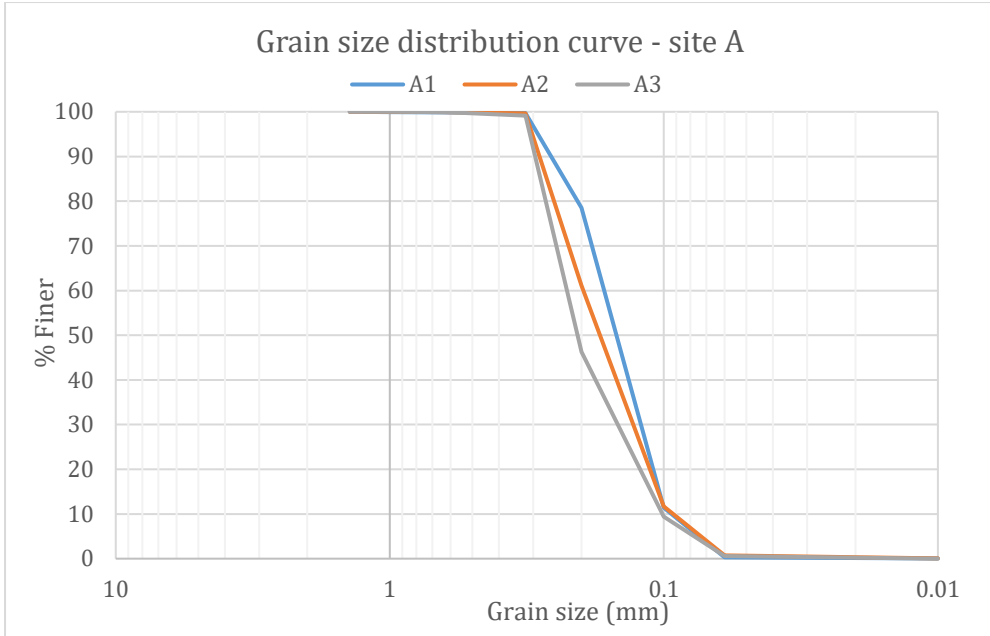


Figure A32. Grain-size distribution curve for location A. Sample A1 is illustrated with a blue line, A2 in orange, and A3 in grey.

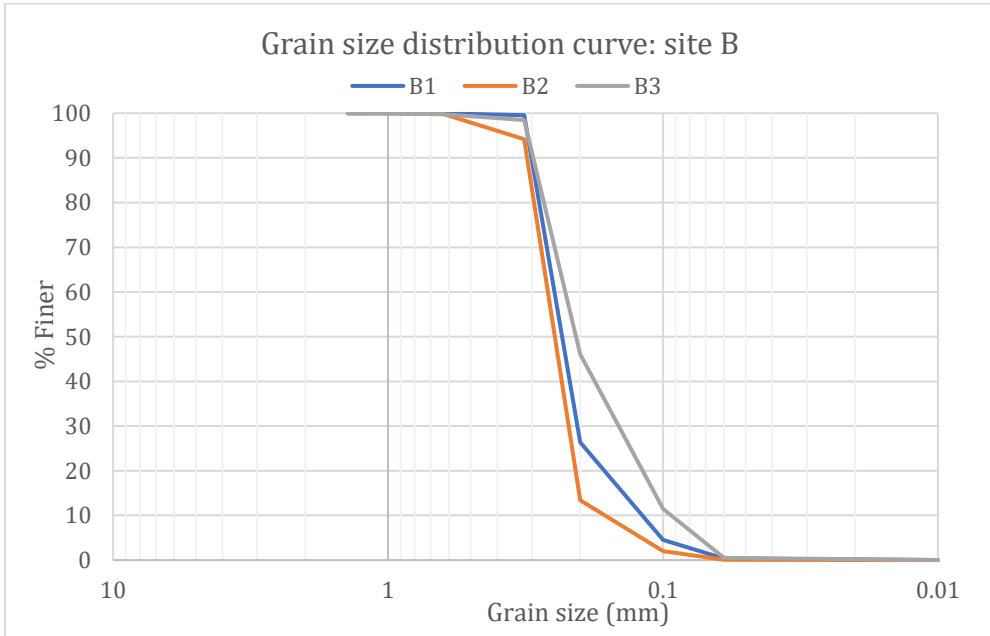


Figure A33. Grain-size distribution curve for location B. Sample B1 is illustrated with a blue line, B2 in orange, and B3 in grey.

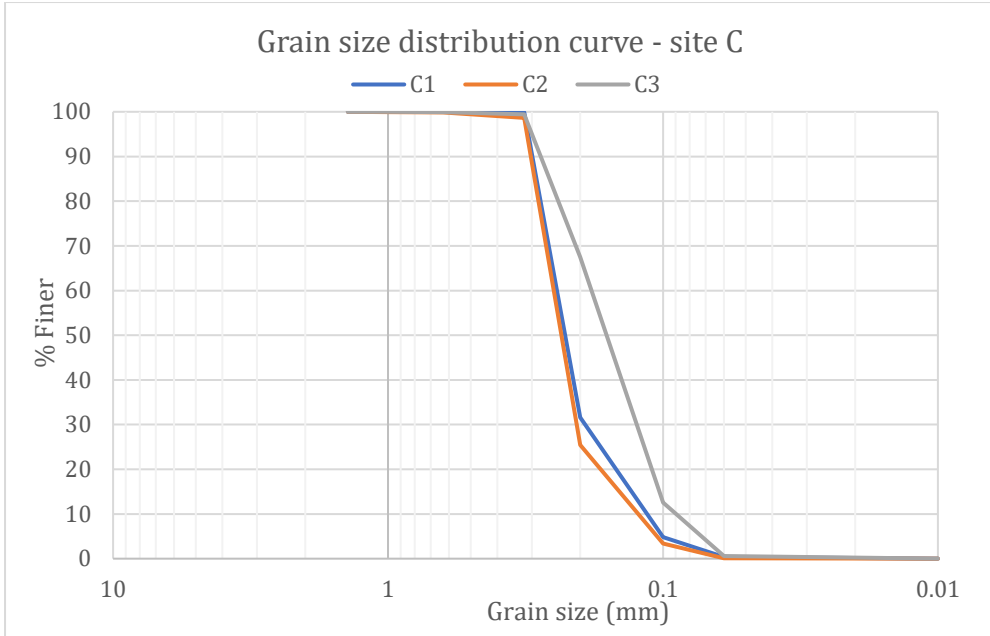


Figure A34. Grain-size distribution curve for location C. Sample C1 is illustrated with a blue line, C2 in orange, and C3 in grey.

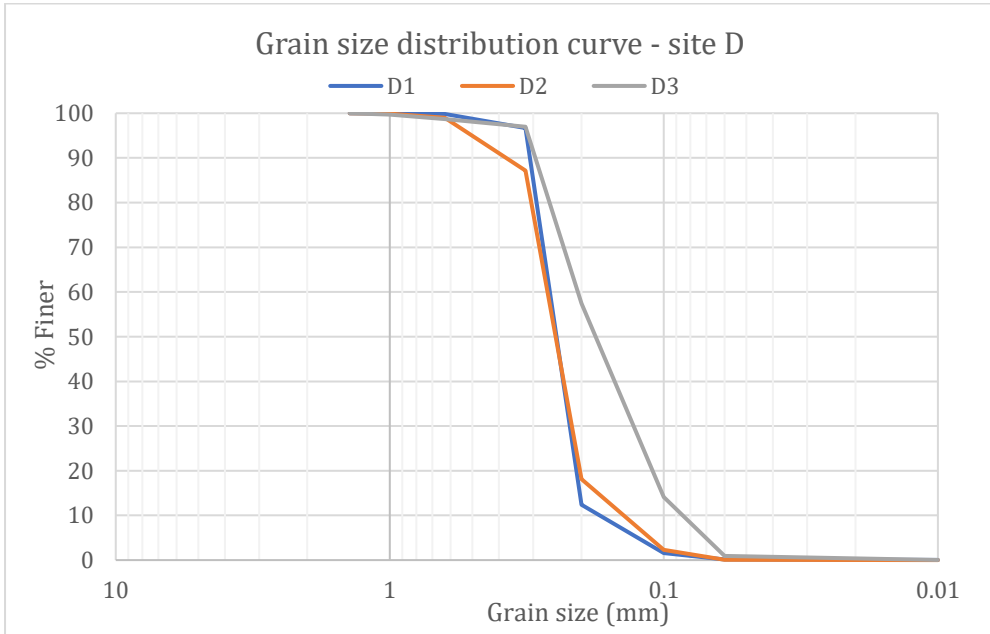


Figure A35. Grain-size distribution curve for location D. Sample D1 is illustrated with a blue line, D2 in orange, and D3 in grey.

A3. Offshore wave climate data

The offshore wave data encompassed the years 1988 to 2017, with wave conditions given every third hour between 1988 to 2004, and every hour between 2005 to 2017, implying that the data included a total of 163,632 individual waves. Table A2 shows the monthly mean of the average significant wave height, maximum wave height, and average period for every month for the years 1988 to 2017. Table A3 shows the significant wave height that is exceeded twelve hours per year and the corresponding period, which is used to calculate the depth of closure according to Hallermeier's equation (Equation 6, section 2.2.5).

Table A2. Monthly mean of average significant wave height, maximum significant wave height, and the average period

Month	Average H_s (m)	Max H_s (m)	Average T_s (s)
Jan	1.60	4.23	7.54
Feb	1.32	3.76	7.00
Mar	1.15	3.78	6.42
Apr	0.91	3.26	5.78
May	0.73	3.38	5.37
Jun	0.63	3.30	5.06
Jul	0.60	2.82	5.10
Aug	0.56	2.88	5.36
Sep	0.75	7.24	5.80
Oct	1.33	8.67	7.14
Nov	1.77	9.33	7.75
Dec	1.98	5.19	8.22

Year	He (m)	T_s (s)
1988	3.68	14.71
1989	2.97	15.87
1990	4.34	16.39
1991	2.81	16.39
1992	2.81	16.39
1993	3.60	16.67
1994	3.58	15.38
1995	3.44	12.20
1996	3.34	14.71
1997	2.98	17.54
1998	3.62	12.35
1999	3.25	12.20
2000	3.07	11.49
2001	3.13	12.99
2002	2.85	15.15
2003	2.99	12.20
2004	2.70	14.49
2005	5.02	11.76
2006	4.18	12.71
2007	4.60	11.76
2008	4.69	11.76
2009	6.47	11.76
2010	4.33	16.01
2011	4.46	14.82
2012	4.66	12.71
2013	8.08	16.01
2014	4.93	13.72
2015	4.05	11.76
2016	4.89	14.82
2017	5.12	11.76
Average	4.03	14.00

Table A3. Yearly significant wave height that is exceeded twelve hours per year H_e , and corresponding T_s .

A4. Shorelines

Figure A36, A37, and A38, show each of the investigated zones in section 5.6 (Figure 30) in more detail. The figures show the shorelines for the years “2002-2004”, “2011-2012”, “2014”, and “2017”. In Figure A36, north of the river mouth, accretion can be seen between the years. Figure A37 indicates erosion around the river mouth. Figure A38 shows slight accretion south of the mouth.

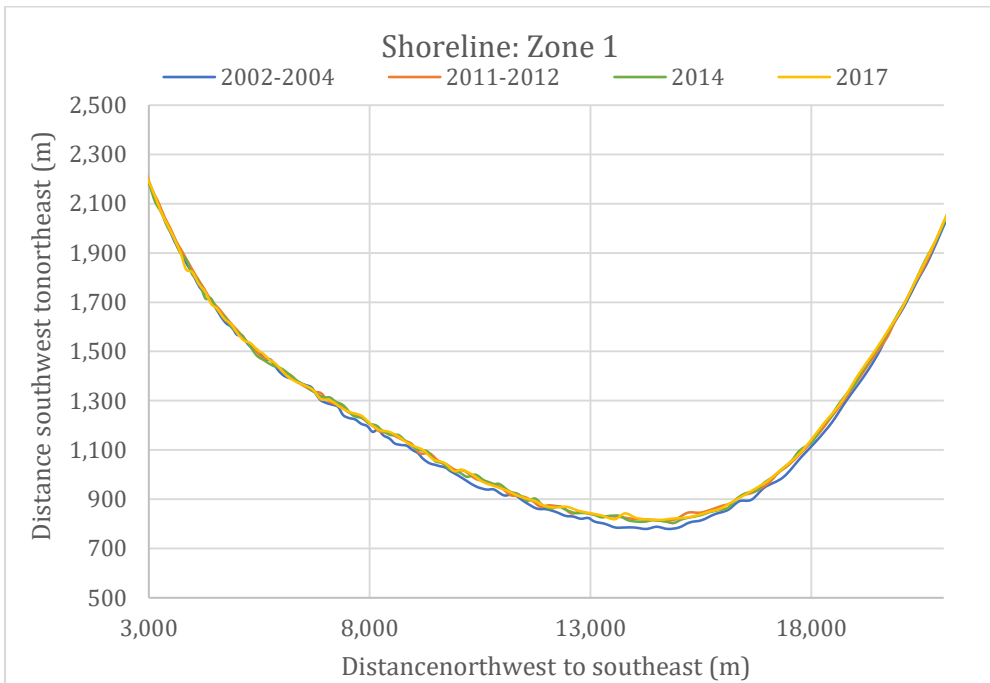


Figure A36. Shoreline position for Zone 1 in Figure 30, section 5.6, for the years “2002-2004”, “2011-2012”, “2014”, and “2017”.

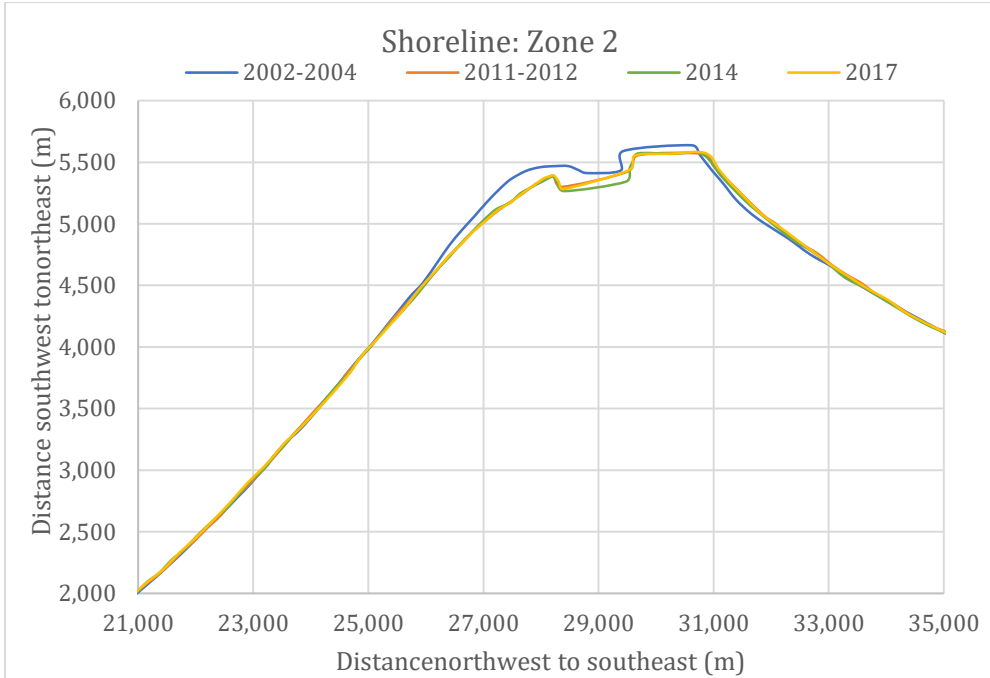


Figure A37. Shoreline position for Zone 2 in Figure 30, section 5.6, for the years “2002-2004”, “2011-2012”, “2014”, and “2017”.

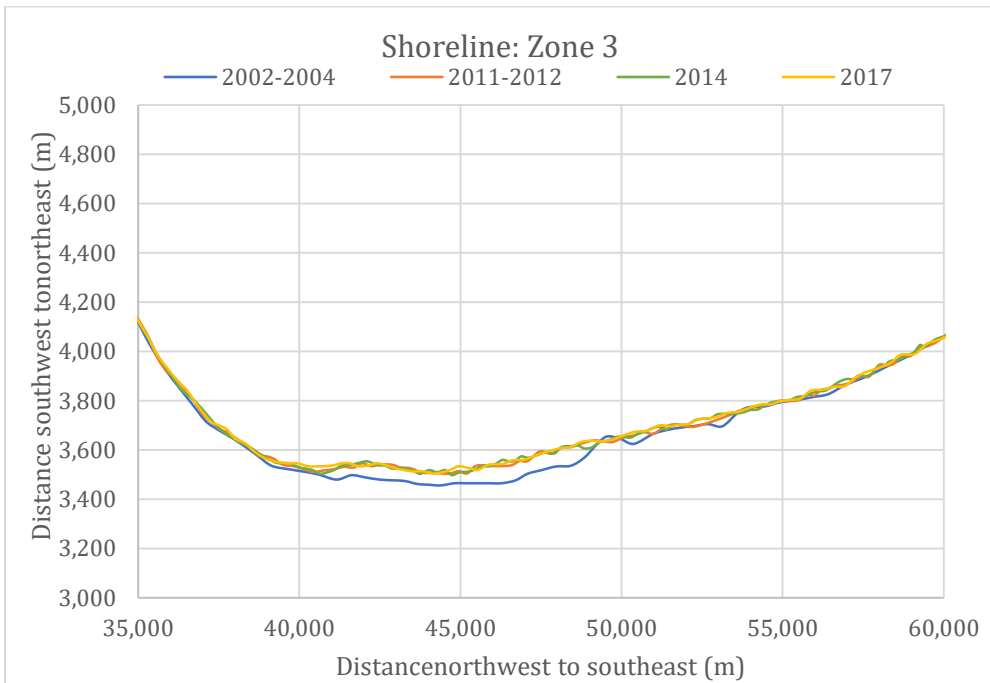


Figure A38. Shoreline position for Zone 3 in Figure 30, section 5.6, for the years “2002-2004”, “2011-2012”, “2014”, and “2017”.

Appendix B: Numerical modelling

B1. EBED

For the validation of the EBED model four different indexes were used: root-mean-square error (*rel.rmse*), scatter index (*s.i*), relative bias (*rel.bias*), and coefficient of determination (r^2). The indexes are also applied in the study by Nam et al. (2017). The *rel.rmse* is calculated as expressed in Equation B1, and takes both random and systematic errors into account. The *s.i* (Equation B2) also includes both earlier mentioned errors. *Rel. bias* (Equation B3) only considers the systematic errors. The r^2 value (Equation B4) gives an overall estimation of how well the calculated data fit the observed data. The range of the r^2 value is between 0 to 1, with a perfect fit giving the r^2 value 1.

$$rel.rmse = 100\% \times \sqrt{\frac{\sum_{i=1}^N (H_{s,calc,i} - H_{s,meas,i})^2}{\sum_{i=1}^N (H_{s,meas,i})^2}} \quad (B1)$$

$$s.i = \sqrt{\frac{1}{N} \sum_{i=1}^N (H_{s,calc,i} - H_{s,meas,i})^2 / \bar{H}_{s,meas}} \quad (B2)$$

$$rel.bias = \frac{1}{N} \sum_{i=1}^N (H_{s,calc,i} - H_{s,meas,i}) / \bar{H}_{s,meas} \quad (B3)$$

$$r^2 = \frac{COV(H_{s,calc}, H_{s,meas})^2}{Var(H_{s,calc})Var(H_{s,meas})} \quad (B4)$$

Where,
 $H_{s, calc}$ = calculated significant wave height,
 $H_{s, meas}$ = measured significant wave height,
 N = number of data points,
 COV = covariance,
 Var = variance

Table B1 show the calculated results for the average significant wave height, H_s , for each one of the input years, with the corresponding deep-water wave conditions. It also provides the average result.

Table B1. Yearly average significant wave height in each location point and initial deep-water wave.

H_s(m) Year	L1	L2	L3	L4	L5	L6	L7	L8	L9	L10	L11	Deep
1988	0.65	0.96	1.01	0.92	0.76	0.68	0.71	0.93	1.04	1.07	1.07	1.13
1989	0.62	0.89	0.93	0.83	0.67	0.61	0.67	0.86	0.95	0.98	0.98	1.04
1990	0.57	0.83	0.86	0.78	0.64	0.57	0.62	0.80	0.89	0.91	0.91	0.97
1991	0.61	0.86	0.87	0.77	0.61	0.57	0.65	0.84	0.91	0.92	0.92	0.98
1992	0.61	0.87	0.90	0.80	0.65	0.60	0.66	0.85	0.93	0.95	0.95	1.01
1993	0.63	0.91	0.94	0.84	0.68	0.62	0.68	0.88	0.97	0.99	0.99	1.04
1994	0.55	0.78	0.80	0.72	0.57	0.52	0.58	0.76	0.83	0.84	0.84	0.90
1995	0.61	0.89	0.93	0.84	0.68	0.61	0.65	0.86	0.96	0.97	0.98	1.03
1996	0.62	0.93	0.97	0.88	0.70	0.62	0.67	0.89	0.99	1.01	1.01	1.06
1997	0.51	0.72	0.74	0.66	0.54	0.50	0.55	0.70	0.77	0.79	0.79	0.84
1998	0.55	0.78	0.82	0.75	0.64	0.60	0.62	0.77	0.87	0.88	0.90	0.96
1999	0.58	0.89	0.94	0.87	0.70	0.60	0.63	0.84	0.96	0.98	0.99	1.03
2000	0.56	0.85	0.90	0.83	0.68	0.59	0.61	0.81	0.92	0.94	0.95	1.01
2001	0.54	0.81	0.85	0.77	0.62	0.54	0.58	0.77	0.87	0.88	0.89	0.94
2002	0.51	0.73	0.76	0.68	0.56	0.51	0.56	0.71	0.78	0.80	0.81	0.87
2003	0.55	0.79	0.82	0.73	0.59	0.53	0.59	0.77	0.84	0.86	0.86	0.92
2004	0.52	0.74	0.77	0.68	0.54	0.49	0.55	0.72	0.78	0.80	0.80	0.86
2005	0.57	0.81	0.84	0.75	0.61	0.56	0.61	0.79	0.87	0.89	0.89	1.19
2006	0.53	0.77	0.80	0.73	0.60	0.55	0.59	0.75	0.83	0.85	0.86	1.13
2007	0.56	0.82	0.86	0.79	0.65	0.59	0.61	0.79	0.89	0.91	0.92	1.19
2008	0.56	0.84	0.89	0.81	0.65	0.57	0.60	0.80	0.90	0.92	0.93	1.21
2009	0.53	0.79	0.83	0.75	0.61	0.54	0.57	0.75	0.84	0.86	0.87	1.11
2010	0.58	0.81	0.83	0.75	0.62	0.58	0.63	0.79	0.87	0.89	0.89	1.17
2011	0.61	0.95	1.01	0.92	0.74	0.64	0.66	0.90	1.01	1.04	1.04	1.31
2012	0.50	0.72	0.75	0.67	0.54	0.50	0.54	0.70	0.77	0.79	0.79	1.08
2013	0.59	0.87	0.90	0.82	0.67	0.60	0.64	0.84	0.93	0.95	0.95	1.21
2014	0.71	0.94	0.94	0.79	0.61	0.61	0.75	0.94	0.99	1.00	0.97	1.11
2015	0.70	0.86	0.86	0.74	0.64	0.67	0.79	0.91	0.96	0.97	0.96	1.07
2016	0.73	0.97	0.98	0.88	0.74	0.73	0.83	1.00	1.07	1.09	1.08	1.19
2017	0.75	1.00	1.01	0.90	0.75	0.73	0.83	1.01	1.09	1.11	1.10	1.21
Ave- rage	0.59	0.85	0.88	0.79	0.64	0.59	0.64	0.82	0.91	0.93	0.93	1.06

B2. LST

Figure B1 shows an illustration of how the input angle for the longshore transport calculations was estimated for location L2. Table B2 shows the used input angle for each one of the 11 studied locations.

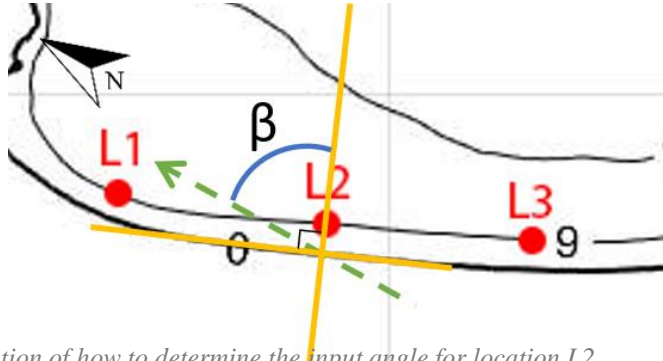


Figure B1. Illustration of how to determine the input angle for location L2.

Table B2. Input angle for each studied location.

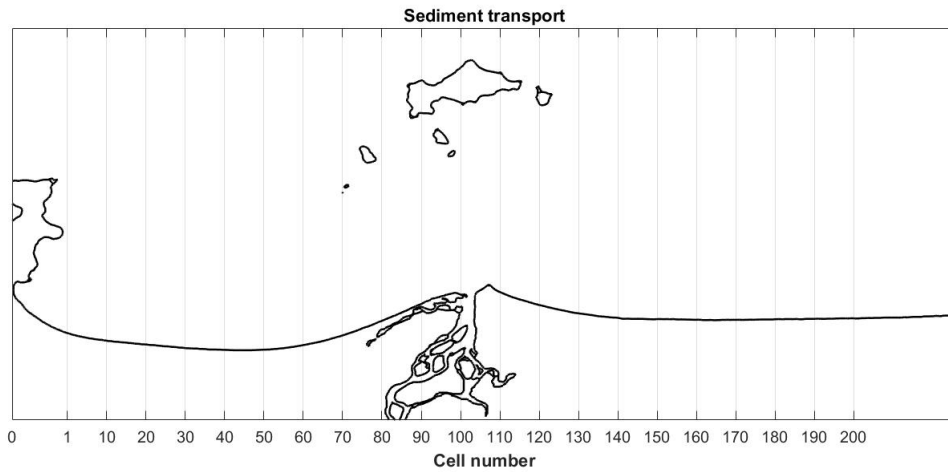
Location	L1	L2	L3	L4	L5	L6	L7	L8	L9	L10	L11
Input angle β ($^{\circ}$)	82	67	62	45	32	46	80	66	61	60	58

B3. Cascade

Figure B2 shows the grid and cell numbering used for the Cascade simulations, where each cell was 250 m and there were 200 cells in total. The amount of annual average net sediment transport over 10 cells is shown in Table B3.

Figure B2. The grid used for Cascade simulations, where the cell number is shown on

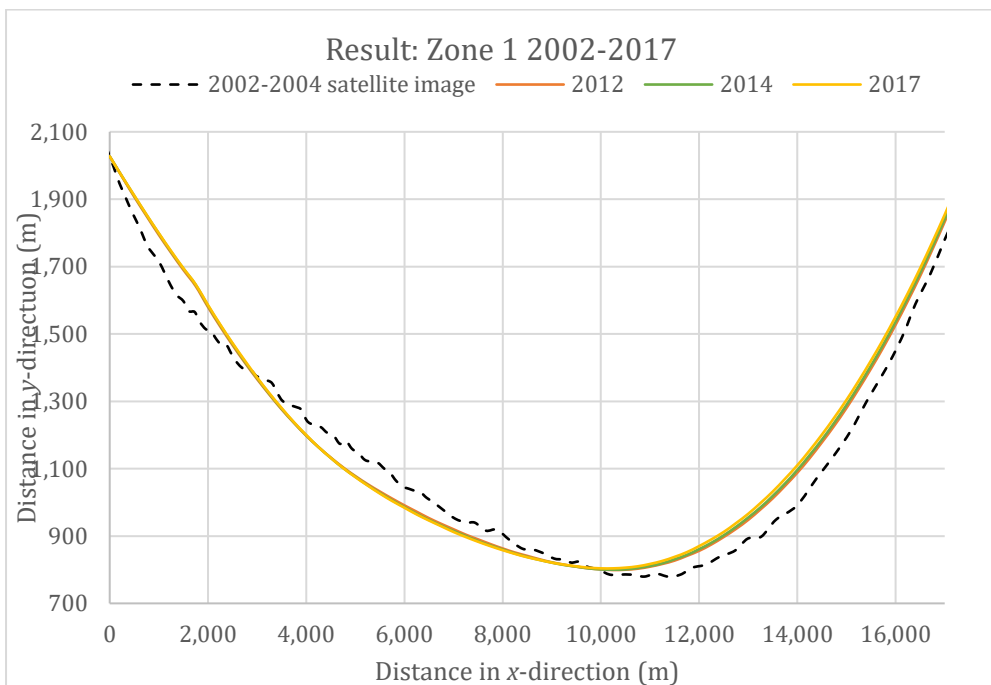
Table B3. The annual average net sediment rate per cell number, where a positive value corresponds to movement in the positive direction of the x-axis.



Cell number	Annual Average (m ³) x 10 ³
1-10	32
11-20	-33
21-30	65
31-40	145
41-50	142
51-60	33
61-70	-135
71-80	-250
81-90	-307
91-100	-237
101-110	105
111-120	280
121-130	-14
131-140	-165
141-150	-228
151-160	-207
161-170	-161
171-180	-170
181-190	-151
191-200	-67

Figures B3 to B5 show the simulated result in Cascade for the years 2012, 2014, and 2017, together with the initial shoreline at “2002-2004”. The location of each zone is illustrated in Figure 50 of section 6.3.3. Figure B3 of Zone 1 indicates accretion of the beach from 10,000 m to 17,000 m. Figure B4 shows signs of erosion around the river mouth. In Figure B5, from 33,000 to 38,000 m there is accretion.

Figure B3. Shoreline evolution 2002 to 2017 for Zone 1.



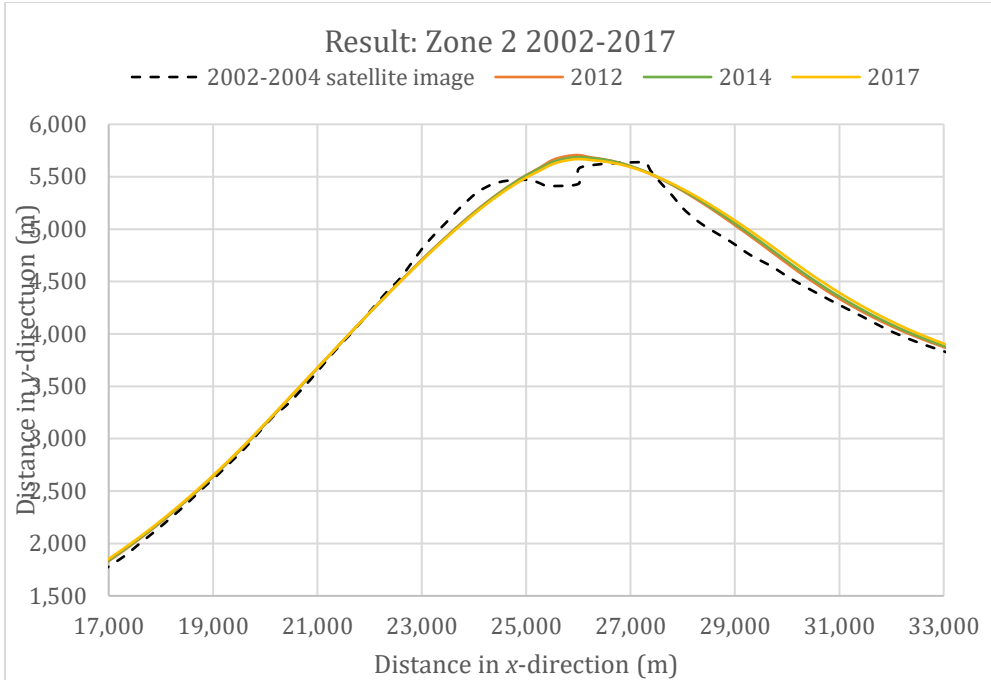


Figure B5. Shoreline evolution 2002 to 2017 for Zone 3.

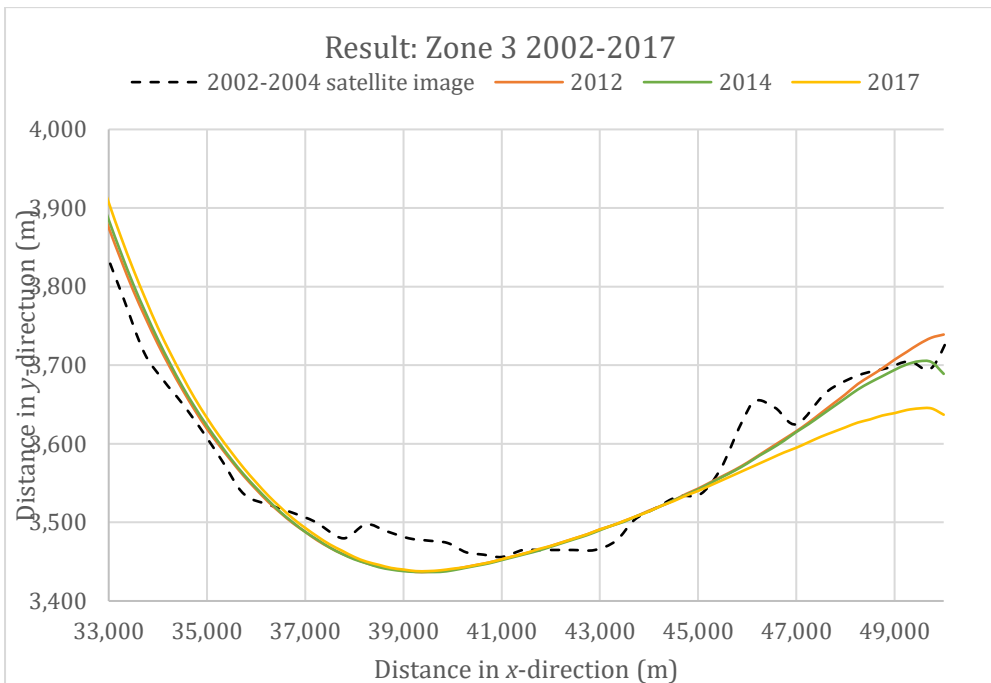


Figure B4. Shoreline evolution 2002 to 2017 for Zone 2.

Figures B6 to B8 illustrate the resulting shorelines for the future scenarios modelled with Cascade and described in more detail in section 6.3.3. Each of the figures shows a zoom for the three zones in Figure 50 (section 6.3.3).

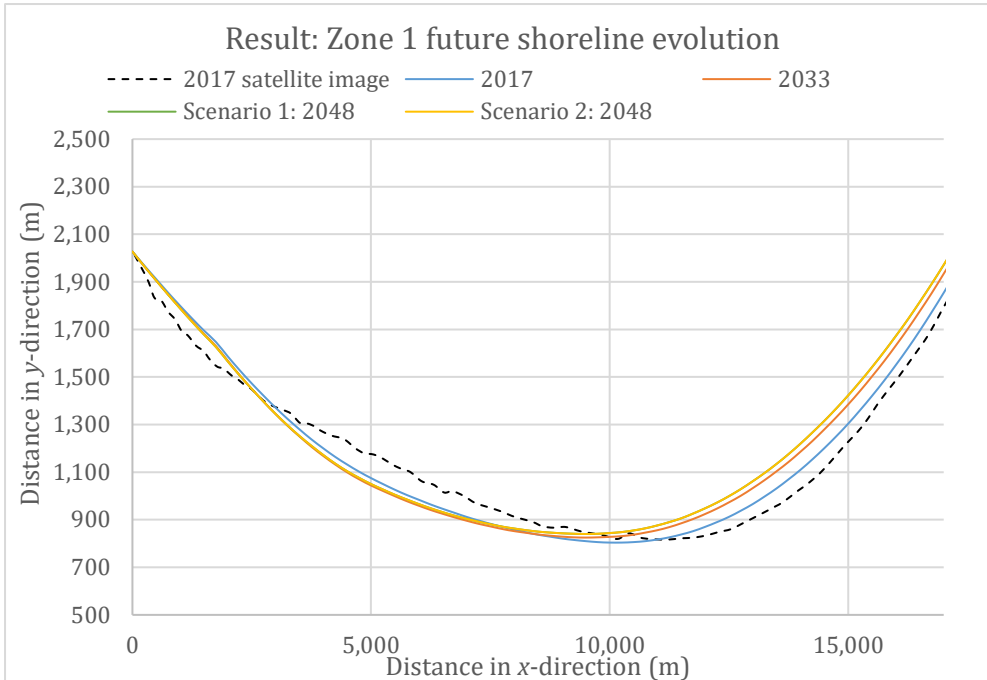


Figure B6. Cascade results for Zone 1 of future shorelines 2033, and two different scenarios 2048 together with the shoreline location 2017.

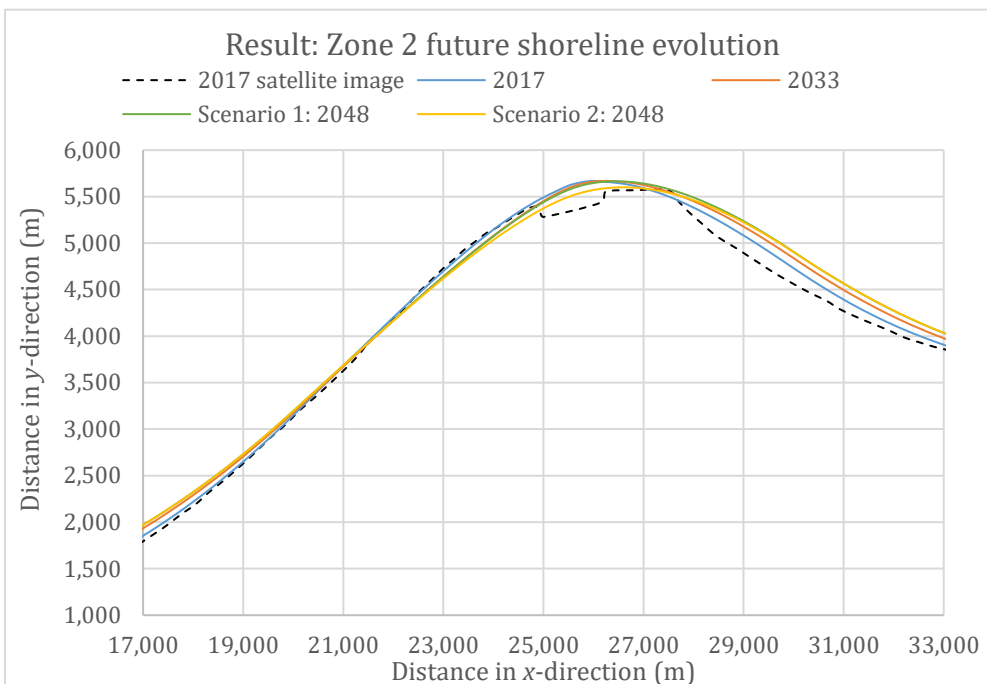


Figure B7. Cascade results for Zone 2 of future shorelines 2033, and two different scenarios 2048 together with the shoreline location 2017.

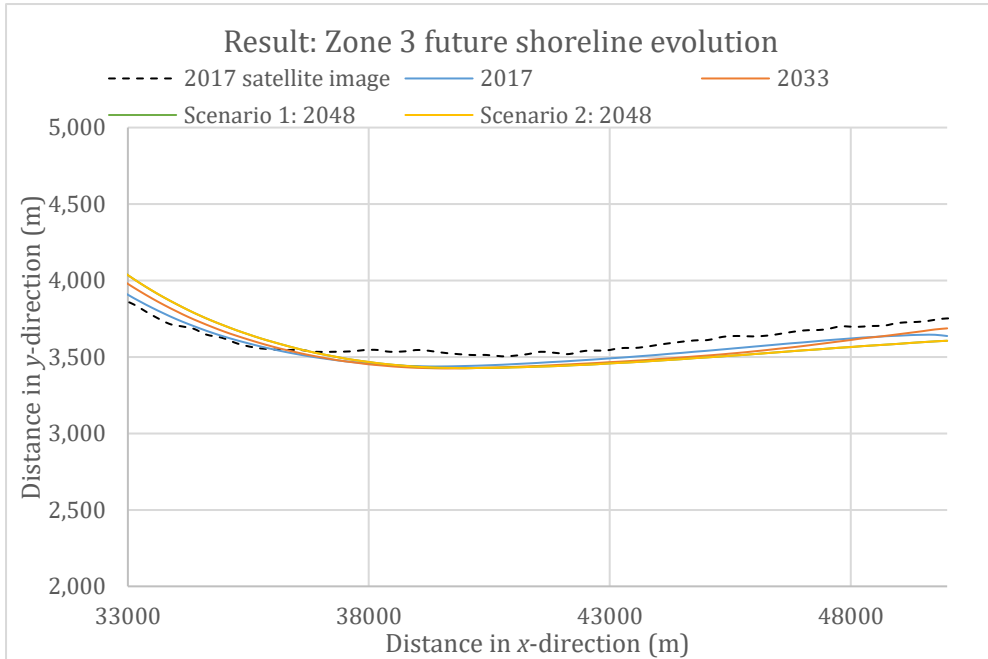


Figure B8. Cascade results for Zone 3 of future shorelines 2033, and two different scenarios 2048 together with the shoreline location 2017.

B4. Comparison between LST and Cascade

The calculated annual average net sediment transport rate in each of the 11 location points with LST and Cascade are presented in Table B4, where a positive value indicates a transport direction along the x-axis in the positive direction.

Table B4. A comparison between the calculated annual average net sediment transport rate in LST and Cascade.

Location	LST ($\text{m}^3 \times 10^3$)	Cascade ($\text{m}^3 \times 10^3$)	Difference ($\text{m}^3 \times 10^3$)
L1	21	76	55
L2	178	12	166
L3	220	162	58
L4	-210	-62	148
L5	-190	-285	95
L6	20	-124	144
L7	28	90	62
L8	31	-212	243
L9	18	-171	189
L10	43	-175	218
L11	62	-146	208